ROSAT Observations of Superflares on RS CVn Systems

Vito Giuseppe Graffagnino

Thesis submitted for the degree of Doctor of Philosophy,
in the Faculty of Science of the University of London.

Mullard Space Science Laboratory
Department of Space & Climate Physics
UNIVERSITY · COLLEGE · LONDON

2000

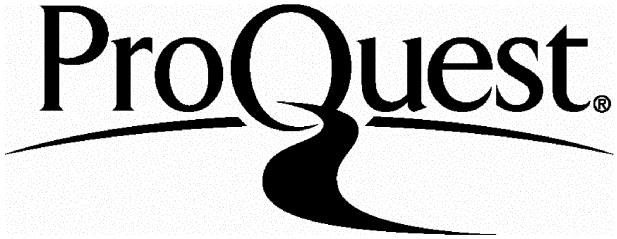

... A Mia Moglie

E

Miei Genitori

Abstract

The following thesis involves the analysis of a number of X-ray observations of two RS CVn systems, made using the ROSAT satellite. These observations have revealed a number of long-duration flares lasting several days (much longer than previously observed in the X-ray energy band) and emitting energies which total *a few percent* of the available magnetic energy of the stellar system and thus far greater than previously encountered. Calculations based on the spectrally fitted parameters show that simple flare mechanisms and standard two-ribbon flare models cannot explain the observations satisfactorily and continued heating was observed during the outbursts. This is the first time that such departures from two-ribbon flare models have been identified unambiguously for such large flares, however for some of these outbursts the situation is complicated by the fact that other flaring activity may have been superimposed on the observed lightcurves. By analysing the general decay of the flares, loop heights were derived. Although these loop heights are dependendent on the amount of heating assumed, the calculations were performed for a wide range of reasonable heating values. For these cases the flare heights obtained for these outbursts were of the order of the inter-binary separation and inter-binary flares are suggested as the cause of the outbursts.

Contents

List of Tables

List of Figures

Acknowledgements

Question the beauty of the earth,
Question the beauty of the sea,
Question the beauty of the air distending and diffusing itself,
Question the beauty of the sky ...
Question all these realities.

St. Augustine of Hippo, Sermo 241, 2: PL 38, 1134.

Okay, now for the difficult part. As anyone who has had the privilige, opportunity and insane idea of attempting a PhD would know, a thesis (although personal in nature) involves the interaction of many people, without whom the project would be doomed to failure.

So firstly I would like to thank my supervisor, Graziella Branduardi-Raymont, without whose invaluable support, this thesis would not have been possible. Grazie.

Many, many, many thanks also to Dave Wonnacott, who has been a second supervisor to me. He has guided me along, encouraged me with his infectious enthusiasm of all things astronomical and introduced me to Babylon 5 and the writings of Tom Clancy. Without him this thesis would have been a pamphlet the size of a postage stamp rather than the tome that it has become. I will be forever indebted to him.

To all the gang at MSSL, past and present including: The all singing

and dancing, John Mittaz; The walking and talking 'home entertainment' duo Chris Jomaron and Mark Garlick; PJS1 aka Phil Smith (hmmmm); Andy Phillips (Genius); Lee Sproats (for whom the words *beat* and *meat* are often in the same sentence); Gavin Ramsey (mad as a tartan fruitbat); Steve Potter (this man will beat you at any game in existence. Do not gamble with this man); and Encarne Romero Colmenero and Kerry Nicholson who have shown that having brains and being babes (in that order) are not mutually exclusive.

Many thanks also to the gang at UCL. Special thanks to Hoanh Lam whose limits on drinking coffee and letching were pushed to olympic standards. Volumes could be written about this man. A delight to behold. Bill Ball, for sharing with me the predicament of trying to complete a thesis whilst ducking and diving with the DSS. I would like to say that this experience has made us more tenacious in our outlook, stronger in will, and generally altogether better people, but I'm probably far too bitter and twisted for that now. I'm also amazed at how much alcohol this man can consume. Raman Prinja I hold in great esteem for the many useful and sometimes surreal discussions on life, Astronomy, Harrow, and anything else that came to mind as and when he would storm into the STARLINK user room. Also many thanks to John Deacon - manager extraordinaire of aforementioned user room, and all the other afflicted personalities who I have come to know and love at UCL.

Finally I would like to thank my family, for their continued support and also many thanks to Donna, who has shared much of my pain and joy in this endeavour. This thesis would never have been completed without them.

I acknowledge the support provided by PPARC in granting me a studentship.

Chapter 1

An Introduction to Stellar Extremists — RS CVns

There is nothing more difficult to take in hand,
or perilous to conduct,
or more uncertain in its success,
than to take the lead in the introduction of a new order of things.

Niccolo Machiavelli

1.1 INTRODUCTION

The RS CVn group of binary systems are the most active and X-ray bright of the normal stars, due to tidal enhancement of the dynamo effect. As such they provide an unparalleled astrophysical laboratory in which to investigate and understand the underlying physical processes of both quiescent and active stellar coronae. Coronal and flare activity in both the Sun and other stars

is generally explained in terms of plasma which has been heated to X-ray temperatures and which is confined within magnetic loops. The following thesis presents analyses of X-ray observations for two RS CVn systems which have demonstrated extremes of activity, and it is the intent of this introductory chapter to set the scene for their analysis.

1.2 THE RS CVn BINARY SYSTEMS

The class of chromospherically active binaries known as the RS CVns has it's beginnings in 1946, when Struve noticed the similarities in a group of 5 binary systems which exhibited Ca II H and K emission lines ($\lambda\lambda\, 3933, 3968\, \mathring{A}$) stronger than found in single stars of the same spectral class. The emission lines from these binaries (all with at least one component of late-G or early-K spectral type and a mass ratio near unity) were visible outside of eclipse, and their strengths were phase-dependent. Gradually the number of systems recognised as sharing these characteristics increased (Hiltner 1947; Gratton 1950; Popper 1970) and a working definition for this class of stars was finally produced by Hall (1976).

In total, Hall recognised and listed 18 general properties common to the group, but his three main defining criteria were:

1. strong Ca II H and K emission seen outside of eclipse;
2. binary systems with orbital periods of 1–14 days; and
3. a hotter component of spectral type F or G and luminosity class V or IV.

Although these defining criteria may seem somewhat arbitrary (arising as they did from a collation of similarly observed properties), a physical basis for

these characteristics can be demonstrated (e.g. Linsky 1984). For instance, one of the distinguishing features separating the active components in RS CVn systems from normal single stars of the same spectral type is their rapid rotation, which in the case of close binaries is enhanced by tidally induced synchronisation of orbital and rotation period.

Zahn (1977) has shown that for stars with convective envelopes, the synchronization time for the system can be expressed in terms of the mass ratio and orbital period. His expression for the synchronization time is given in equation 1.1.

$$t_{\rm synch} \sim 10^4 \left[\frac{1+q}{2q}\right]^2 p^4 \text{ years} \qquad (1.1)$$

Where q is the mass ratio and p the orbital period for the system in days. Most RS CVns have mass ratios $\sim$ 1, therefore using equation 1.1, synchronization timescales of $\lesssim 4 \times 10^8$ years are obtained for systems which lie within Hall's defining criterion of 1–14 days. Even shorter synchronization timescales were proposed by Tassoul (1987, 1988; see also Tassoul and Tassoul 1997 and references therein) who extended the simplified tidal-friction model of Zahn, by considering the axial non-symmetries present in a nonsynchronous binary system due to the presence of tidal bulges. As will be seen from the next section, RS CVn systems are evolved binary systems whose ages far exceed the synchronization times calculated above. Synchronization within these systems therefore results in rapid rotation of the component stars, which as a consequence of the dynamo effect, exhibit the observed enhanced chromospheric activity.

A variation of Hall's defining criteria, combining numbers 1 and 3 above with the presence of a photometric or distortion wave in the optical light-curve (see Fig. 1.4) was suggested by Fekel, Moffet and Henry (1986). This last

feature has become known as a typical characteristic of the RS CVn systems (and other chromospherically active stars), and will be dealt with more fully in section 1.3.4.

1.2.1 RS CVns and evolution

With the definition of the RS CVns as a class, their evolutionary status came into question. An early suggestion for the evolutionary nature of the prototype system, RS CVn, was that it was a T-Tauri type object (Catalano and Rodonò 1967; Hall 1972) and as such had not entered onto the main sequence. However the accepted view now is of a post-main sequence evolutionary status for RS CVns (Ulrich and Popper 1974; Popper & Ulrich, 1977). These authors found that in their sample of detached binary systems, those not showing RS CVn phenomenology (i.e. Ca II emission, light-curve modulation) occupied the main sequence, whereas the RS CVn systems occupied the Hertzsprung gap. This implies that RS CVn systems have already completed core-hydrogen burning and have developed convective envelopes (Iben 1991). One consequence of this scenario is that some mass exchange or mass-loss may occur within the system, during the crossing of the Hertzprung gap. A number of observations seem to support this hypothesis including infra-red excesses found in some RS CVns (see section 1.3.4), and observed period changes (Hall & Kreiner 1980; Thompson, Coates & Anders 1991), as well as observations indicating the possibility of matter streams (Huenemoerder 1985). Such a central position within the HR diagram also lends itself to speculation as to whether RS CVns systems may be Algol-precursors (Iben 1989) or forerunners to cataclysmic variables (Tout & Eggleton 1989).

1.3 X-RAY OBSERVATIONS OF RS CVn SYSTEMS

As this thesis is primarily concerned with observations made in the X-ray regime, this section provides a historical background to the observations described herein.

1.3.1 A Brief Historical Introduction

The Earth's atmosphere is (fortunately) opaque to X-rays ($3 \times 10^{16} \lesssim \nu \lesssim 3 \times 10^{19}$ Hz). Thus the study of extra-terrestrial X-ray emissions was impractical until the arrival of the space-age, when post-World War II rocket technology allowed instruments to be carried sufficiently far (> 80km) above the Earth to allow cosmic X-ray detections. By the late 1940's, the Sun was revealed to be a source of X-rays (Burnight 1949) and the rocket missions of the early sixties discovered a sky containing many non-Solar X-ray sources (e.g. Giacconi et al. 1962; Gursky, Giacconi, & Paolini 1963).

It was not until 1974 however, that the first detection of X-rays from a 'normal' star (Capella) was made whilst calibrating instruments aboard a rocket launched by the Lockheed Palo Alto Research Laboratory (Catura, Acton, & Johnson, 1975). Several months later these X-ray emissions were confirmed by the soft X-ray detector aboard the Astronomical Netherlands Satellite, *ANS* (Mewe et al. 1975).

Quiescent X-ray emission from an RS CVn system (HR 1099) was not discovered until observation by the *HEAO-1* satellite (White, Sanford & Weiler 1978). Further observations of nine RS CVn systems by the *HEAO-1* satellite led to suggestions that RS CVns were a new class of X-ray source and that the X-ray emissions may be coronal in nature (Walter, Charles and Bowyer

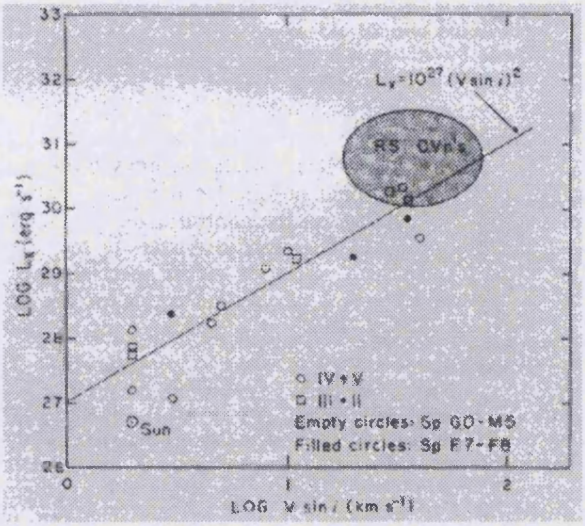

Figure 1.1: *Pallavicini's x-ray luminosity vs v sini relationship for late-type stars (From Ap.J.* **248**, *p.286.)*

1978; Walter et al. 1980). In this scenario the coronae of RS CVn systems consist of magnetically confined loops of plasma (as is the case for the Sun) which obey the scaling laws derived by Rosner, Tucker and Vaiana for the Solar case (1978) relating the coronal loop length, temperature and pressure. Their results show that coronal magnetic loop models are capable of producing the observed X-ray luminosities, unlike the previously hypothesised acoustic models (e.g. Landini and Fossi 1973; Hearn 1975).

1.3.2 Stellar X-ray Luminosity Relationships

The *Einstein* (*HEAO-2*) satellite survey results (Vaiana et al. 1981) demonstrated the ubiquity of stellar X-ray emission across almost the whole range of spectral types (excluding A-type stars). Among the main results from this survey was the lack of any clear correlation of X-ray luminosity with luminosity class for either early or late-type stars (Pallavicini et al. 1981). Early-type

stars demonstrated a definite correlation between X-ray and bolometric luminosities. Late-type stars however displayed a good correlation with equatorial rotational velocities [of the form $L_x \simeq (v \sin i)^2$] as displayed in Fig. 1.1. This latter is interpreted as evidence for stellar dynamo-induced activity and has served to demonstrate the important rôle played by the star's own magnetic field in coronal heating of late-type stars (Vaiana et al. 1981; Pallavicini et al. 1981).

Fig. 1.1 shows that RS CVns Obey an X-ray luminosity/rotation rate dependence for all late-type stars, of the form $L_x = 10^{27}(v \sin i)^2$ (e.g. Pallavicini et al. 1981; Dempsey et al. 1993a). However, when the sample consists solely of RS CVns, this rotational dependence becomes almost non-existent. This can clearly be seen from Fig. 1.2 which shows the wide spread in X-ray luminosity for a particular value of $v \sin i$ exhibited by the RS CVn systems catalogued by Strassmeier et al. (1993). The solid line in this figure denotes Pallavicini's luminosity-rotation relation found for his sample of active stars. The dashed line indicates the line of best fit found by a least squares method (I used the IDL procedure LINFIT to calculate this). As judged by the χ^2_ν value of 22.8, this is statistically a poor fit. The IDL procedure CORRELATE derived a value for the linear Pearson correlation coefficient, ρ, of 0.122, a further indication of a poor correlation between the luminosity and the $v \sin i$ values.

Although the Dempsey et al. sample of RS CVns (1993a) — from the ROSAT all-sky survey (the largest X-ray sample of RS CVns to date) — did find an inverse proportionality between X-ray flux, F_X, and rotation period, this can be attributed solely to systems containing sub-giant and giant active stars, because in RS CVns systems, in which the active component is a dwarf star, this inverse proportionality disappears. This proportionality can therefore be shown to be principally due to the bolometric luminosity dependence

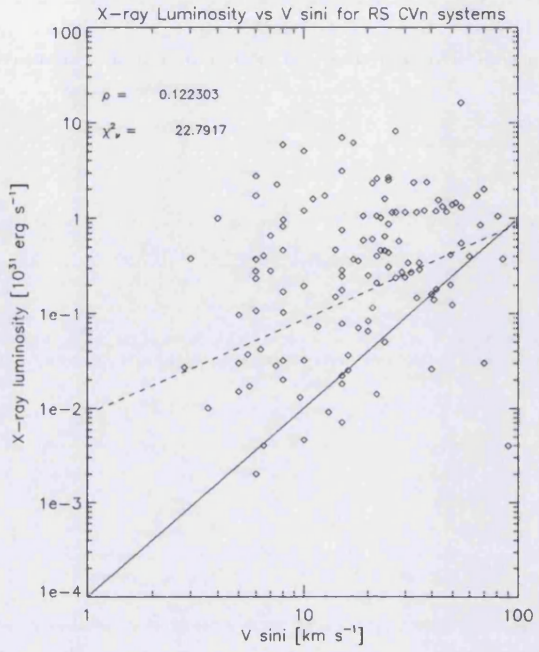

Figure 1.2: *X-ray luminosity vs v sini relationship for RS CVn systems. The data were extracted from the Strassmeier et al. Catalogue of Chromospherically Active Binaries (1993). The solid line denotes the luminosity/rotation relationship for all active stars found by Pallavicini et al. (1981). The dashed line denotes the best fitting line found by a least-squares method. (See text for details.)*

(e.g. Rengarajan & Verma 1983) and thus is a simple consequence of Kepler's third law. Similar arguments have been used by Majer et al. (1986) to explain earlier studies (e.g. Walter & Bowyer 1981) where some form of X-ray luminosity/Period relationship is suggested.

The cause of this large spread in X-ray luminosities begs further investigation, but as yet there is no clear understanding of which other factors are

involved. It is clear that any rotation-activity relationship for binary systems may not be a simple one. In the case of close-binary systems such as RS CVns tidally induced forces may also need to be taken into account. Although it has been demonstrated that the presence of a companion star does not directly affect the activity level within a binary system, it will serve to produce the rapid rotation required (Dempsey et al. 1993b). The presence of a companion star may also affect the internal dynamo structure of the system by repositioning the axis of rotation in such a way that magnetic activity is enhanced (e.g. Schrijver & Zwaan 1991). Although not complete, current stellar dynamo theory (for reviews see Moss, 1986; Weiss, 1993 and references therein) requires a combination of both rotation and convection to explain magnetic activity phenomena such as X-ray emission. Thus one would expect a more reasonable (and complex) relation for a star's X-ray emission to involve both rotation and convection. An empirical measure of rotation and convection with regard to the star's dynamo is the Rossby number, R_0, defined as,

$$R_0 = P/\tau_c$$

where P is the rotational period, and τ_c is the convective turnover time (i.e. a theoretical value related to the rate of energy transport and homogenization within a star's convective zone). Note however, that one must recognise a level of uncertainty in the determination of the convective turnover times and consequently of the Rossby numbers. Current research aims to improve understanding of the convection processes within stellar interiors, extending, and in some cases trying to replace, the standard mixing-length-theory of convection (e.g. Canuto et al. 1996; Abbett et al. 1997). This uncertainty in the calculation of the convective turnover times is further increased in application to binary systems, because at present calculations use theoretical models based on single stars, and binarity effects (noted above) are ignored. With

these caveats in mind, however, strong correlations between Rossby number and chromospheric activity indicators such as Ca II H & K emission have been found for late-type stars (Noyes et al. 1984). Similar results between X-ray luminosity and Rossby number have also been found to exist (Schmitt et al. 1985; Maggio et al. 1987). Finally, an empirical relation between the volume of the convection zone and flare luminosity has been presented by Pettersen (1989) further demonstrating that the stellar dynamo-driven/magnetic nature of the X-ray emission is not restricted to the quiescent state of the star.

1.3.3 Development of Spectral Models to Fit Stellar Coronae

As will be seen below, the complexity of X-ray spectral models used to describe stellar coronal emission has been largely restricted by the signal-to-noise ratio of the data. For the earliest observations, only the brightest objects had high enough signal-to-noise for credible spectra to be extracted and fitted. Among these systems were Capella and UX Ari, observed by *HEAO-1* (Cash et al. 1978; Walter, Charles and Bowyer 1978). These early results were later used to constrain the temperatures (derived using hardness ratios and an assumed bremsstrahlung shape for the spectra) of 59 RS CVns surveyed by *HEAO-1* (Walter et al. 1980). Most of the systems in this sample could be described by a *single* coronal temperature consistent with T $\sim$ 10^7 K. (By comparison the quiet Solar corona only reaches temperatures of the order $\sim$ 10^6 K.)

Improved energy resolution of instruments aboard the *Einstein* observatory (0.15 – 4.5 keV) soon revealed that stellar coronae are not in fact isothermal in nature. For instance, the observation of Capella using the Solid State Spectrometer (SSS)[1] showed that the emission could be modelled by two op-

[1]Energy range 0.5 – 4.5 keV; Energy resolution 160 eV FWHM (White & Peacock

tically thin thermal plasma models at temperatures of $T_1 \sim 5 \times 10^6$ K and $T_2 \sim 5 \times 10^7$ K. (Holt et al. 1979). Comparable results for σ^2 CrB (Agrawal, Riegler and White 1981) and six other RS CVns (Swank et al. 1981) confirmed that an isothermal coronal model is insufficient to describe higher resolution data. Analysis of spectra obtained with the SSS however, was confined to the brightest (and nearest) of the RS CVn systems. A much larger dataset was provided by the Imaging Proportional Camera (IPC, 0.4 – 4.0 keV) onboard *Einstein*. A homogeneous analysis of all the available IPC spectra obtained for RS CVn systems again confirmed the need for two temperature components (Majer et al. 1986).

The establishment of this canonical two temperature thermal plasma model has continued through successive missions (e.g. EXOSAT — Mewe, Schrijver, 1986; White et al. 1986; ROSAT — Dempsey et al. 1993) and has even proved successful when fitting high spectral resolution data from EXOSAT TGS[2] e.g. Schrijver et al. (1989). However, the exact nature of this canonical two-temperature coronal emission is not universally agreed upon.

Independent variability of both temperature components in the sample of Swank et al. (1981) prompted the hypothesis that the components originated in two *physically distinct* emitting regions. Such features may be resolved through X-ray modulation/eclipses. Although analysis of *Einstein* data of the eclipsing RS CVn system AR Lac failed to show any such modulation (Swank & White 1980), later observations from EXOSAT did reveal the presence of an eclipse in the LE energy band (0.05 – 2.0 keV), but none in the harder energy band (1 – 50 keV) covered by the ME detector (White et al. 1986). The

---

1988).

[2]The Transmission Grating Spectrometer covered an energy range of 0.05 – 2 keV with a resolution 81 eV for energies > 0.25 keV (White & Peacock 1988; Heise 1988)

interpretation of this and later observations combined with eclipse modelling (Schrijver, 1985; White et al. 1987, 1988) led to the suggestion that the two-temperature models described the co-existence of a number of coronal structures within RS CVns. These comprised compact, high density and low-temperature loops as well as loops of high temperature, low density and of greater extension (with sizes comparable to the stellar radii, in contrast to the Solar case). Evidence from radio observations showing magnetospheres with sizes of the order of the binary system (e.g. Mutel et al. 1985; Massi et al. 1987 — see Section 1.3.4) and theoretical models (Uchida and Sakurai 1983, 1985) have provided corroborative evidence for such structures. However, interpretation of two-temperature models in terms solely of differing coronal structures is likely to be an oversimplification.

A comparison of the two-temperature fits from the ROSAT data for σ^2 CrB with spectral fits for data obtained by previous missions is shown in Figure 1.3. This example demonstrates that systematic temperature differences found for the same sources using different instruments may imply a dependence on the detector's effective energy. It has been suggested that in fact these sources actually possess a continuous emission-measure distribution (e.g. Majer et al. 1986; Schmitt 1987), a physically more realistic and plausible model for the coronal environment. The two-temperature model would therefore simply be a consequence of the relatively poor spectral resolution of the detectors. Monte Carlo simulations by Schmitt et al. (1987) and Pasquini et al. (1989) showed that two-temperature fits can be obtained from a continuous emission measure distribution, for data from both *Einstein* and EXOSAT LE and ME instruments. However, continuous emission measure distribution (CEM) models, with a power-law dependence of emission measure with temperature(suggested by Solar models, e.g. Antiochos & Noci 1986) only provided acceptable fits to

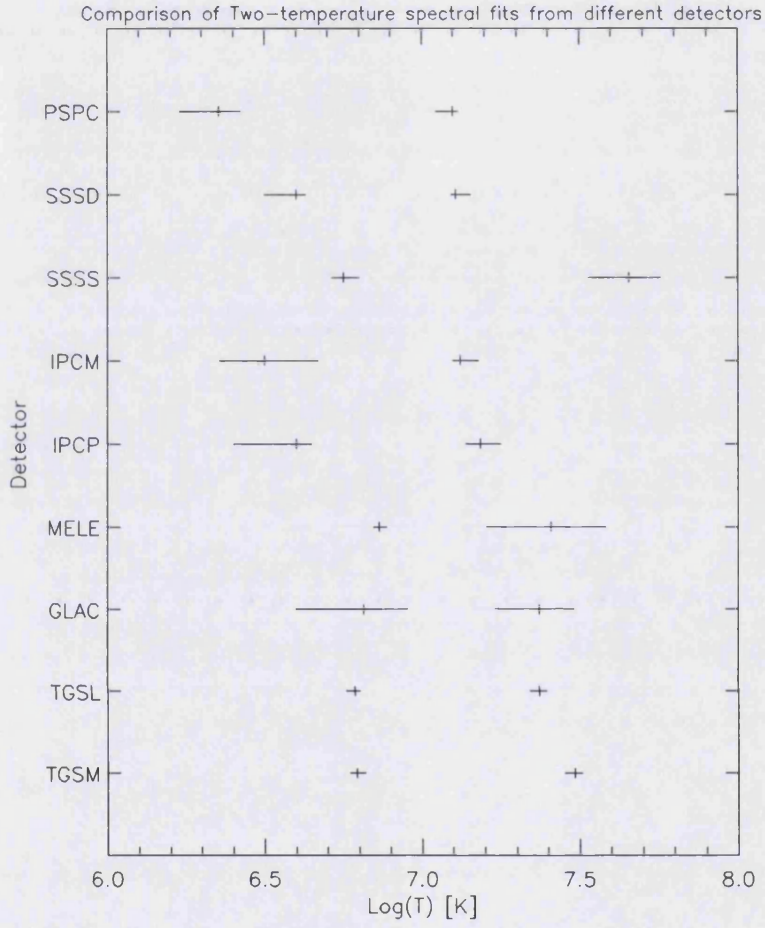

Figure 1.3: *A comparison of the two-temperature fit results for the RS CVn system σ^2 CrB. PSPC refers to the RASS spectra taken by Dempsey et al. 1993b; SSSS data are from Swank et al. (1981); SSSD refer to a reanalysis of the Swank et al. 1981 data using updated plasma codes; IPCM and IPCP refer to analysis of IPC data by Majer et al. (1986) and Pasquini et al. (1989) respectively; MELE refers to the Pasquini et al. (1989) analysis of EXOSAT ME and LE data; GLAC refers to Ginga LAC results (Stern 1992); TGSL and TGSM refer to the analysis of Transmission Grating Spectrograph data by Lemen et al. (1989), and Mewe et al. (1986), respectively. [Extracted from Dempsey et al. (1993b)].*

half of the spectra in the Pasquini et al. (1989) sample, and of these fits the results suggested an emission measure distribution for RS CVns differing from that of the Sun.

Higher quality spectra for some RS CVns (obtained through longer exposures during the pointed phase of the ROSAT mission) could also be fitted by two-temperature thermal plasma models (e.g. Ottmann, Schmitt & Kürster 1993; Ottmann 1994). Ottmann et al. noted, though, that in order to unify their ROSAT two-component temperatures for AR Lac with those obtained by *Einstein* and EXOSAT, an underlying continuous emission measure distribution should be assumed. Other ROSAT spectra of RS CVn systems, could not be satisfactorily fitted by simple two-temperature thermal plasma models, and required more complex multi-temperature or differential emission measure models (e.g. Jeffries 1992; Drake et al. 1994; Singh, Drake & White 1995). The requirement of a more complex (multi-temperature) model seems to be dependent not only on the resolution of the instrument but also on the signal-to-noise of the spectrum. Jeffries mentions that in his ROSAT observation of λ And, two-temperature models did fit some of his spectra. However, this was not the case for those spectra with higher counts. Thus, for observations made with broad-band instruments, multi-temperature models can be used as approximations to differential emission measure distributions models. Naturally one must not neglect the restrictions imposed by the spectral resolution of the detector in determining the number of temperatures used in the analysis, and this is explored more fully in Appendix A. However, although it is assumed that a continuous distribution of emitting material is present, the use of multi-temperature models may be preferable to CEM models, as no initial assumption about the form of the distribution is made. With higher resolution instruments, obviously a more accurate determination of the differential emis-

sion measure may be obtained. Recent results from EUVE demonstrate that the assumption of a continuous distribution is often a valid one for RS CVns (Walter 1996; Drake et al. 1996).

1.3.4 A Brief Review Of Characteristics At Other Wavelengths

The spectral characteristics of RS CVn systems at other wavelengths provide further demonstrations of magnetic activity and structures. Many of these characteristics are shared with the other types of chromospherically active stars (e.g. Algols, BY Draconis systems, and rapidly rotating single stars). However by virtue of their high-activity levels, RS CVns provide a more stringent test of our understanding of Solar-like phenomena when extrapolated to extremes of physical conditions.

RS CVn Characteristics Derived From Radio Observations

The earliest radio observations of RS CVn systems include those of Owen, Jones and Gibson (1976), Owen and Gibson (1978) and Feldman et al. (1978). These and later observations have shown RS CVn systems to be highly variable radio sources, with flux densities ranging from a few mJy during quiescent periods up to ~ 1 Jy in strong flares (e.g. see Table 2 from Mutel and Lestrade 1985). Observations utilising the high-resolution capabilities of the VLBI have demonstrated the existence of both a core and a halo magnetospheric structure for RS CVns, with the extended halo structure being comparable to the size of the binary system (Mutel et al. 1985; Lestrade et al. 1988). The quiescent emission mechanisms are thought to involve gyrosynchrotron radiation from a nonthermal electron population, which in some models is trapped in a toroidal "dead-zone" (e.g. Morris, Mutel & Su 1990). High brightness temperatures

measured in some of these systems ($T_b \gtrsim 10^8$ K) seem consistent with this model (Hjellming and Gibson 1980; Kuijpers and van der Hulst 1985). Some circular polarization is often exhibited, with the quiescent emission being much more strongly polarised than during flare events. A reversal of the direction of circular polarization is also seen to occur between high and low frequencies. Initially it was believed that this was a property of the underlying quiescent emission (Owen et al. 1976; Borghi and Chiuderi Drago 1985). However the gyrosynchrotron model used to explain the quiescent emission does not effectively predict the sense of reversal in polarisation, and as yet no complete explanation is available [see White and Franciosini (1995) for a brief review of these processes].

Infra-Red Emission From RS CVns

A large proportion of the photospheric emission from G and K stars (found in RS CVn systems) lies in the infra-red region of the electromagnetic spectrum. A number of IR studies have been carried out and include both ground-based and space-based infra-red photometry (Busso et al. 1987). These have been used to construct the energy distribution of a number of these systems over a wide wavelength interval (Scaltriti et al. 1993a and references therein). Although some early studies found no evidence for an infra-red excess (e.g. Berriman et al. 1983) it has since been shown that several RS CVn systems do show infra-red excesses, generally starting in the I band and going to longer wavelengths (Busso et al. 1987; Scaltriti et al. 1988). Results from IRAS however have been shown not to be conclusive, and clarification await results from higher resolution instruments such as those aboard ISO (Mitrou et al. 1996). If the infra-red excess is real then one explanation is through the presence of circumstellar material (Scaltriti et al 1987; Busso et al. 1988). An

observed increase in polarization with increasing wavelength (Scaltriti et al. 1993b) gives extra credence to this hypothesis, as this would suggest scattering of the infra-red emission by relatively large dust particles from circumstellar material. Such material may be indicative of episodic mass loss – a scenario consistent with the accepted evolutionary status of RS CVn systems.

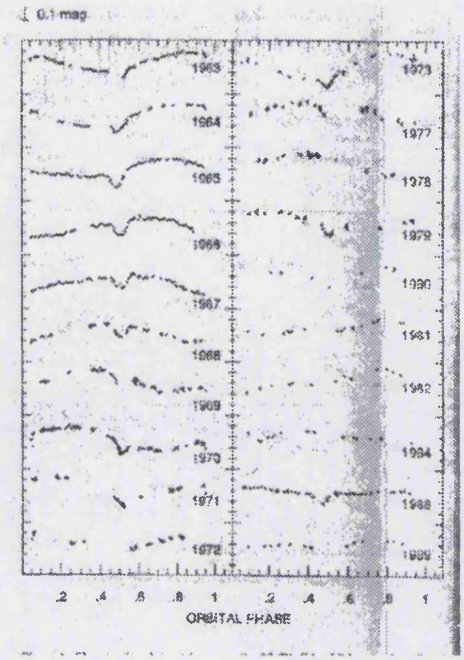

Figure 1.4: *V-band photometric measurements are plotted against the orbital phase at which they occur for the system RS CVn (sample observations shown have been taken over a 26 year period at Catania observatory). For each lightcurve note the definite presence of a secondary eclipse near phase 0.5, and indications of a primary eclipse at phase 0.0. Note also the dip which covers the whole orbital period: this is the photometric wave. The migration of this photometric wave is clearly visible over a period of years. Taken from Rodonó 1992.*

RS CVn Phenomenology At Optical Wavelengths

Much phenomenology exhibited at optical wavelengths provides important evidence for magnetic features on RS CVns located in the region of the lower stellar atmosphere and photosphere. One such phenomenon is the presence of an outside-of-eclipse photometric or distortion wave seen in the optical lightcurve. This phenomenon has been included as a defining characteristic

of RS CVns, both in a major and minor capacity (e.g. Hall 1976; Fekel et al. 1986 respectively). One of the earliest indications of this phenomenon was the reported variations in the lightcurve of the RS CVn system AR Lac (Himpel 1936). An example of typical V-band lightcurves, plotted against orbital phase, is given in Fig. 1.4. This figure shows results from detailed photometric studies of the system RS CVn by workers at Catania Observatory (Chisari & Lacona 1965; Catalano & Rodonó 1967) and clearly highlights this phenomenon. For each lightcurve, the secondary eclipse is clearly visible as a pronounced dip near phase $\sim$ 0.5. (Primary eclipse at phase 0.0 is present but not as clear). However, note that each lightcurve demonstrates a low-amplitude wave covering the whole orbit. This is the photometric wave, whose peak is observed to migrate towards decreasing orbital phases over a period of several years.

Although a number of competing hypotheses had been proposed to explain this phenomenon — e.g. circumstellar material (Catalano & Rodonó 1967, 1969, 1974; Batten 1973), nonradial pulsations (Popper 1977) — the accepted view now is that these variations are due to the presence of cool starspots (Kron 1947; Hall 1972). Starspot models have successfully been used to describe these photometric observations (Eaton & Hall 1979; Poe & Eaton 1985; Henry et al. 1995), although the presence of starspots is not restricted to inferences and modelling of photometric data; more direct evidence has been provided by spectroscopic observations of some of these systems. They include spectrophotometry of a number of RS CVn systems in which chromospheric activity indicators (such as Hα emission) have shown maximum intensity occuring at the photometric minimum (Weiler 1978). Another common feature is that of excess molecular band absorption (such as TiO and VO) indicating the presence of a cooler-than-photospheric region (e.g. Vogt 1979, 1981a; Ramsey & Nations 1980).

However, the most convincing evidence is provided by Doppler imaging. This technique was developed and first used on an RS CVn system by Vogt and Penrod (1983) who looked at HR 1099. This technique has since been employed on a variety of active systems and has provided confirmation of spot results obtained via photometric means (e.g. Rodonò et al. 1986). The picture that has emerged is one quite different from that of the Solar case. The magnitude of the variations in the photometric wave is suggestive of spots (or spot complexes) with covering areas much larger than those found in the Sun (e.g. $\sim$ 20% of the stellar surface covered as opposed to $\sim$ 5% coverage on the Sun — Vogt 1983). Another difference is the existence of high-latitude and polar spots. Although first indicated from photometric evidence (Vogt 1981b) Doppler imaging of a number of systems seem to confirm the existence of these features. Vogt and Penrod (1983) have suggested that these large polar features are actually the remnants of scaled-up active regions which have formed at low latitudes but which drift pole-ward to form the stellar analogues of Solar coronal holes. In contrast, Shüssler and Solanki (1992) have suggested that such polar migration of active regions is unnecessary. Instead they show that magnetically buoyant flux tubes, originating at the base of the convective zone of rapidly rotating stars, surface preferentially at higher latitudes, courtesy of the Coriolis force. Thus in their scenario the occurrence of polar spots would be a direct consequence of the rapid rotation. Their hypothesis, however, does not explain polar spots, only high-latitude spots, and has difficulty in explaining why lower-latitude (e.g. equatorial) spots are also observed.

Doubts over whether or not polar-spots are artifacts of the analytical process have surfaced (Byrne 1996), the main criticism being that reference line-profiles (from slowly rotating unspotted stars) used in the Doppler imaging analysis carry inherent assumptions which may not prove valid in the case of

rapidly rotating active stars. This is a valid point and other researchers have also tried briefly to address this problem (Strassmeier et al. 1991; Unruh and Cameron 1995). The question of whether such polar features do exist is still to be resolved and awaits further work.

Optical observations have also led to indications that extended material, such as prominences, may exist in RS CVn systems. By analogy to the Sun, the presence of such features should not be surprising. The difference for active systems, however, is in the substantial spatial extent of such features. Cool material trapped in magnetic loops of active systems such as the rapidly rotating single K-type star AB Dor (Collier Cameron & Robinson 1989) and in G-type dwarfs (Collier Cameron & Woods 1992), have been inferred from Hα observations, suggesting loops of several stellar radii in height. Similar results have been found for eclipsing RS CVn systems (Hall & Ramsey 1992,1994), in which excess absorption at various orbital phases has been observed in a number of chromospheric lines, and have been modelled as prominence-like features.

Ultra violet

Observations at ultra violet wavelengths provide further spectroscopic evidence of enhanced non-radiative heating (see Linsky 1985 for review) as well as of magnetic structures within the chromosphere (Walter, Gibson and Basri 1983) and the transition region (Rodonó et al. 1987). Investigation of coronal structures observed on the Sun at X-ray wavelengths culminated in a number of analytical models and scaling laws being developed. These early models used the simplifying assumption that the quiescent loop structures forming the corona, are essentially in hydrostatic equilibrium. The seminal work in this area is that of Rosner, Tucker and Vaiana (1978)— hereafter refered to as the RTV

model. (See Appendix A.1.4).

When used in combination with X-ray observations, UV data have allowed constraints to be placed on the base pressures of fitted RTV quasi-static loop models, thus limiting the range of possible loop model parameters (Giampapa et al. 1985). In the past, multiwavelength observations such as these have been hampered by the non-simultaneity of the observations, which suggest some uncertainty in the results due to possible independent variability at the chromospheric and coronal level. However, more recently a number of simultaneous multiwavelength observing campaigns (e.g. et al. 1994; Neff et al. 1996) have demonstrated consistency with previous non-simultaneous results.

Combined IUE and optical observing campaigns on a number of RS CVn systems by Rodonò et al. (1987) have shown chromospheric and transition-region line surface fluxes (of several orders of magnitude greater than Solar values) to vary in anti-phase with their optical photometric measurements. This has been interpreted as evidence for the co-spatial location of magnetic loops (which form UV-bright chromospheric plages) overlying optically dark photospheric spots — as in the case of the Sun. However, follow-up observations have revealed rotational modulation of chromospheric lines which suggest that some plages are located on the opposite hemisphere to starspots detected by optical photometric means (Doyle et al. 1989). This suggests a phenomenology different from that found on the Sun, a view further supported by Huenemoerder et al. (1990).

1.4 STELLAR FLARES

Although the first white light Solar flare was reported by Carrington in 1859, the first stellar flare was not observed until the late 1940s (Joy and Humason, 1949). It was not until the advent of spaceborne instruments that the first

X-ray stellar flare was observed on the classical flare star, YZ Canis Minoris (Heise, 1975). The first X-ray flare observed on an RS CVn system (HR 1099) was detected by instruments on the *Copernicus* satellite, using an X-ray detector built at MSSL (White, Sanford & Weiler, 1978). Since then a variety of satellite X-ray missions have detected flares on RS CVn and Algol systems (see section 1.4.3) increasing current stellar flare knowledge.

General reviews of stellar flares include those of Haisch (1989), Byrne (1989), Haisch, Strong and Rodonò (1991), and Bastian (1994). Pettersen's review (1989) showed that flares occurs on most stars across the HR diagram, and emit radiation covering the whole electromagnetic spectrum. More specific to this thesis are the review of flares on RS CVn systems by Catalano (1990) and X-ray observations of flares on late-type stars by Haisch (1983) and Pallavicini (1995).

Flares can be described as localised catastrophic releases of electromagnetic energy which lead to particle acceleration within the corona. The generally accepted source of this energy is magnetic in origin, and the canonical flare model now envisaged (e.g. Sturrock 1968; Kopp & Pneumann 1976) involves reconnection of magnetic field lines which make up the coronal loops. This arises as a consequence of a number of physical processes which are implicitly invoked in current flare models, and which are now briefy described.

Owing to the high electrical conductivity of the plasma within stellar coronae, magnetic flux freezing takes place, that is, both field lines and plasma move as a single unit. The validity of this statement (for the Solar corona) can be demonstrated by calculating the magnetic Reynolds number, $R_{\rm m}$, which gives a measure of the importance of this phenomenon for a given length scale: $R_{\rm m} \sim \frac{4\pi v l}{\eta c^2}$ (where v is the plasma flow velocity, c is the speed of light, l is the length scale and η is the resistivity of the plasma). For length scales char-

acteristic of magnetic structures on the Sun, a high value of R_m is obtained, indicating that the assumption of magnetic flux freezing occuring is a good one (e.g. Tandberg-Hanssen and Emslie 1988).

One consequence of this magnetic flux freezing is the concept of magnetic buoyancy. This buoyancy occurs in magnetic flux tubes because the density inside a flux tube is less than in the surrounding atmosphere. This is simply a consequence of the interior pressure being the sum of gas and magnetic pressure, whereas the exterior pressure is due solely to gas pressure. For pressure balance to occur, the total pressure inside and outside the flux tube must be equal, thus a lower density is required within the flux tube (for a constant temperature). An order of magnitude calculation can demonstrate that a hypothetical flux tube will rise through the stellar atmosphere at the local Alfvén speed (e.g. Tandberg-Hanssen and Emslie 1988). If the emerging flux tube is restricted by the footpoints then loop structures are produced. These magnetic loop structures extend out from the stellar surface or photosphere where the loop footpoints are anchored in regions of opposite magnetic polarity, resulting in loops which straddle a *'neutral line'* (i.e. a line where the polarity reverses on the stellar photosphere). Relative motion between these footpoints at the photospheric level may result in the twisting and shearing of these loops and hence increase the stresses in the (current-carrying) magnetic field lines. This may continue until the loop becomes unstable, magnetic field lines reconnect, and settle into a loop configuration of lower energy state. The excess energy liberated then goes on to power the flare, heating the plasma and accelerating particles as it does so.

1.4.1 Types of Stellar Flares

Previous X-ray observations of stars have demonstrated the existence of both short-duration and long-duration flares, similar to those observed on the Sun; i.e. the compact and two-ribbon flares respectively (see Priest 1981). These two classes of flare are differentiated not only by their duration but also by the energy outputs involved, and the magnetic field configurations and mechanisms involved in producing them. Short-duration or compact flares are thought to involve a loop whose *gross* magnetic configuration remains essentially unchanged during the outburst, and which experiences no further energy input during the decay of the flare. The larger, long duration outbursts (two-ribbon flares) with decay times lasting several hours, are thought to be morphologically similar to Solar two-ribbon flares. In these flares, disruptive opening of the magnetic field lines occurs, which then relax back to a lower energy state, gradually releasing their excess energy. YOHKOH observations of two-ribbon flares on the Sun show these flares as an arcade of loops being triggered sequentially (e.g. Tsuneta et al. 1992). Previously this could only be inferred from H_α observations (for example), when two ribbons of emission (from the line of flare footpoints) were seen to move apart away from the neutral line, as the flare progressed (Priest 1981).

The level of good spectral and spatial resolution afforded to observations of Solar flares unfortunately does not extend at present to observations of stellar flares. The possible measurable parameters of an observed stellar flare include the rise and decay times of the flare and the best-fit spectral parameters e.g. temperatures and emission measures. Therefore any derivation of other physical parameters of a stellar flare (e.g. size and density) are modelled by inference and through analogy with the Solar case. Reviews describing the methodology can be found in Haisch (1983), Haisch et al. (1991), and Pallavicini (1995).

The assumptions and methods involved are here briefly introduced and, where needed for the analysis in this thesis, are further developed in subsequent chapters.

1.4.2 Simple Analysis and Inference of Stellar Flare Parameters

Order-of-magnitude estimates of the physical parameters of a compact stellar flare can be made by describing the flare as a simple magnetic loop. It is assumed that energy is impulsively deposited at or near to the top of the loop, and the flare decays via radiative and/or conductive losses. By analogy with the Solar case, further heating does not substantially occur during the flare decay (Moore et al., 1980; Priest 1981; van den Oord & Mewe 1989; Schmitt 1994). An idea of whether radiative or conductive cooling dominates the flare decay can be obtained by examining the ratio of the radiative and conductive cooling times, τ_r and τ_c respectively.[3]

As the flare decays, the ratio of these two cooling times (denoted $\mu = \tau_r/\tau_c$) indicates the dominant cooling process. This ratio is generally unknown and varies during the flare itself (van den Oord & Mewe 1989). However, a simplifying approximation can be made by assuming equal radiative and conductive cooling times i.e. $\mu = 1$ (Haisch 1983). Under this assumption (shown empirically to be a valid one in the Solar case, Moore 1980) the ra-

[3]The radiative cooling time is the time for the flare plasma to cool solely via radiative cooling e.g. $\tau_r = 3k\mathrm{T}/n\Lambda(\mathrm{T})$, where k is Bolzmanns constant, T is the plasma temperature, n is the electron particle density and $\Lambda(\mathrm{T})$ is the plasma emissivity at temperature T. Similarly, the conductive cooling time is the time for the flare plasma to cool solely via conduction e.g. $\tau_c \sim 10^{-10} n\mathrm{L}^2\mathrm{T}^{\frac{-5}{2}}$ (where T is the plasma temperature, L is the flare loop length and n is the density).

diative cooling time can be equated with the observed lightcurve decay time $\tau_d = \tau_r = 3k\mathrm{T}/n\Lambda(\mathrm{T})$. The temperature derived from the spectral fits, can be substituted into this equation and a value for the plasma density can be derived. This density value can then be used with the corresponding emission measure value (found from the spectral fits) to derive a volume for the flare.

Similarly, equating the lightcurve decay time and conductive cooling times ($\tau_d = \tau_c \sim 10^{-10} n \mathrm{L}^2 \mathrm{T}^{\frac{-5}{2}}$) using the value for the previously derived density will produce a value for the loop length L. However for a unique solution, knowledge of both the loop geometry (which is especially important with regard to conductive cooling) and the dominant cooling processes (i.e. value of μ) is required, and these are both unknowable for stellar flares. Van den Oord and Mewe (1989) circumvented this problem when they investigated the quasi-static cooling of flares. In their scenario, the flare cools through a series of constant-pressure loops, in which equilibrium between the input and output energy of the flare exists at each stage. Thus μ can be considered constant, and can be used as a check of quasi-static cooling.

Two-ribbon flares, on the other hand, experience some additional heating during the decay phase. In this type of flare, an initial disruptive opening of the magnetic field line configuration occurs. As these field lines relax back to a lower energy configuration, reconnection occurs at progressively higher altitudes. Reconnection models have thus been used to predict the continuous energy release during the flare. One such model is the Kopp and Poletto model (1984, see chapter 2). This model's main strengths are that no assumptions are made about the initial disruptive event, but instead the continuous energy release caused by reconnection during the decay phase of the flare is modelled. The Kopp and Poletto model has been used succesfully in the analysis of both Solar and stellar two-ribbon flares. Apart from the Sun (Kopp & Poletto 1984)

these include EQ Peg (Poletto, Pallavicini & Kopp 1988; Ottmann & Schmitt 1994), AR Lac and Proxima Centauri (Poletto et al. 1988). This Proxima Centauri flare, however, has *also* been successfully modelled as a compact flare by Reale et al. (1988) highlighting the problem often associated with the low signal-to-noise inherent to most stellar X-ray observations.

Finally, an alternative approach is in the use of detailed hydrodynamic models (e.g. Reale et al. 1988; Peres 1989). In these models detailed calculations of the temperature and density evolution of magnetically confined plasma are carried out. However these models are more generally used for the single loop configurations of compact flare events, and the results are dependent on assumed heating processes.

1.4.3 X-ray flare observations

Tables 1.1 — 1.4 list the major X-ray observations of flares on RS CVn systems reported in the literature to date. For each RS CVn system listed, details of the flare parameters are given. (Where more than one outburst has been observed on a system these are listed in chronological order). The durations of these flares are comparable with those seen on the Sun. However, the greatest differences are in the energies produced – two to five orders of magnitude greater than those observed on the Sun (see van den Oord et al. 1986, 1988). Also noticeable are derived values of flare loop heights, which in some cases are a significant fraction of the stellar radius (unlike in the case of the Sun). As in the case of quiescent coronal loops, the lower surface gravities in these evolved systems must play an important role in determining these loop heights.

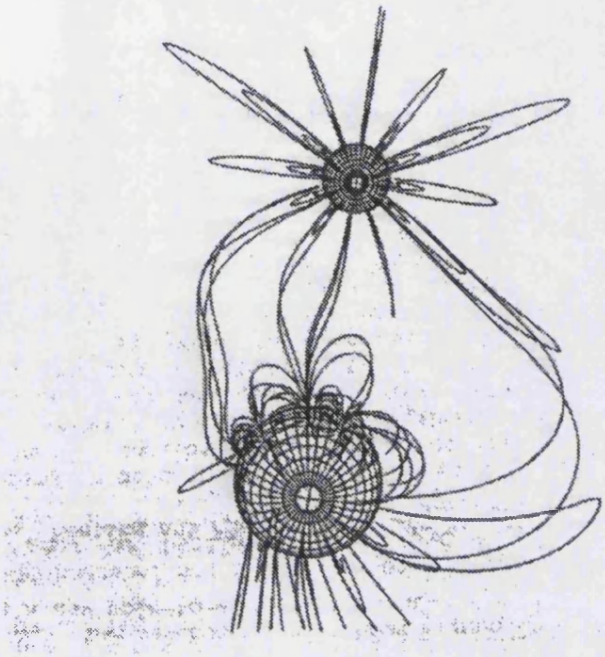

Figure 1.5: *Representation of inter-binary loops according to the Uchida-Sakurai model. Taken from Uchida & Sakurai 1985.*

These larger-than-Solar flares have fuelled much speculation over the years as to whether inter-binary flaring can occur within RS CVn systems. Theoretical investigations have hinted that the interactions between the magnetic fields of the two components of RS CVn systems would result in magnetic loop configurations connecting both stars (e.g.Uchida & Sakurai 1985; see Fig. 1.5).

These speculations are strengthened by our understanding of the conditions within the RS CVn system environment, and further supported by a number of flare observations made at various wavelengths. These include radio (Feldman et al. 1978; Owen et al. 1978; Feldman, 1983) and UV (Simon et al., 1980). Other observations include those by Bopp (1983) of HR 1099 in H_α which showed no orbital modulation, indicating that the emitting volume was on a

Table 1.1: Details of the major X-ray flares observed in RS CVn systems and reported in the literature. (Although Algol is not an RS CVn system, the secondary is chromospherically active and so has been included in this table). The bracketed numbers in the Notes/refs. section refer to the references listed in Table 1.5. The following abbreviations have been used: T refers to Temperature; EM is the Emission Measure; V is the flare volume; B refers to magnetic field strength; H the flare loop height; L_R is the flare loop length calculated using Reale et als. method (1997); L_{ecl} is the flare loop length calculated using the self-eclipse of the lightcurve to constrain the flare geometry; E is the energy released during the flare; n_e is the electron density; $\tau_{\rm eff}, \tau_d, \tau_r$ refer to the effective and lightcurve decay times and the flare rise time respectively.

Star/ Flare Date	Flare Parameters[a] (Spectral/Geometrical)		Notes/ refs.
HR 1099			
17 Oct 1983	T=43 MK	EM=9×10^{53}cm^{-3}	EXOSAT (ME, LE): 1T Bremms model.
	$\tau_r \sim$ 1000s	$\tau_d \sim$ 1500s	HR steepens and declines with
	E$\sim 10^{34}$ergs	$n_e \sim 4.4 \times 10^{11}$ cm^{-3}	heating and cooling of the flare.
	V$\sim 5 \times 10^{30}$cm^3	H $\lesssim 3 \times 10^{10}$ cm	
	B$\sim$ 360 G		[1]
UX Ari			
24 Jul 1987	T=79 MK	EM=95×10^{53}cm^{-3}	GINGA (LAC): 1T Bremms + Fe line model.
	E$\sim 10^{37}$ergs	$n_e \lesssim 2 \times 10^{10}$cm^{-3}	Quiescent spectra subtracted.
	V$\sim 2 \times 10^{34}$cm^3		Continued heating or long decay
		B$\sim$ 140—360 G	time for flare.
			Flare = two-ribbon. [2]
29 Aug 1994	T=80 MK	EM=32×10^{53}cm^{-3}	ASCA: 3T MEKAL[b] model.
		$n_e \sim 10^{11}$cm^{-3}	
	H$\sim 5.2 times 10^{11}$ cm		Fe abundance increase during
		B $\gtrsim$ 500 G	flare decay.
		$\tau_d \sim$ 3600s	Flare = two-ribbon. [3]

[a] Where two-temperature (2T) or multi-temperature spectral models have been used Temperatures and Emission Measures(EM) quoted are the peak values for the hottest temperature component.

[b] MEKAL: Mewe-Kaastra-Liedahl Thermal Plasma emission model

Table 1.2: *Major X-ray flares: continued.*

Star/ Flare Date	Flare Parameters (Spectral/Geometrical)		Notes/ refs.
σ^2 CrB			
17 Aug 1980	T$\sim$25 MK	EM=3 x 10^{53}cm^{-3}	*Einstein* (SSS):
	$\tau_d \gtrsim$2000s	E=2 x 10^{34}ergs	1T RS[a] model
	H$\sim$ 1.1 x 10^{10}cm		[4]
29 Sep 1983	T=95 MK	EM=5.7 x 10^{53}cm^{-3}	EXOSAT: 1T RS model
	$\tau_d \sim$ 1700s	$\tau_r \sim$ 180s	Quiescent spectra subtracted from flare spectra.
	H=1.4 x 10^{10}cm	E=2.4 x 10^{34} ergs	Flare duration $\sim$9 ks.
	$n_e \sim 6 \times 10^{11}$cm^{-3}	V=6.9 x 10^{29} cm^3	Hardness Ratio falls during flare decay.
	B=630 G		Flare = compact [5]
28 Jun 1988	T=32 MK	EM=1.4 x 10^{53}cm^{-3}	GINGA: 2T RS model
			Incomplete flare coverage
			Duration $\gtrsim$7.2ks [6]
II Peg			
22 Jul 1985	T=37 MK	EM=7.5 x 10^{53}cm^{-3}	EXOSAT (ME, LE): 1T & 2T RS models applied.
	$\tau_r \gtrsim$7000s	$\tau_d \sim$ 31000s	Both models fit equally well, although flare peak
	E > 1.6 x 10^{35}ergs	$n_e \sim 3 \times 10^{10}$cm^{-3}	was best fitted by 1T model
	V$\sim$ 1 x 10^{33}cm^3	H$\sim$ 1 x 10^{11} cm	(Quiescent spectra subtracted).
		$\sim 0.7R_*$	Duration$\sim$90ks [7]
17 Aug 1989	T=65 MK	EM=30 x 10^{53}cm^{-3}	GINGA (LAC): 1T RS + Fe line model.
	τ_{eff} = 2132s	V=6.1 x 10^{30}cm^3	Simultaneously observed in UV, optical & radio.
	E$\sim$ 10^{35}ergs	$n_e \sim$ 7.5 x 10^{11}cm^{-3}	Was also a strong optical flare.
	V$\sim$ 1 x 10^{33}cm^3	H$\sim$ 3 x 10^{10}cm	Fe abundance dropped during
	B $\gtrsim$522 G		flare decay by 33%.
			Flare = two-ribbon. [8]
19 Dec 1994	T=36 MK	EM=2 x 10^{53}cm^{-3}	ASCA: 2T MEKAL for quiescent + 1T MEKAL for flare.
	$\tau_r \lesssim$3600s	V=3 x 10^{31}cm^3	
	E$\sim$ 2.4 x 10^{35}ergs	$n_e \sim 0.8 \times 10^{11}$cm^{-3}	
	$\tau_d \lesssim$10800s	H$\sim$ 8 x 10^{10}cm	Fe abundance increased during
	B $\gtrsim$140 G		
			Flare = two-ribbon. [9]
5-6 Dec 1997		$E_{Tot} \sim 4 \times 10^{35}$erg	BeppoSAX
		$\tau_d \sim$ 19ks	Incomplete flare decay coverage
			Duration $\gtrsim$36ks [10]

[a] RS: Raymond & Smith Thermal Plasma emission model

Table 1.3: *Major X-ray flares: continued.*

Star/ Flare Date	Flare Parameters (Spectral/Geometrical)		Notes/ refs.
Algol			
9 Aug 1979	T=42 MK	EM=6 x 10^{53}cm^{-3}	*Einstein* (SSS): 2T RS model
			Duration ~ 43 ks [11]
18/19 Aug 1983	T=60 MK	EM=10 x 10^{53}cm^{-3}	EXOSAT (TGS, ME, LE):
	E=10^{35}ergs	τ_d = 7000s	1T Bremms. + Fe line
	V=6 x 10^{31}cm^3	n_e = 3 x 10^{11}cm^{-3}	Hardness Ratio (HR) decays during event
	B> 200G	H~ 5 x 10^{10}cm	Duration ~ 14.4 ks [12]
18/19 Aug 1983	T=78 MK	EM=8 x 10^{53}cm^{-3}	EXOSAT: Reanalysis of [12]
	τ_{eff} = 5618s	V=1.4 x 10^{31}cm^3	1T RS model: (Quiescent spectra subtracted
	H=5.1 x 10^{10}cm		from flare spectra).
	=0.2R$_*$		Flare = two-ribbon [13]
14 Jun 1989	T=55 MK	EM=13 x 10^{53}cm^{-3}	GINGA (LAC):
	τ_d = 22500s	H~ 2 x 10^{11}cm	1T Bremms + Fe line model:
	n_e ~ 5 x 10^{10}cm^{-3}	=0.8R$_*$	Quiescent spectra subtracted
			Flare = two-ribbon [14]
19 Aug 1992	T=44 MK	EM=108 x 10^{53}cm^{-3}	ROSAT (PSPC): 1T RS model with low z
	E=7 x 10^{36}ergs	τ_{eff} = 28800s	Duration ~ 14.4 ks
	V=1.3 x 10^{34}cm^3	H=1.6 x 10^{11}cm	N_h increase by factor 2 during
		=0.7R$_*$	flare decay.
			Flare = two-ribbon [15]
30 Aug 1997	T=140 MK	EM=133 x 10^{53}cm^{-3}	ASCA: 3T MEKAL model comprising
	E=1.4 x 10^{37}ergs	τ_{eff} = 56000s	2T Quiescent (*fixed*) plus
		L_R=4.7 – 12.0 x 10^{11}cm	1T flare spectra.
		L_{ecl}=2.4 x 10^{11}cm	N_h and abundance increase during flare decay.
			Flare = compact [16]

scale comparable or greater than the stellar radius or that the emission was possibly emanating from between the two stars. Large broadening of the H_α line ($\sim$ 400 km s^{-1}) and asymmetries in the line profile also suggested mass motion.

Table 1.4: *Major X-ray flares: continued.*

Star/ Flare Date	Flare Parameters (Spectral/Geometrical)		Notes/ refs.
AR Lac			
19 Jun 1990	T=39 MK	EM=100 x 10^{53}cm^{-3}	ROSAT (PSPC): 3T RS model comprising
	τ_{eff} = 15400s	V$\sim$ 1.2 x 10^{33}cm^3	2T Quiescent (*fixed*) plus
	E$\sim$ 10^{37}ergs		1T flare spectra.
	H$\sim$ 8 x 10^{10}cm (Γ = 1) = 0.4R_*		Duration $\sim$ 29ks
	H$\sim$ 4 x 10^{10}cm (Γ = 10)		Flare = two-ribbon. [17]
11 Nov 1997	T=26 MK	EM=3.1 x 10^{53}cm^{-3}	BeppoSAX:
	τ_d = 23000s		1T flare spectra.
	E$\sim$ 2^{35}ergs		[18]
HD 8357			
13 Jan 1978	T=30 MK	EM=500 x 10^{53}cm^{-3}	HEAO-A1 (Sky Survey):
	$\tau_d \sim$ 4500s	$n_e \sim 2 \times 10^{11}$cm^{-3}	
	B$\sim$ 200 G	H$\sim$ (6—9)x10^{10} cm	
	E$\sim$ 10^{36}ergs		[19]
HU Vir			
15 Jun 1994	T$\sim$ 10 MK	E$\sim$ 7.7 x 10^{36}ergs	ROSAT (HRI):
		$n_e \sim 2.2 \times 10^{10}$cm^{-3}	Duration $\sim$ 130ks.
	B$\sim$ 200 G	H$\sim$ 5.2x10^{11} cm	
			[20]
DM UMa			
5/6 Nov 1977	T$\sim$ 10 MK	E$\sim$ 4 x 10^{37}ergs	HEAO-A2:
		$\tau_r \sim$ 7200s	Duration $\lesssim$ 173ks.
			[21]

1.4.4 In This Thesis

This chapter has set out a brief overview of our current understanding of X-ray flares observed on RS CVn systems. It is not, nor is it intended to be, a complete review as the subject matter is vast. The main body of this thesis presents observations made with the PSPC and WFC instruments onboard the ROSAT satellite of a number of flare outbursts from two of these systems. Chapter 2 discusses the first outburst, observed on the system HR 5110. The method of van den Oord et al. to derive an effective decay time for flares is extended

to include the effects of heating and this is then applied to the observation in order to constrain the flare parameters. Follow-up observations of HR 5110 are presented in Chapter 3, where a number of flare events were observed on the system HR 5110. Thus a comparison can be made of separate flare events. In Chapter 4, a similar long-duration flare event on another RS CVn system, CF Tucanae, is presented; in this case the different system inclination allows for a more thorough investigation of the flare phenomenon. The observations presented in Chapter 4 were of sufficient duration to allow investigation of the post-flare emission, and this is detailed in Chapter 5. Finally in Chapter 6 the main results of the previous chapters are brought together in order to compare them and suggest a number of ways in which this work can be extended.

#	References
1	Barstow 1985
2	Tsuru et al. 1989
3	Gudel et al. 1999
4	Agrawal, Rao & Riegler 1986
5	van den Oord, Mewe & Brinkman 1988
6	Stern et al. 1992b
7	Tagliaferri et al. 1991
8	Doyle et al. 1991,1992a,b
9	Mewe et al. 1997
10	Covino et al. 2000
11	White et al. 1980
12	White et al. 1986
13	van den Oord & Mewe 1989
14	Stern et al. 1992a
15	Ottmann & Schmitt 1996
16	Favata & Schmitt 1999
17	Ottmann & Schmitt 1994
18	Rodono et al. 1999
19	Ambruster, Synder & Wood 1984
20	Endl et al. 97
21	Charles, Walter & Bowyer 1979

Table 1.5: *References for the major X-ray flares observed in RS CVn systems.*

Chapter 2

HR 5110—A Source Of Inter-Binary Flaring?

... Made weak by time and fate, but strong in will
To strive, to seek, to find, and not to yield.

"Ulysses", Alfred Lord Tennyson

2.1 INTRODUCTION

HR 5110 ($\alpha_{2000.0} = 13^h\,34^m\,47.8^s$; $\delta_{2000.0} = 37°\,10'\,57''$) is a bright (V = 4.97) double-lined spectroscopic binary. Slettebak (1955) originally classified HR 5110 as a single F2IV star, but it was later classified as a member of the RS CVn systems (Hall 1976) mainly due to the strong CaII H and K emission observed from the secondary (Conti 1967). Conti's spectrosopic study gave a mass ratio

of M_2/M_1=0.28, which together with the assumption that $M_1 = 1.5M_\odot$ and an orbital period of 2.61 days, suggested an orbital inclination of 13°. Conti used this mass ratio, combined with the parallax determined by Jenkins (1963) to deduce that the secondary has an effective temperature of 4000 K and fills its Roche lobe. This view is supported by the multi-wavelength study carried out by Little-Marenin et al. (1986) who argue that HR 5110 can also be considered to be an Algol system seen nearly pole-on. High-resolution spectroscopy with full orbital phase coverage of the Hα emission enabled Eker and Doherty (1987) to detect lines from the secondary for the first time. This provided a new estimate for the mass ratio for HR 5110 of M_2/M_1=0.54, a slightly smaller inclination angle of 8.9°, and spectral types of F2IV and K2IV for the primary and secondary components respectively.

Some Algol systems also contain secondaries which rotate synchronously and are characterized by rapid rotation and deep convective zones. These systems should therefore display increased chromospheric and transition region activity (Hall 1989), best observed in the UV portion of the spectrum. However, in most Algol systems any chromospheric activity from the secondary is normally difficult to detect because the UV spectrum is dominated by the much hotter primary, an accretion source and/or a hot gas stream. An inspection of 5 Uniform Low Dispersion Archive IUE spectra of HR 5110 was made by myself: this revealed no indication of an accretion source or gas stream as evinced by the lack of absorption in transition-region lines modulated on the orbital period.

Photometric variability of the order ΔV=0.01 mag. modulated with the orbital period was detected in HR 5110 by Hall et al. (1978) who attributed it to a reflection effect, rather than a distortion wave due to darker starspots which is characteristic of most RS CVn binaries.

A number of strong radio outbursts from the star between 1979 and 1983 gave further weight to the RS CVn classification (Viner & Feldman 1979; Feldman 1983) as did the discovery of a reversal of circular polarization by Mutel et al. (1985) during the 1983 outburst, a characteristic of radio emission from RS CVns (see Section 1.3.4).

Although HR 5110 had been observed with the *Einstein* satellite with a count-rate of 1.54±0.04 ct/s in the IPC detector, the interpretation of the spectrum had been hampered by low signal-to-noise. With the launch of ROSAT and its greater sensitivity and better spectral resolution (see Appendix B), much more detailed studies could be carried out, and these form the subject matter of this chapter. Any work carried out by co-workers has been indicated in the text.

2.2 THE DATA

The data presented in this chapter were obtained from both survey and pointed ROSAT observations made with the PSPC and WFC instruments. During the initial six-month survey phase of the ROSAT mission, the whole sky was scanned, (see Appendix B), and this was followed by the pointed phase of the mission. A pointed observation of one of the Lockman 'holes' (a region of low neutral hydrogen galactic column density; $N_{\rm H} = 6.5\times10^{19}\,{\rm cm}^{-2}$) was made with both the PSPC and WFC beginning on 1991 June 23 with the aim of performing a deep extragalactic survey (Branduardi-Raymont et al. 1994). The principal investigator for the proposal of this pointed observation was Branduardi-Raymont. The total exposure time was 73ks taken over a period of $\sim$ 3 days. HR 5110 lies within the 2° diameter field of view of the PSPC, and at the time of observation was found to be in a state of substantial activity. In the following sections I will describe the HR5110 time series extracted from

both the survey and pointed observations and then will describe the subsequent spectral analyses. I used the ASTERIX suite of programs (Saxton 1991) to analyse the ROSAT data.

2.3 THE ANALYSIS

2.3.1 The WFC Survey Time-Series

The field of view of the WFC is 5°, more than twice the diameter of the PSPC field of view (2°). I estimated the background contamination of the source signal from an area displaced along the scan path. In this way, the background and source counts were measured within a few seconds of time of each other, minimizing the differences due to temporal variations in the background. This is important because background variability in the WFC was apparent on a timescale of the ROSAT orbital period (approximately 96 minutes) or less, and can significantly affect low-count-rate sources (Wonnacott 1994).

I retrieved the WFC survey data from the WFC Survey archive. I produced two images, one for the S1 band (90–185 eV) and one for the S2 band (62–111 eV). For each band, the counts were summed in two circular regions of 8 arcmin radius. One circle was centred on the source and the other one was displaced by 10 arcmin along the WFC scan direction. I employed the method of Kraft, Burrows, & Nousek (1990), which uses Bayesian statistics to calculate the Poisson errors, to obtain count-rates of 0.033 ± 0.006 ct/s and 0.037 ± 0.007 ct/s, for the S1 and S2 bands respectively with errors at the 68% confidence level. This gives an S1/S2 ratio of $\sim$ 1, which for the WFC survey is typical of nearby active stars. These fluxes for HR 5110 compare well with those in Pounds et al. (1993) of $0.029 \pm$ 0.005 ct/s and $0.042 \pm$ 0.006 ct/s respectively, which were produced by an automated extraction process. The WFC survey

count-rates for both the S1a and S2a filters are shown in Figure 2.1. Fitting a constant count-rate to the WFC data gives χ^2_ν values of 0.964 (with 30 degrees of freedom) and 0.785 (with 34 degrees of freedom) for the S1a and S2a filters respectively, so there is no evidence of variability.

2.3.2 The Survey PSPC Time-Series.

I requested the corresponding Survey PSPC time-series from Max-Planck-Institut für Extraterrestrische Physik, and "as the data were then still proprietory", these were extracted by Dr. S. Schaedt (1993). He extracted them using source and background circles of 5 arcmin radii, with the background circle displaced along the scan direction, as in the case for the WFC survey data extraction. For a full description of standard extraction of survey PSPC data, see Belloni et al. (1994).

The PSPC time-series is shown together with the survey WFC time-series in Figure 2.1. Although most of the data points seem to straddle the mean count-rate value of 2.28 $\pm$ 0.22 ct/s to within 1σ, note that the outermost data points seem to suggest a slope, in that the early points are systematically higher than the mean, and the later points are systematically lower. A least-squares fit performed on the data produced a best-fit line with a gradient of -0.37 ± 0.14 ct/s/day, corresponding to a 2.6σ level of significance.

In order to check whether HR 5110 was in a state of quiescence during the survey observation, I converted the HR 5110 ROSAT PSPC survey count-rate to the *Einstein* IPC bandpass using the PIMMS program (Mukai 1993) assuming a four-temperature Raymond and Smith plasma model derived from the PSPC survey observations (see section 2.3.5 and table 2.3). The predicted IPC count-rate of 0.81 $\pm$ 0.06 ct/s is about half the value observed in the IPC (1.54 $\pm$ 0.04 ct/s—IPC catalogue designation IPC 133234+3726). This

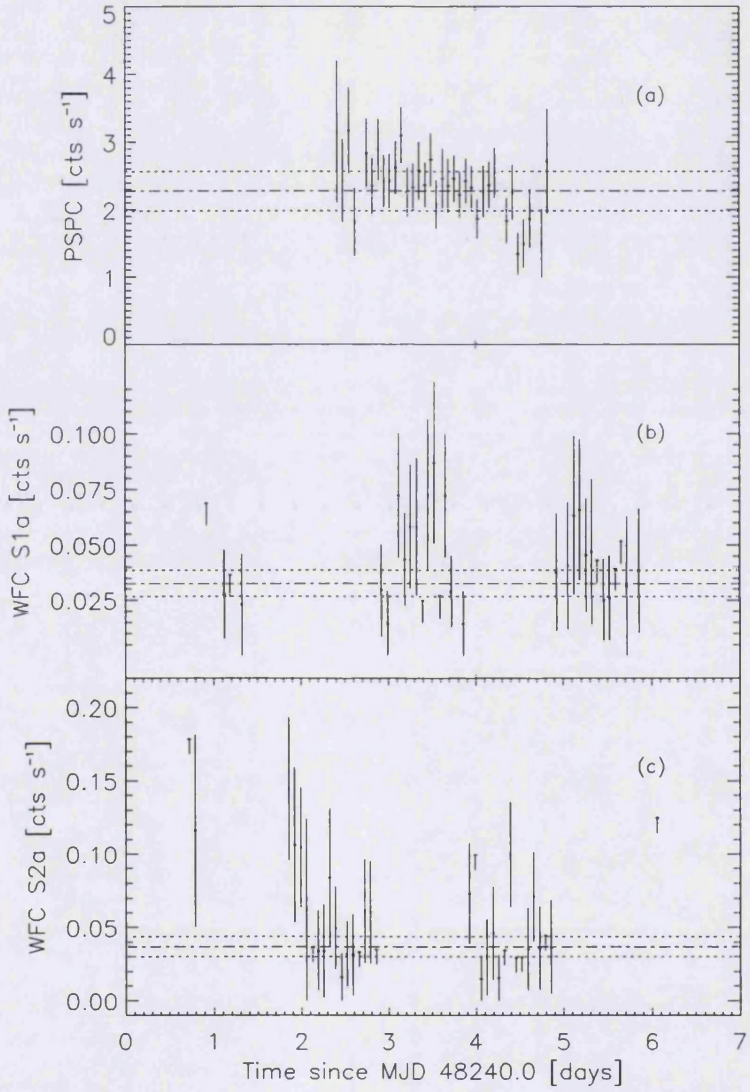

Figure 2.1: *PSPC and WFC Survey observations of HR 5110. count-rates shown are for (a) the PSPC, (b) the WFC S1a filter and (c) the WFC S2a filter. In each figure the mean count-rate and 1 sigma level are indicated by dash-dot and dotted lines respectively. Data points showing only the lower half of an error bar are upper-limits.*

indicates that during the original *Einstein* observation HR 5110 was not in quiescence, but *may* have been when observed during the PSPC survey.

2.3.3 The Pointed WFC Time-Series.

Only the S1a filter was used during the pointed observation. I extracted the pointed WFC time-series from a circular region of 16-arcmin radius centred on the source position. The background was taken from an annulus with outer radius of 33 arcmin and inner radius of 17 arcmin, again centred on the source. As no other sources were detected in the WFC image, the large area was used to improve the background estimate. I corrected for the WFC efficiency degradation, (by a factor of 5 Willingdale, 1991) and obtained a mean count-rate of 0.118 ± 0.012 ct/s for the S1a filter. This is an increase by a factor of ~ 3.6 over the survey count-rate. The pointed WFC time-series is shown in Figure 2.2 along with the pointed PSPC observation and hardness ratio. The gaps present in the WFC time-series are due to periods when the UV calibration filter was in place.

2.3.4 The Pointed PSPC Time-Series

I extracted the PSPC time-series (and spectra) of HR 5110 after excluding times of higher background (leaving $\sim$ 67 ks of 'clean' data). In the PSPC image another fainter source (with a mean count-rate of 0.171 ± 0.003 ct/s) was found to lie 8.1 arcmin from HR 5110. So that no source confusion would occur, I selected a 5.5 arcmin-radius source circle, in which 98% of the source photons were included, to extract the HR 5110 PSPC time-series. (This extra source is *not* present in the WFC image.) I therefore applied a correction for the remaining 2% of the photons.

I then selected a 12 arcmin-radius background region away from both

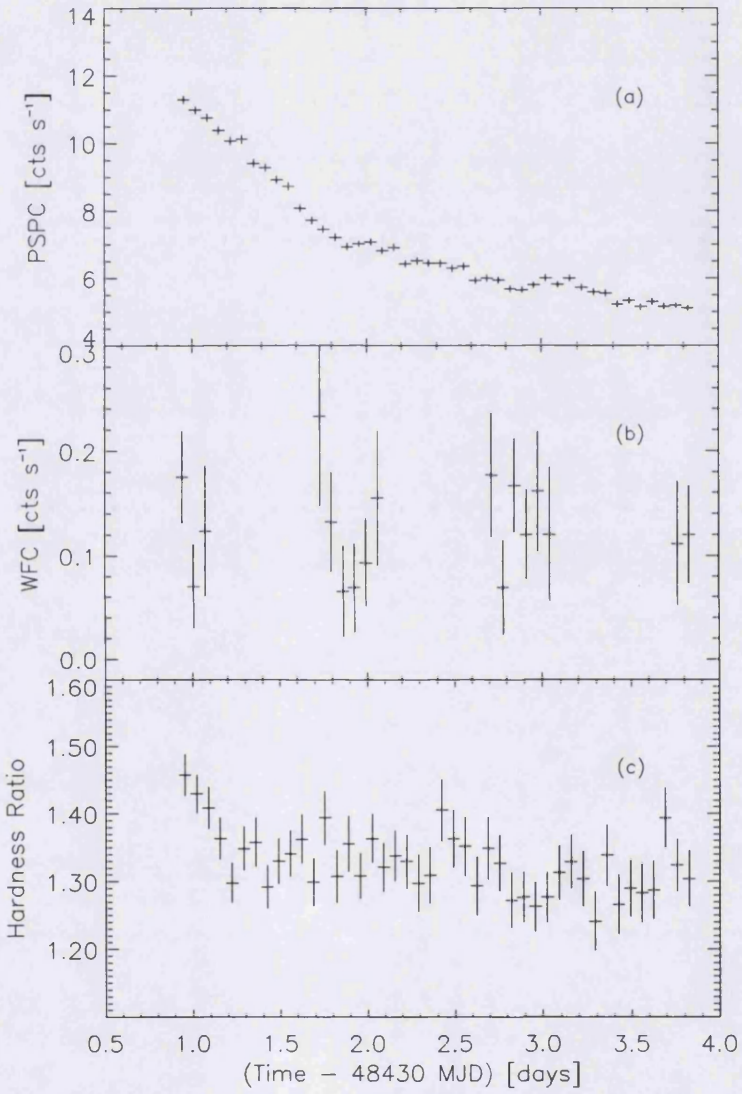

Figure 2.2: *Pointed observations of HR 5110.(a) The PSPC count rate. Note the sharp change in decay rate at ∼ 1.9 days. (b) The WFC count-rate remains constant throughout the observation although at a higher level than the survey observation. (c) The hardness ratio, defined as the hard band counts divided by the soft band counts (hard band 0.29 - 2.00 keV, soft band 0.1 - 0.28 keV). Note that the hardness ratio remains approximately constant throughout the*

sources and the counts were summed and normalised to the source area before background subtraction, exposure correction, and correction for vignetting and deadtime were performed. A Scargle periodogram (from the DIPSO package) was performed on the data binned at 100 seconds time resolution and shows a peak at the ROSAT orbital period of 96.194 minutes with no significant power at other periods: I therefore rebinned the data on this orbital period, and centred on the middle of the time bin. The PSPC time-series in Figure 2.2 shows that the count-rate declined from 11.30 ± 0.12 ct/s, at the start of the observation to 5.11 ± 0.08 ct/s (68% errors) by the end. The PSPC count-rate shows a substantial increase over the all-sky survey value, and was presumably already in a state of decline when the observations started.

I defined a soft and hard band in terms of the Pulse Height Amplitude (PHA) channels below and above the instrumental carbon edge (0.284 keV) respectively, in order to obtain a hardness ratio. However channels 1–11 and 200–256 were not used as the former are unreliable and the latter are heavily contaminated by particle background. The resulting hardness ratio is shown in Figure 2.2 as a function of time. The first three data points show a slight decay in the hardness ratio. Subsequent points exhibit very slight variations about the mean value of 1.32 ± 0.01. If the first three points are ignored, a χ^2_ν of 1.08 (43 degrees of freedom) is obtained for an assumed constant hardness ratio, indicating that the slight variations are not statistically significant. As the hardness ratio can be considered a crude temperature diagnostic, this shows that the temperature remained constant during most of the decay.

2.3.5 The Spectral Analysis

In order to see how the spectral properties of the outburst varied with time, I divided the pointed PSPC time-series into four time-bins, by splitting the time-

Table 2.1: *Table detailing the time bins within which the outburst spectra, (N°·1-4), and survey spectra (denoted S), were extracted.*

#	Start Time [MJD]	End Time [MJD]	Integration Time [ks]	Total counts in Bin
1	48430.9211	48431.4535	14.5	261085
2	48431.4535	48432.0322	13.6	193894
3	48432.0322	48432.9581	21.2	241733
4	48432.9581	48433.8840	24.0	233601
S	48242.3888	48244.8503	0.6	2325

series near the point where the decay rate suddenly changes, at t = 48431.84 days, and then halving each section again. (The low number of bins was used to ensure a very high signal-to-noise ratio.) The times for each bin are given in table 2.1. Also included in the table are the times for the survey data.

I extracted a PSPC spectrum for each time-bin. For the pointed PSPC data, I used a 5.5-arcmin radius for the source and an 8.1-arcmin radius for the background, situated away from the source. The survey PSPC spectrum was extracted by Dr. Schaedt as for the time-series, and the data set was made available to me. I carried out background subtraction and exposure correction on all of the five spectra, and these I then converted to a format which could be used by the XSPEC spectral fitting package (Shafer et al. 1993). In order to compensate for the random uncertainties in the PSPC calibration, the error-bars on the data points were increased by 2%, as recommended by Turner & George (1993).

I then binned in energy such that each bin within the spectrum contained a minimum of 100 counts.

I then fitted each spectrum, i.e. the four pointed (outburst) spectra and that of the survey, with a variety of single and multi-component spectral mod-

els. These comprised of all single and pairwise combinations of Raymond and Smith plasmas, blackbodies, bremmstrahlung emission, and power-law models. No single choice of model fitted each of the five spectra consistently well, apart from the following two models:

1. a combined Raymond and Smith plasma and power-law model with interstellar column and all parameters left free (see table 2.2), and

2. a four-temperature Raymond and Smith optically thin plasma model, with the four *fixed* temperatures of 10^6, 3×10^6, 10^7, and 3×10^7K, the emission measures, and column density (i.e. five free parameters), allowed to vary (see Table 2.3 and Figure 2.3). These four temperatures were chosen to cover the PSPC energy range, and are equally spaced in log space, with the initial temperature being chosen arbitrarily. (An examination of the validity of this method is presented in Appendix A).

All other models were statistically substantially worse as judged by their χ^2_ν values with typical values of $\gtrsim 2$. (In the case of the survey spectrum, however, a two-temperature Raymond and Smith plasma model did give a good fit with a χ^2_ν of 0.96 with 5 degrees of freedom, primarily due to the lower signal-to-noise.)

A similar choice of models was arrived at by Drake et al. (1994) in fitting X-ray data from a sample of Algol systems. They found that although two-temperature thermal plasma models produced best spectral fits to both *Einstein* and BBXRT data of their sample, this was not the case for ROSAT PSPC data of these systems. Instead they found that a multi-temperature thermal plasma model (in their case using three temperatures) and a thermal plus power-law component model provided the best fits to the PSPC data of the Algol systems. Their three-temperature fits found two of the components

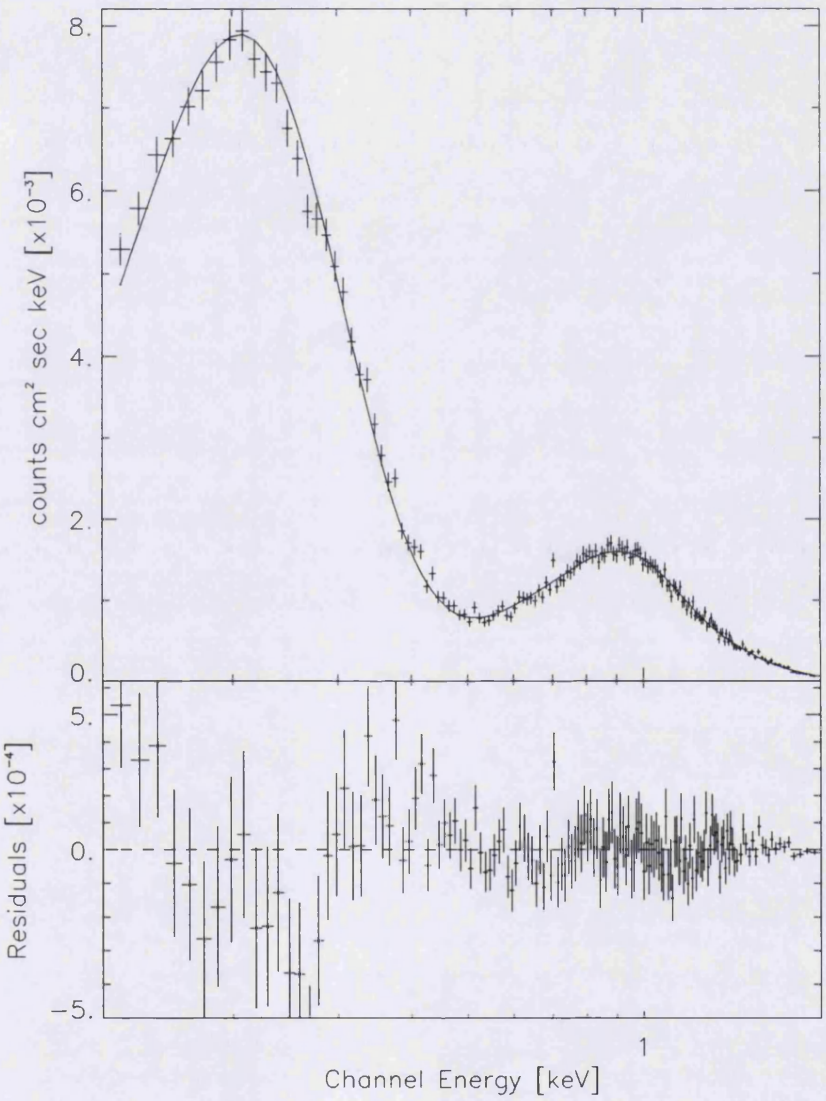

Figure 2.3: *Fit to the outburst spectrum (third time bin — see table 2.1), using a four-temperature Raymond and Smith model with interstellar column. The* χ^2_ν *for this fit was 1.21 for 147 degrees of freedom (see table 2.3 for details).*

to be the same as those found in the *Einstein* and BBXRT data, plus a much softer ($\sim$ 0.15 keV) component. Although the actual nature of the soft powerlaw component itself is unclear at present, it may form the tail end of a softer thermal component. It may also be indicative of emission from a non-thermal distribution of particles, possibly as part of the mass transfer process within the Algol systems. This would, of course, have implications for the classification of HR 5110 as an Algol-type system. Interpretation of this however, is hindered by the poor understanding of the soft calibration of the PSPC, as the powerlaw component may possibly be an artifact of this (see below).

Fits to Combined PSPC and WFC Spectra

In order to extend the spectral coverage to lower energies than the PSPC, I attempted to fit combined WFC and PSPC spectra. To do this, I created a one-channel 'WFC spectrum' by inserting the pointed WFC S1 count-rate into a WFC spectral template. This I then converted to a format suitable for use with the XSPEC package. Similar spectral points were created for the survey WFC S1 and S2 count-rates. I repeated the spectral fits for the combined PSPC and WFC spectra, but these produced fits with typical $\chi^2_\nu \gtrsim 17$ *even for the previously found best fit models.*

Note that a discrepency between the PSPC and WFC calibrations has been highlighted by Napiwotzki et al. (1993), who used high-quality stellar parameters for the white dwarf HZ 43A to check the X-ray and EUV flux calibrations of ROSAT. By comparing synthetic and measured count rates from HZ 43A they showed that the calibration of the ROSAT WFC filters is very reliable, with count-rates agreeing with their model to 6%, well within their errors. Count-rates observed with the PSPC, however were too low by a factor of 1.77. (A more extensive survey of DA white dwarfs by Jordan et al.

(1994) has confirmed this result).

Thus, in order to see if improved spectral fits could be obtained for the combined PSPC and WFC spectra (and as a test of the WFC/PSPC calibration) I multiplied the counts within the PSPC spectra by this factor of 1.77, converted these spectra to XSPEC format and combined them with the WFC spectra points before refitting. This time acceptable fits were obtained, with the best fits again provided by a combined Raymond and Smith and powerlaw model or a four temperature Raymond and Smith optically thin thermal plasma model. The results of these fits are found in tables 2.4 and 2.5 respectively, along with their corresponding survey fits.

Notice that in comparing the results from tables 2.2 and 2.4 the spectral *shapes* (as dictated by the temperatures and photon indices) are very similar. The difference arises in the comparison of the emission measures or powerlaw normalisation and hydrogen column density where there is a trade-off between them. There is more consistency between survey values of column density and those found during the outburst for the spectral results incorporating the WFC spectral point (i.e. using the modified PSPC data). This is due to the greater sensitivity of the WFC to column density.

Note however, that although the soft portion of the PSPC response is not finally calibrated, calibration problems with the WFC were also being experienced at about the time of the pointed deep observation (Barstow 1994). In this case, the PSPC/WFC discrepancy cannot therefore be firmly ascribed to one or other instrument. Furthermore, the PSPC calibration test performed by Napiwotzki et al. is only valid up to $\sim 0.35\,\mathrm{keV}$, as HZ 43 is a very soft source. Therefore I repeated the combined spectral fits with only the PSPC channels down to 0.35 keV, modified by the correction factor (1.77). This produced very poor fits (with best $\chi^2_\nu \sim 7$), due to the step introduced by

the factor 1.77 being applied to only the lower energy channels. Thus any correction to the calibration must be smoother than a simple step function.

As a further test, and also to see why the PSPC count-rate halved whilst the WFC count-rate remained essentially constant during the observation, I folded the *uncorrected* PSPC light curve through the WFC S1 filter band-pass using the two best-fit spectral models. Figure 2.4 shows that variation in the PSPC count-rate, is smoothed out when folded through the WFC S1 filter, and is lost within the Poisson noise. This results in the WFC light curve being succesfully reproduced *to within the errors*, indicating that the WFC light curve is simply the EUV counterpart of the emitted X-rays, originating from the same source.

Thus the spectral analysis, which shows a discrepancy between the PSPC and WFC spectra, and the results of folding the PSPC light curve through the WFC band-pass seem to contradict each other. This may be reconciled by remembering that both the spectral analysis and the reproduction of the light curve has involved binning the data in two different ways. The WFC data were binned on the spacecraft orbital period. This produced a light curve whose data points have large error bars. Good fit statistics are obtained therefore, when the WFC light curve is fitted with a model light curve, produced by folding the PSPC count-rate through the WFC S1 filter. In the spectral analysis however, the data were binned over a number of orbital periods, increasing the number of photons in each bin and hence *reducing the size of the error bars on the data points.* When performing a combined PSPC/WFC fit, the reduced errors result in poor fits.

Correction for the PSPC/WFC discrepancy is likely to be considerably more involved than simply multiplying the PSPC points by a constant correction factor, and any attempt to allow for this in this analysis will necessarily

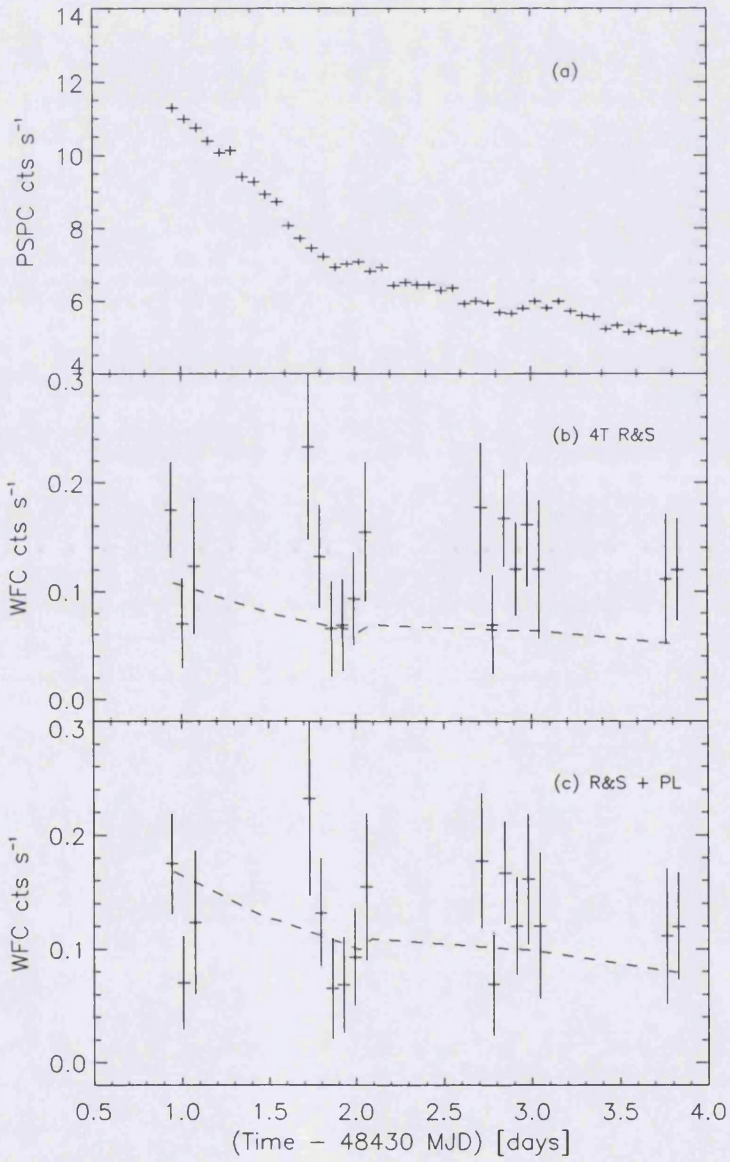

Figure 2.4: *This plot shows the simulated count-rates obtained by folding the PSPC light curve through the WFC S1 filter, using the best fit spectral models. (a) The uncorrected PSPC light curve. (b)—(c) The observed WFC light curve, overplotted with the simulated count-rates. The models used are (b) a four-temperature thermal plasma, and (c) a combined thermal plasma with a powerlaw component.*

add uncertainty. Subsequent calculations in this chapter will therefore use the results of the two best fit models for the *uncorrected* PSPC data, found in tables 2.2 and 2.3 along with their corresponding survey fits, and should be interpreted with the discrepancy firmly in mind.

2.4 DISCUSSION

As mentioned in chapter 1, Swank et al. (1981) found that two-temperature, optically-thin thermal plasma models fitted spectra obtained from their sample of chromospherically active stars observed with *Einstein* quite well ($\chi^2_\nu \sim 1.26$). Similar results were reported by Majer et al. (1986), also using *Einstein* data, and Dempsey et al. (1993) who conducted a study of the X-ray properties of RS CVn stars using the ROSAT all-sky survey data. The fact that a two-temperature thermal plasma model also gives a good fit to the survey data is at least consistent with previous results. However, the use of single-temperature or two-temperature models for chromospherically active stars almost certainly does not reflect the true physical conditions present within stellar coronæ, and EXOSAT data showed evidence that multi-temperature coronal structure exists within RS CVns (Pasquini et al. 1989). Very high signal-to-noise ratio data obtained with ROSAT and EUVE have also shown that fits obtained with simple two-temperature models are no longer acceptable: using a differential emission measure (DEM) method may give statistically better, and physically more realistic, fits (Jeffries, 1992; Dupree et al., 1993).

The four-temperature Raymond and Smith model samples the emission measure across a range of *fixed* temperatures equally spaced in log-space (i.e. a *five*-parameter fit). Figure 2.5 shows that the basic *shape* of the emission measure distribution curves, which are typical for RS CVns, remains the same over the period of observation, but that the *magnitude* of the emission measure

distribution curves decreases smoothly with time. Simple cooling of the outburst plasma over the temperature range accessible to the PSPC would have shown the emission measure from matter at the hotter temperatures decreasing and emission measure at the cooler temperatures increasing with time, so the curves would show the emission measure distribution skewing to lower temperatures in this case. As the emission measures fall steadily over the whole temperature range with time without changing their relative contributions, this shows that the temperature remains more or less constant throughout the outburst, in agreement with the hardness ratio plot of Figure 2.2; substantial cooling of the plasma *on the timescale of days* can be rejected.

An approximate calculation of the thermal energy of a sampled plasma can be made using $\varepsilon = 3kT\,EM/n_e$, where ε is the thermal energy, k is the Boltzmann constant, n_e the electron density, T the temperature and EM the emission measure at that temperature. (This is only valid for constant electron densities.) Observations of Solar two-ribbon flares have suggested that for a given loop in a two-ribbon flare, the gas density is relatively independent of height – being about the same at the top of the loop and in the legs (Pneuman, 1982). Electron-density values for large two-ribbon flares (see section 2.4.1) in RS CVn systems typically lie between $10^{11}-10^{12}$ cm^{-3} (Jeffries and Bedford, 1990; Van den Oord et al. 1988). The spectral fit results of table 2.3, show that the largest value for the emission measure, of 1.5×10^{54}cm^{-3}, is in the first time bin at a temperature of 3×10^{7}K. These values and a value of $n_e = 10^{11}$cm^{-3} gives the thermal energy as 1.9×10^{35}ergs for this timebin.

For plasmas with $T > 10^6$K the *radiative* loss can be calculated from $Q = 10^{-19}T^{-1/2}$.EM (Hudson, Canfield & Kane 1978), giving a value of 2.7×10^{31} erg s^{-1}. Thus the radiative cooling time for this plasma, $\varepsilon/Q \sim 7000$ seconds. Similar results are obtained if these calculations are repeated for the

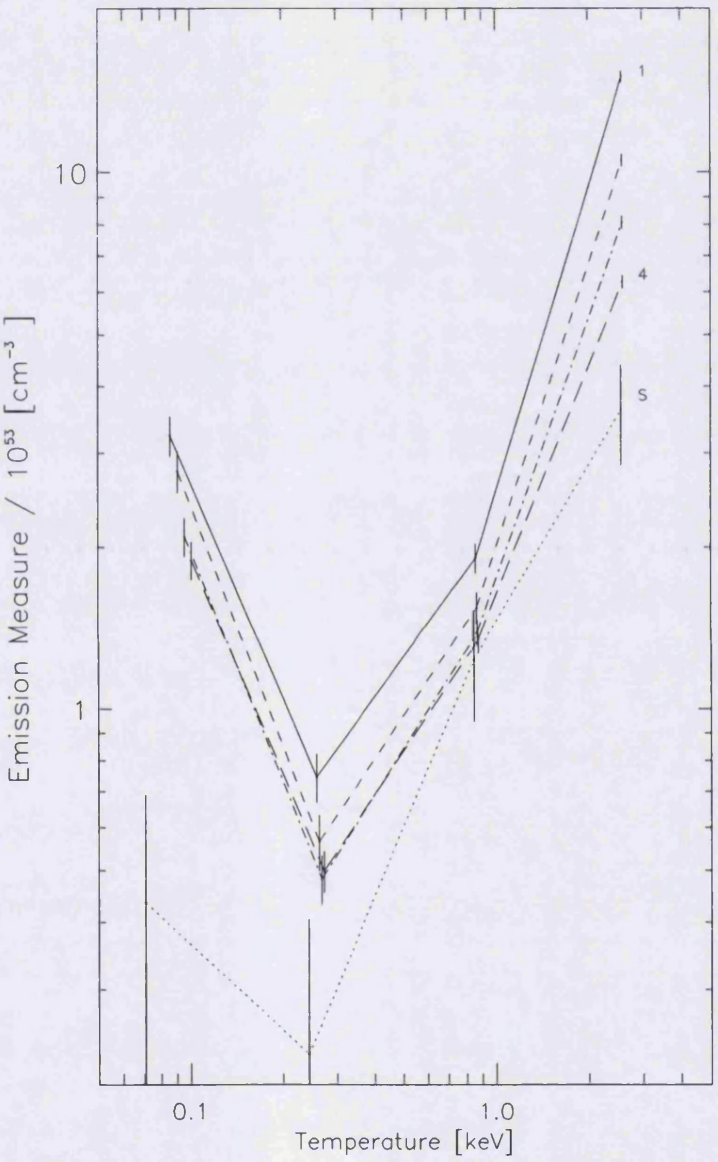

Figure 2.5: *A time varying emission measure distribution plot of the HR 5110 outburst. Note that the points have been slightly displaced in temperature for clarity. The emission measure distribution curves for the outburst are decreasing in magnitude with time from curve 1 – 4. Also shown is the corresponding survey emission measure distribution curve, denoted s.*

thermal plasma component of the Raymond & Smith and power-law model. As the emission is maintained over a period of $\sim$ 3 days, *some mechanism must be heating the plasma.*

One way in which chromospheric flares may be heated is from electrons with a power-law distribution in energy of the form $\frac{dn_e}{dE} = AE^{-\delta}$ (where A is some constant and δ is the power-law index) which have been accelerated down onto the chromosphere during the rise of the flare and fill the flare volume with hot ablated material (Brown 1971). This power-law distribution for the electron stream would give rise to a photon spectrum of the form $\Phi = A'(h\nu)^{-\gamma}$, (where A' is a constant, h is planck's constant, ν is the frequency of the emitted photon and γ is the power-law index such that $\gamma = \delta - 1$ in this case). From Hudson et al. (1978) the power generated via this 'thick target emission' is given by

$$P_{20} = 1.05 \times 10^{26} I_{20} \frac{b(\gamma)}{(\gamma - 1)} \text{ erg/s}$$

where $b(\gamma) = \gamma^2\ (\gamma\ -\ 1)^2\ B(\gamma - \frac{1}{2}, \frac{3}{2})$, P_{20} is the power deposited by electrons with energies $\gtrsim 20$ keV, and B(x,y) is the Beta function. A photon index of 1.87 is given for the first time bin in table 2.2, and this corresponds to a value of $b(\gamma)/(\gamma - 1) = 1.57$; $I_{20} = 20^{\gamma} I_1$ where I_1 is the normalisation of the power-law (K_0 in table 2.2). This gives a value of 1.50×10^{27} erg s^{-1} for the amount of power produced by the electrons. Clearly, this is insufficient to balance the energy loss previously calculated (2.7×10^{31} erg s^{-1}) indicating that chromospheric evaporation is unlikely to provide the energy input required to keep this plasma heated. If protons were being accelerated instead of electrons the energy generated would still be an order of magnitude too small. Another heating mechanism therefore must be sought.

2.4.1 A Two-Ribbon Flare?

Another possible heating mechanism is magnetic reconnection. This has been hypothesised to be the dominant energy producing process in Solar two-ribbon flares. These flares, so called because when observed in Hα two ribbons of emission are observed on either side of a dark ribbon or filament, decay over a period of several hours. The largest flare events observed on the Sun are of this type.

Kopp and Poletto (1984) have produced an analytical model describing the decay phase of a two-ribbon flare undergoing magnetic reconnection, and have successfully applied these models to a Solar flare observed with the SOLRAD satellite. The Kopp and Poletto (KP) reconnection model has also been successfully used to model a long duration ($\sim$ 1 day) flare observed on EQ Peg with EXOSAT, suggesting that EQ Peg had undergone the stellar equivalent of a Solar two-ribbon flare (Poletto, Pallavicini and Kopp 1988).

In the KP model, an unknown instability in the magnetic field causes an opening of the field line structure. As the magnetic field relaxes to a lower energy configuration, the magnetic field lines reconnect at increasingly higher altitudes, resulting in the rise of the neutral line as the flare progresses. Excess magnetic energy produced in this process is released as thermal energy, providing continuous heating of the plasma. The rate of release of this magnetic energy is given by

$$\frac{dE}{dt} = \frac{R_*^3 B_m^2}{8\pi} \frac{I_{12}(n)}{P_n^2(\theta)} \frac{2n(n+1)(2n+1)^2 y_1^{2n}[y_1^{2n+1}-1]}{[n+n(n+1)y_1^{2n+1}]^3} \frac{dy_1}{dt}$$

where R_*, B_m are the stellar radius and surface magnetic field respectively, $I_{12}(n)$ and $P_n^2(\theta)$ are related to the Legendre polynomials used to describe the magnetic field configuration, n is the order of the Legendre polynomial

(also defining the angular separation of the footpoints – larger for smaller values of n), and y_1 is the height of the reconnecting point (and hence the neutral line). From a number of observations of Solar two-ribbon flares, Kopp and Poletto were able to deduce that this motion can be described by an exponential function of the form

$$y_1(t) = 1 + (H_m/R_*)[1 - exp(-t/t_0)],$$

where H_m is the maximum height reached (equal to the separation of the footpoints), and t_0 is a time constant related to the duration of the event [see Kopp and Poletto (1984) for details].

An estimate for the total thermal energy released by HR 5110 in the outburst can be found by calculating the thermal energies for each of the time bins, and then summing the results. In the previous section, details were given of a crude calculation performed on the first time bin to give an order of magnitude value for this time bin. The total thermal energy released within each time bin can be calculated from ε = EM.Ψ(T).δt, where ε is the total (i.e. bolometric) thermal energy, EM is the emission measure, Ψ(T), the emissivity of an optically thin plasma at temperature T derived by Raymond (1979), and δt, the integration time of the time bin. The calculation reveals the magnitude of the outburst to have been $\gtrsim 4 \times 10^{36}$ ergs. On the basis of the duration of the event, it was inferred that HR 5110 had undergone the stellar equivalent of a two-ribbon flare.

Decay phase of the flare

The treatment of the decay phase of stellar flares by Van den Oord et al. (1988) introduced an improved means of determining parameters such as loop heights and volumes from observed quantities (see section 1.4.2). Their analysis models the flaring region as N identical semi-circular loops of length L. The emission

measure for these N loops can then be defined as

$$EM = \int n_e^2 dV = \frac{\pi}{8} n_e^2 L^3 (\Gamma + 1) N \alpha^2 \ cm^{-3} \tag{2.1}$$

with n_e, the electron density, Γ, an expansion factor for the loop and α, the ratio between the diameter of the loop at the base, and the loop length.

They defined an effective decay time for the flare as being the sum of the decay times resulting from both radiative and conductive losses within these flare loops. By substituting the definitions of the radiative and conductive cooling times, they were able to express the effective decay time in terms of observable parameters such as the count-rate and temperature decay times, i.e., if the radiative and conductive cooling times for a plasma, τ_r and τ_c respectively, are defined as,

$$\tau_r = \frac{3 n_0 k T_0}{n_0^2 \Psi_0 T_0^{-\gamma}} \tag{2.2}$$

and

$$\tau_c = \frac{3 n_0 k T_0 (\Gamma + 1) L^2}{8 \kappa_0 T_0^{7/2} f_l(\Gamma)} \tag{2.3}$$

with n_0,T_0 being the electron density and temperature of the plasma at the start of the decay phase, k is Boltzmanns constant, Ψ the plasma emissivity at that temperature, $f_l(\Gamma)$ is a function of the loop expansion factor and is dependent on the loop geometry. This gives:

$$\frac{1}{\tau_r} + \frac{1}{\tau_c} = \frac{1}{\tau_{eff}} = \frac{1}{2\tau_d} + \frac{(1 - \gamma/2)}{\tau_T} \tag{2.4}$$

with τ_d, τ_T being the count-rate and temperature decay times respectively.

Van den Oord et al. showed that using equations 2.1,2.2, and 2.3, and using the relationship $H\pi = L$ (where H is the loop height), equation 2.4 could be expressed in the form:

$$H^{3/2} - AH - B = 0 \tag{2.5}$$

with

$$A = \frac{\sqrt{8}}{3}\frac{\kappa_0}{k}\frac{f_l(\Gamma)}{(\Gamma+1)^{1/2}}\frac{T_0^{5/2}}{EM_0^{1/2}\tau_{\rm eff}N^{1/2}\alpha}$$

and

$$B = \frac{\sqrt{8}}{3}\frac{\Psi_0}{k}\frac{T_0^{-\gamma-1}}{\pi^2}\frac{EM_0^{1/2}}{(\Gamma+1)^{1/2}}\frac{\tau_{\rm eff}}{N^{1/2}\alpha}$$

(see Van den Oord et al., 1988, for a complete methodology and discussion).

Amendment to the Van den Oord treatment of the Decay phase

The observations presented in this chapter, have however demonstrated a continued heating during the decay phase of the flare. Thus in order to apply Van den Oord's methodology, some modification is required. This I have achieved through the addition of an extra heating term to equation 2.4 to give,

$$\frac{1}{\tau_{\rm eff}} = \frac{1}{\tau_{\rm r}} + \frac{1}{\tau_{\rm c}} - \frac{1}{\tau_{\rm H}} \tag{2.6}$$

with

$$\tau_{\rm H} = \frac{\varepsilon_{\rm H}}{3nkT}$$

and $\varepsilon_{\rm H}$ being the heating rate per unit volume.

In order to find the effective decay time for this analysis, I fitted the PSPC light curve with an exponential decay, giving $\tau_d \sim 6$ days. As the temperature remains virtually constant throughout the observation (See Figures 2.2,2.5 and discussion in section 2.4) $\tau_T \rightarrow \infty$. Therefore the $\tau_{\rm eff}$ can be approximated to $\tau_{\rm eff} = 2\tau_d$.

So, following the calculation of Van den Oord et al., substitution of equations 2.2, and 2.3 into equation 2.6 and rearranging, gives an expression for the cooling time of a plasma, which can be written

$$\frac{3nkT}{\tau_{\rm eff}} = n^2\Psi_0 T^{-\gamma} + \frac{8\kappa_0 T_0^{7/2} f_l(\Gamma)}{(\Gamma+1)H^2\pi^2} - \varepsilon_{\rm H} \tag{2.7}$$

Multiplying both sides of this equation by $\tau_{\rm eff}(\Gamma + 1)H^2\pi^2$, the equation becomes,

$$3nkT(\Gamma + 1)H^2\pi^2 = 8\kappa_0 T_0^{7/2} f_l(\Gamma)\tau_{\rm eff} - tau_{\rm eff}(\Gamma + 1)H^2\pi^2\varepsilon_{\rm H} + \tau_{\rm eff}(\Gamma + 1)H^2\pi^2 n^2 \Psi_0 T^{-\gamma} \tag{2.8}$$

Recall that equation 2.1 defines the emission measure as

$$EM = \int n_e^2 dV = \frac{\pi}{8} n_e^2 L^3(\Gamma + 1)N\alpha^2,$$

and this can be substituted in equation 2.8 to give,

$$3kT(\Gamma + 1)^{\frac{1}{2}} H^{\frac{1}{2}} \sqrt{8} \frac{EM^{\frac{1}{2}}}{(N\alpha^2)^{\frac{1}{2}}} = \frac{8EM\tau_{\rm eff}\Psi_0 T^{-\gamma}}{H^2\pi^2(N\alpha^{\frac{1}{2}})} + 8\kappa_0 T_0^{\frac{7}{2}} f_l(\Gamma)\tau_{\rm eff} - (\Gamma + 1)H^2\pi^2\varepsilon_{\rm H}\tau_{\rm eff} \tag{2.9}$$

Rearranging equation 2.9 gives,

$$3\sqrt{8}kT(\Gamma + 1)^{\frac{1}{2}} EM^{\frac{1}{2}} (N\alpha^2)^{\frac{1}{2}} \pi^2 H^{\frac{3}{2}} = (\Gamma + 1)\pi^4\varepsilon_{\rm H}\tau_{\rm eff}(N\alpha^2)H^3 + 8\kappa_0 T_0^{7/2} f_l(\Gamma)\tau_{\rm eff}(N\alpha^2)\pi^2 H - 8EM\tau_{\rm eff}\Psi_0 T^{-\gamma} \tag{2.10}$$

but $\pi^4(\Gamma + 1)(N\alpha^2)H^3 = 8V$, where V is the total volume of the loops. Substitution of V into the equation 2.10 and rearranging gives,

$$3kT(\Gamma + 1)^{\frac{1}{2}} EM^{\frac{1}{2}} (N\alpha^2)^{\frac{1}{2}} \pi^2 H^{\frac{3}{2}} - \sqrt{8}\kappa_0 T_0^{7/2} f_l(\Gamma)\tau_{\rm eff}(N\alpha^2)\pi^2 H - \sqrt{8}\tau_{\rm eff}(EM\Psi_0 T^{-\gamma} - \varepsilon_{\rm H} V) = 0 \tag{2.11}$$

By substitution of variables, this reduces to the form,

$$H^{\frac{3}{2}} - AH - B' = 0 \tag{2.12}$$

Note that this is a cubic equation in $H^{\frac{1}{2}}$ with,

$$A = \frac{\sqrt{8}}{3}\frac{\kappa_0}{k}\frac{f_l(\Gamma)}{(\Gamma+1)^{1/2}}\frac{T_0^{5/2}}{EM_0^{1/2}\tau_{\rm eff}N^{1/2}\alpha} \tag{2.13}$$

as before, and

$$B' = \frac{\sqrt{8}}{3}\frac{\Psi_0}{k}\frac{T_0^{-\gamma-1}}{\pi^2}\frac{EM_0^{1/2}}{(\Gamma+1)^{1/2}}\frac{\tau_{\rm eff}}{N^{1/2}\alpha}(1-\varepsilon_f) \tag{2.14}$$

where

$$\varepsilon_f = \frac{\varepsilon_{\rm H}V}{EM_0\Psi_0T^{-\gamma}} \tag{2.15}$$

i.e., B' can be defined as $B' = (1-\varepsilon_f)B$, which reduces to B as given by Van den Oord et al. when there is no heating present.

I solved equation 2.12 for $H^{1/2}$, and thus determined the height, H of a loop (H=L/π), as a function of the unknown parameter, Nα^2, for a given value of Γ and a given heating fraction f. Figure 2.6 shows that for a rigid loop structure ($\Gamma = 1$), $\tau_{\rm eff} = 2\tau_d$ and no heating present, the minimum height of the loop is $\sim 3 \times 10^{12}$ cm. Decreasing $(1-\varepsilon_f)$, i.e., increasing the amount of heating, or reducing the effective decay time by some factor reduces the minimum loop height by a similar amount. As $\tau_{\rm eff}$ is unlikely to be more than a factor of a few too high, loop heights corresponding to a compact loop (H<R_* $\sim$ $R_\odot$ say) require $>$ 99.9% of the radiative losses to be balanced by extra heating.

A further relationship between loop height, H, and Nα^2 was also derived by Van den Oord and Mewe (1989), under the condition that the loops cooled quasistatically. In this case, a necessary condition is that the ratio μ between the radiative and conductive cooling time remains constant, i.e.

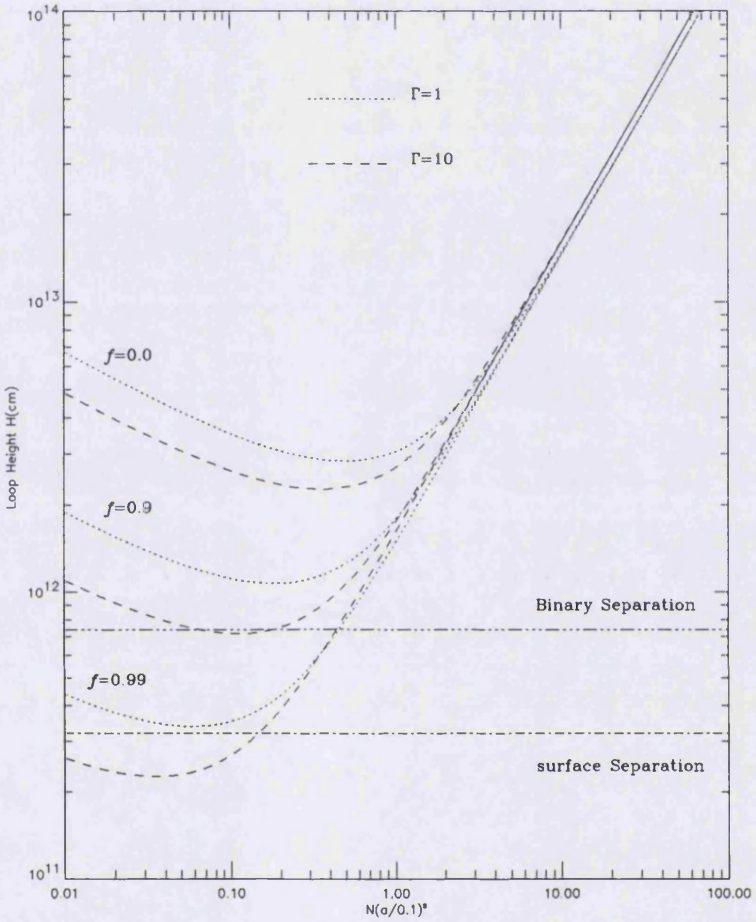

Figure 2.6: *This plot shows the height of a loop as a function of the unknown parameter, $N\alpha^2$, where N is the number of flaring loops and α is the aspect ratio of the loop. The two types of loop shown are those with Γ values of 1 (loop with constant cross section) indicated by dotted lines, and 10 (slightly expanding cross-section) indicated by dashed lines. Each of these pairs of loop are plotted with heating fractions of 0, 90%, and 99% of the radiative losses. The dash-dotted line represents the inter-binary separation of the system, as given in Strassmeier et al. (1993).*

$$\mu = \frac{\tau_r}{\tau_c} = 2.6 \times 10^{-3}(H_{10} N \alpha_{0.1}^2)\frac{T_7^{13/4}}{EM_{53}} = constant, \qquad (2.16)$$

where H_{10} is the loop height in units of 1×10^{10} cm, T_7 in units of 10^7 K and EM is in units of 10^{53} cm^{-3}. However, as the emission measures decreased throughout the observation, and the temperature remained virtually constant, it can be seen that quasistatic cooling is *not* taking place. This implies that the magnetic configuration of the outburst was in a non-equilibrium state, considerably reducing the probability that the flare event was compact in nature.

KP modelling

The combination of minimum loop heights derived in the previous section, combined with the large magnitude and long duration of the outburst, imply that it seems unlikely for the magnetic field configuration to have been spatially small ($H \ll R_*$). A small magnetic field configuration would also necessarily have given rise to very large field strengths [e.g. for $n = 9$, B $\sim 10^4$G which is approximately an order of magnitude greater than magnetic field strengths previously found on RS CVns (Donati et al. 1990) or even dMe flare stars (Saar et al. 1987). From this analysis, a large magnetic feld configuration is therefore preferred. Thus, this rules out Kopp and Poletto (KP) models with large values of n ($n \gtrsim 9$ is equivalent to small loops). This assumption is also supported by the cursory analysis of a very similar long-duration event ($\sim$ 9 day outburst) observed on the RS CVn CF Tucanæ, which has an inclination of $\sim 64°$ and yet shows no eclipse variation, suggesting a flaring volume larger than the primary (Kürster 1995; see also Chapter 4).

To proceed with modelling, I made the initial assumption that the footpoints (starspots) were restricted to equatorial bands as is the case for the Sun, and I chose a KP model with a value of $n = 3$, giving a loop footpoint

separation of $\sim 53°$ (I rejected $n = 1$ as the footpoints would be situated at opposite poles, and the flare would cover the whole stellar surface). I calculated the total energy for each time bin as before, using $Q = 10^{-19}T^{-1/2}.EM$ and the spectral fit parameters in Table 2.3. As the rise to peak was not observed, the only information available concerning the quiescent state of HR 5110 was taken from the survey observation six months before. To allow for the possibility that the flare began several days (or more) before the initial observation, I performed a number of fits as follows, (see Figure 2.7.):

Fit A: I placed the pre-flare (quiescent) measurement *immediately* before the first photon detected in the PSPC pointed observation and I then fitted the energy decay curve with a $n = 3$ KP model,

Fit B: I assumed a shift of one day earlier in the position of the quiescent data point, and again fitted the energy decay with a $n = 3$ KP model,

Fit C: a shift of four days earlier in the position of the quiescent data point, fitted with a $n = 3$ KP model, and

Fit D: I placed the quiescent data point immediately before the first photon detected in the PSPC pointed observation and fitted with an exponential decay model.

Given the model and assuming Gaussian errors (Jeffries 1961), the χ^2-values were used to derive the joint probability distribution for the four fit parameters (offsets and scales for both time and flux). This was achieved by integrating out (marginalising) the unwanted parameters, leaving probability distributions for just the useful parameters. These are: t_0, the start time of the flare, f_0, the quiescent flux level and $t_s \times f_s$, a parameter related to the energy released during the flare (with t_s, a time constant for the KP model, and f_s a luminosity scale).

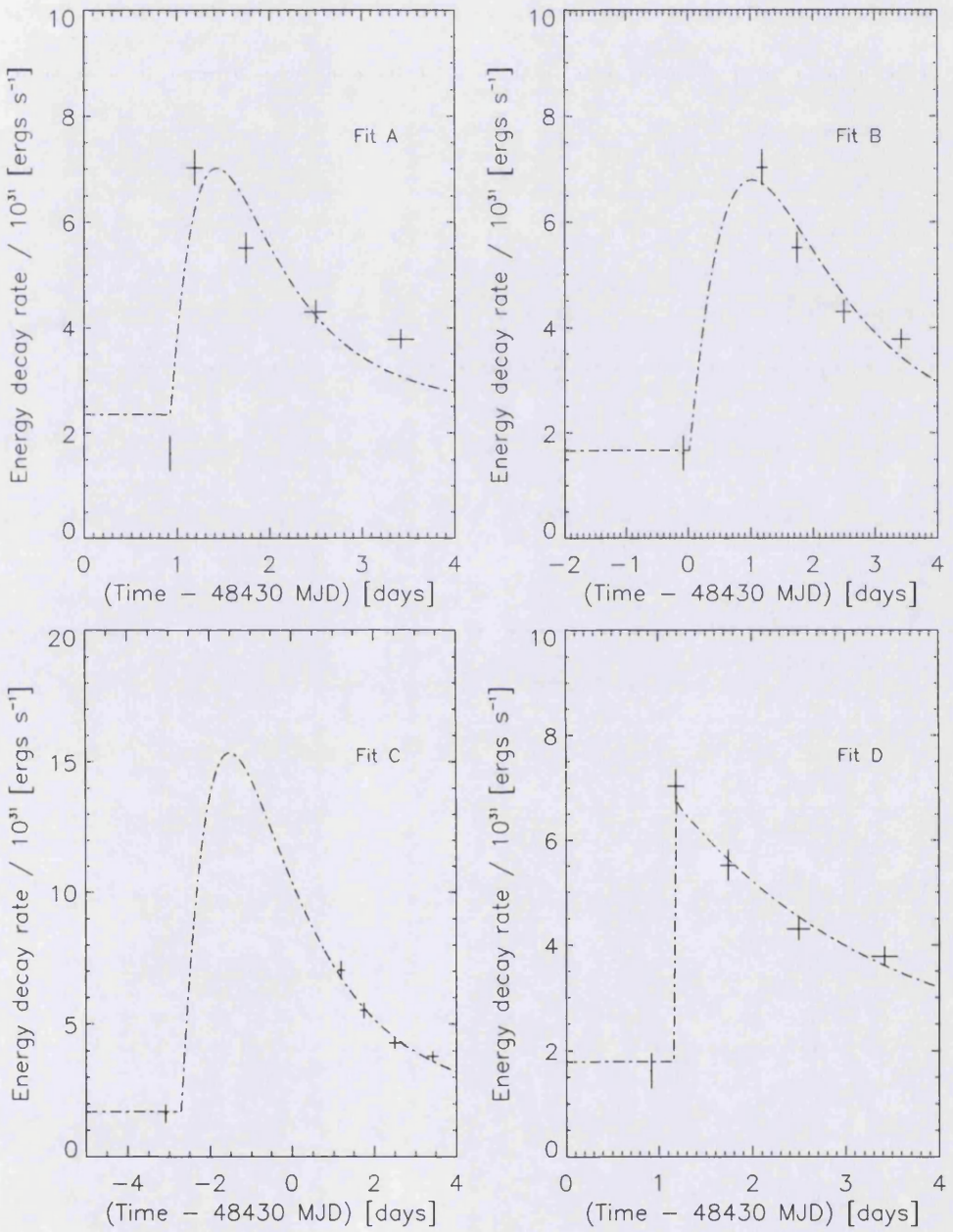

Figure 2.7: *Observed energy decay rate of the outburst is overplotted on various flare model fits. (a)–(c) Standard KP model flares (n=3) with the start of the flare taken as the start of the observation, one day before and four days before, respectively. (d) An exponential decay model with the start of the flare taken as the start of the observation. (See text for details.)*

Gaussian fits to these where possible give the best value and 1σ errors listed in Table 2.4.1. Where a Gaussian was deemed to be a poor representation, ranges or limits are given.

Fits to the standard Kopp and Poletto models were less than successful (see table 2.4.1). A minimum solution (fit A) is unable to accommodate the low background and the high curvature of the decay phase simultaneously. A shift of one day in the position of the background point increases the goodness-of-fit substantially (fit B, with χ^2_ν of 8.0 — a decrease from fit A's χ^2_ν of 45.5), but it is still not acceptable, again owing to the high curvature of the decay phase. Obviously, if this is continued (fit C), the fit will improve (in fact, $\chi^2_\nu = 2.9$) but the total energy of the flare will grow very rapidly as the data cluster down onto the tail of the decay where they will not usefully constrain the fit over a significantly large part of the flare's duration. [In this case, the derived value for the outburst energy $\gtrsim 10^{38}$ ergs, which equates to a few percent of the total magnetic energy available to the binary system as a whole (see below).] A similar effect could also be achieved by increasing n, as this increases the rise time of the flare without affecting the decay time. However, this also requires a decrease in the size of the flare loop, contrary to the assumption that the flare is not compact.

A better fit to the minimal-case data is achieved by using a pure exponential decay (fit D) generated by using the physical model of Kopp and Poletto to *predict* the functional form of y_1 needed to give rise to the *required* (in this case exponential) model. This is the inverse of the KP modelling (Kopp & Poletto 1984) where they assume a Solar-like function for y_1 and then calculate the expected flare behaviour (Wonnacott 1994). Even this fit, however, is still quite poor. The decrease in the χ^2_ν ($= 2.9$) is achieved by making the impulsive rise as sharp as possible (actually discontinuous in the exponential model). The

KP model cannot match this as the only way to make the model more peaked is to increase n substantially above 3 ($n = 5$ is insufficient).

The high signal-to-noise of the data resulting from the use of only four time bins, has enabled this deviation between observation and the standard KP model for a two-ribbon stellar flare to be reliably established; this is possibly the first time that serious departures from these models have been found for such a large outburst. This is, however, not unexpected: two effects are involved here. Firstly, previous data has been severely limited by Poisson noise and secondly, owing to the proximity of the two stars ($\sim$ 10.6 $R_\odot$, Strassmeier et al. 1988) the reconnection of the magnetic field lines is unlikely to be the simple affair described by the Kopp and Poletto model. Instead, one could speculate that some sort of interaction between the magnetic field configurations of both stars may be involved; any reconnection taking place may therefore be between the two component stars, resulting in an inter-binary flare. The minimum loop heights, inferred from the general treatment of the decay phase, lend support to this idea.

Van den Oord (1988) investigated the possibility of magnetic reconnection taking place in a binary system, and derived an analytical expression for the amount of energy stored within an (idealized) system:

$$W = 8 \times 10^{37} \left(\frac{L}{R_\odot}\right) \left(\frac{a}{R_\odot}\right)^2 \left(\frac{B}{1000G}\right)^2 \text{erg.}$$

where L is the length of the filament, a the binary separation, and B the surface magnetic field of both stars (assumed identical).

I calculated the magnetic fields for fits A – D using the two-ribbon model fit parameters in Table 2.4.1, under the assumption that the magnetic fields from the KP models are at least representative of the magnetic fields in the inter-

binary flare. The factor $t_s \times f_s$ in table 2.4.1 is related to the surface magnetic field by the expression $t_s \times f_s = R_*^3 B_m \Delta\phi$ where ϕ is the *longitudinal* extent of the flaring arcade. This is taken to be twice the *latitudinal* width of the region as is often the case for the Sun (Poletto et al. 1989), and is therefore a 'known' variable dependent on the value of n. From detailed studies of Solar flares, it has been found that X-ray emission probably contributes only about 10% of the total bolometric energy losses (Poletto et al. 1988; Canfield et al. 1980): prior to deriving the magnetic fields, I therefore multiplied the factor $t_s \times f_s$ by 10. I then used the magnetic field values to find the total system energy as defined by Van den Oord. Under the assumption that the length of the filament is of the order of the maximum height attained by the neutral point (L $\sim$ H), energies of the order of $\sim 10^{40}$ ergs are obtained. This is more than enough to balance the energy requirements of the observed outburst.

This is probably not the first time that an inter-binary flare has been observed on an RS CVn system. Simon, Linsky and Schiffer (1980) suggested an inter-binary flare on UX Ari to be the cause of an outburst observed using the IUE satellite. In their proposed scenario, as flares produced on both the component stars rotate onto the inner faces of the binary, the magnetic field lines interact causing the stars to become temporarily magnetically coupled. In the case of HR 5110, the two components are closer together than in UX Ari and are in a synchronous orbit. Any inter-binary reconnection would therefore last longer, as the relative rotation of the stars would not interfere in this reconnection process. If this scenario correctly interprets the observations presented in this chapter, it would be interesting to find out how frequent such outbursts occur. Obviously similar observations are required, and these form the subject matter of subsequent chapters.

2.5 SUMMARY

A giant outburst lasting > 3 days was observed on the RS CVn system HR 5110, in both the WFC and PSPC instruments on the ROSAT satellite. Analyses of these data produced the following main results:

1. Examination of the ratio between the radiative and conductive cooling times during the decay of the flare, suggested that quasi-static cooling was not taking place. This implies that the magnetic configuration of the flare was in a non-equilibrium state, thus negating the possibility that the flare could have been compact in nature.

2. The long duration and large magnitude of the outburst ($\gtrsim 4 \times 10^{36}$ ergs), therefore suggested a large two-ribbon flare as the cause of this outburst.

3. Evidence for continued heating during the decay phase of the flare was found.

4. Attempts at fitting standard Kopp and Poletto two-ribbon flare models to the data, however, were unsatisfactory. The high signal-to-noise of these data implies that the observed departure from standard two-ribbon flare models is unambiguous. *This is the first time* that such large discrepencies in the model have been clearly identified for a stellar flare.

5. Differences in the morphology of the HR 5110 outburst light curve may be indicative of a different magnetic field configuration, and this, combined with the derived loop heights (which are of the order of the binary separation), suggest that the outburst may be of an inter-binary nature.

6. Simple calculations determined the amount of magnetic energy stored within the HR 5110 system to be of the order of 10^{40} ergs — enough to

balance the energy requirements of the observed outburst.

7. Magnetic Field strengths were derived for HR 5110 which are consistent with field strengths previously found in RS CVns (Bastian, 1994; van den Oord, 1988; Schmitt 1994). However, these values should be considered lower limits as they are based on estimates of the decay time constant for the KP model. Unfortunately in the case of thesethis constant is uncertain, as the start of the outburst was not observed.

Table 2.2: *This table shows the results of fitting a combined Raymond and Smith plus powerlaw model to the uncorrected PSPC data.*

#	kT [keV]	EM [$10^{53}\,cm^{-3}$]	α	K_0 [a]	N_H [$10^{19}\,cm^{-2}$]	χ^2_ν
1	1.00 ± 0.03	3.53 ± 0.46	1.87 ± 0.03	$(1.33\pm0.06)\times10^{-2}$	5.20 ± 0.32	1.19
2	1.00 ± 0.04	2.74 ± 0.39	1.94 ± 0.04	$(9.34\pm0.48)\times10^{-3}$	5.54 ± 0.38	1.19
3	0.95 ± 0.04	2.08 ± 0.29	1.94 ± 0.03	$(7.50\pm0.35)\times10^{-3}$	5.08 ± 0.33	1.03
4	0.89 ± 0.01	1.70 ± 0.12	1.99 ± 0.03	$(6.20\pm0.18)\times10^{-3}$	5.33 ± 0.34	1.05
S	0.93 ± 0.21	1.80 ± 1.30	1.87 ± 0.33	$(2.94\pm1.65)\times10^{-3}$	2.40 ± 1.55	1.14

[a] In units of photons/cm^2/s/keV normalised at 1 keV.

Table 2.3: *This table shows the results of fitting a four-temperature Raymond and Smith model to the uncorrected PSPC data.*

#	EM_1 [a] [$10^{53}\,cm^{-3}$]	EM_2 [$10^{53}\,cm^{-3}$]	EM_3 [$10^{53}\,cm^{-3}$]	EM_4 [$10^{53}\,cm^{-3}$]	N_H [$10^{19}\,cm^{-2}$]	χ^2_ν
1	3.25 ± 0.30	0.75 ± 0.08	1.91 ± 0.14	15.06 ± 0.65	8.29 ± 0.60	1.26
2	2.78 ± 0.27	0.57 ± 0.07	1.54 ± 0.12	10.53 ± 0.49	8.96 ± 0.68	1.29
3	2.10 ± 0.19	0.48 ± 0.05	1.39 ± 0.09	8.92 ± 0.40	8.11 ± 0.59	1.21
4	1.90 ± 0.17	0.50 ± 0.05	1.35 ± 0.08	6.29 ± 1.75	8.21 ± 0.59	1.22
S	0.44 ± 0.26	0.23 ± 0.18	1.23 ± 0.29	3.61 ± 1.01	2.65 ± 2.11	0.96

[a] Emission measures 1–4 fitted with fixed temperatures $(1, 3, 10, 30)\times10^6$ K respectively.

Table 2.4: *A combined Raymond and Smith plus powerlaw model fitted to both the WFC and PSPC data (the PSPC data were multiplied by a factor of 1.77).*

#	kT [keV]	EM [$10^{53}\,cm^{-3}$]	α	K_0 [a]	N_H [$10^{19}\,cm^{-2}$]	χ^2_ν
1	1.03 ± 0.03	6.93 ± 0.77	1.96 ± 0.03	$(2.28\pm0.10)\times10^{-2}$	6.47 ± 0.25	1.35
2	1.00 ± 0.04	4.92 ± 0.67	1.96 ± 0.03	$(1.64\pm0.08)\times10^{-2}$	5.75 ± 0.28	1.23
3	0.93 ± 0.05	3.42 ± 0.47	1.91 ± 0.03	$(1.36\pm0.06)\times10^{-2}$	4.85 ± 0.24	1.04
4	0.89 ± 0.01	2.98 ± 0.17	1.96 ± 0.02	$(1.09\pm0.03)\times10^{-2}$	4.79 ± 0.25	1.08
S	1.006 ± 0.061	4.29 ± 0.84	2.93 ± 0.51	$(1.3\pm1.0)\times10^{-3}$	5.68 ± 0.53	0.93

[a] In units of photons/cm^2/s/keV normalised at 1 keV.

Table 2.5: *The combined WFC and PSPC data fitted with a four-temprature Raymond and Smith plasma model (the PSPC data were multiplied by a factor of 1.77).*

#	EM_1 [a] [$10^{53}\,cm^{-3}$]	EM_2 [$10^{53}\,cm^{-3}$]	EM_3 [$10^{53}\,cm^{-3}$]	EM_4 [$10^{53}\,cm^{-3}$]	N_H [$10^{19}\,cm^{-2}$]	χ^2_ν
1	5.4 ± 3.4	1.35 ± 0.14	3.38 ± 0.20	26.50 ± 0.57	7.83 ± 0.40	1.26
2	3.65 ± 0.27	1.07 ± 0.12	2.63 ± 0.18	18.66 ± 0.50	6.77 ± 0.42	1.44
3	2.65 ± 0.18	0.894 ± 0.087	2.30 ± 0.13	14.64 ± 0.34	5.82 ± 0.38	1.37
4	2.30 ± 0.15	0.938 ± 0.074	2.27 ± 0.11	11.26 ± 0.30	5.57 ± 0.39	1.48
S	1.37 ± 0.15	0.04 ± 0.26	2.41 ± 0.44	3.9 ± 1.1	4.12 ± 0.21	0.93

[a] Emission measures 1–4 fitted with fixed temperatures $(1, 3, 10, 30) \times 10^6$ K respectively.

Model	t_0 [a] (d)	f_0 (10^{31} erg/s)	$t_s \times f_s$ (10^{39} erg)	χ^2_ν	E_{BOL} (10^{36} erg)	B_m (G)
A	0.89 – 0.91	2.29 ± 0.19	3.58 ± 0.40	45.5	6.03 ± 0.68	500 ± 28
B	-0.11 – 0.09	1.74 ± 0.20	7.22 ± 0.72	8.0	12.2 ± 1.2	710 ± 35
C	-2.9 – -2.5	1.65 ± 0.17	21.5 ± 6.4	2.9	36 ± 11	1200 ± 180
D	< 1.18	1.68 ± 0.34	4.25 ± 0.80	2.9	7.2 ± 1.4	540 ± 52

[a]Note that the start time, t_0, follows a *Top-Hat* distribution rather than a gaussian one and so is expressed as a range of values.

Table 2.6: *Fitted flare model parameters for HR 5110.* t_0 *refers to the start time of the flare and is measured in days from 48430 MJD.* f_0 *is the quiescent flux level produced by the model.*

Chapter 3

HR 5110—You Can't Keep A Good Flare Down

... All that's bright must fade...

Thomas Moore (1779 – 1852)

3.1 INTRODUCTION

In chapter 2 I presented observations of a long-duration flare event in the RS CVn system HR 5110. Although, unfortunately, the start of the flare was missed, the analyses indicated that this flare may have been of an inter-binary nature. Further similar observations would therefore be required in order to produce a more complete picture of these outbursts as well as providing an

indication of the frequency with which they occur. In this chapter I describe one such similar observation.

3.2 THE DATA

A *follow-up* pointed observation of the Lockman hole region in which HR 5110 is situated, was made with the ROSAT satellite on 19th June 1993 using both the WFC and PSPC instruments, two years after the observation described in chapter 2. The 33 ks observation was spread over $\sim$ 28 days, and *again* found HR 5110 to be undergoing long-duration flaring activity.

3.3 THE ANALYSIS

3.3.1 The Time-Series.

I extracted the pointed PSPC (0.1–2.4 keV) and WFC (62–185 eV) time series as in chapter 2, and these can be seen together in Fig. 3.1. They reveal that HR 5110 was displaying *substantial* activity over the 28-day period of observation, with a number of very large flaring events being observed. The WFC EUV observation shows much more variation than in the previous observation, and the EUV countrate can be seen to follow the variation of the soft X-rays detected with the PSPC. Note that in the PSPC lightcurve, even the smallest count rates obtained during this observation are a factor $\sim$2 larger than the quiescent survey value of 2.28$\pm$0.22 ct/s, cited in chapter 2. It is therefore safe to assume that HR 5110 was already in a state of elevated activity when the observations began and probably continued in an active state after the end of the observation.

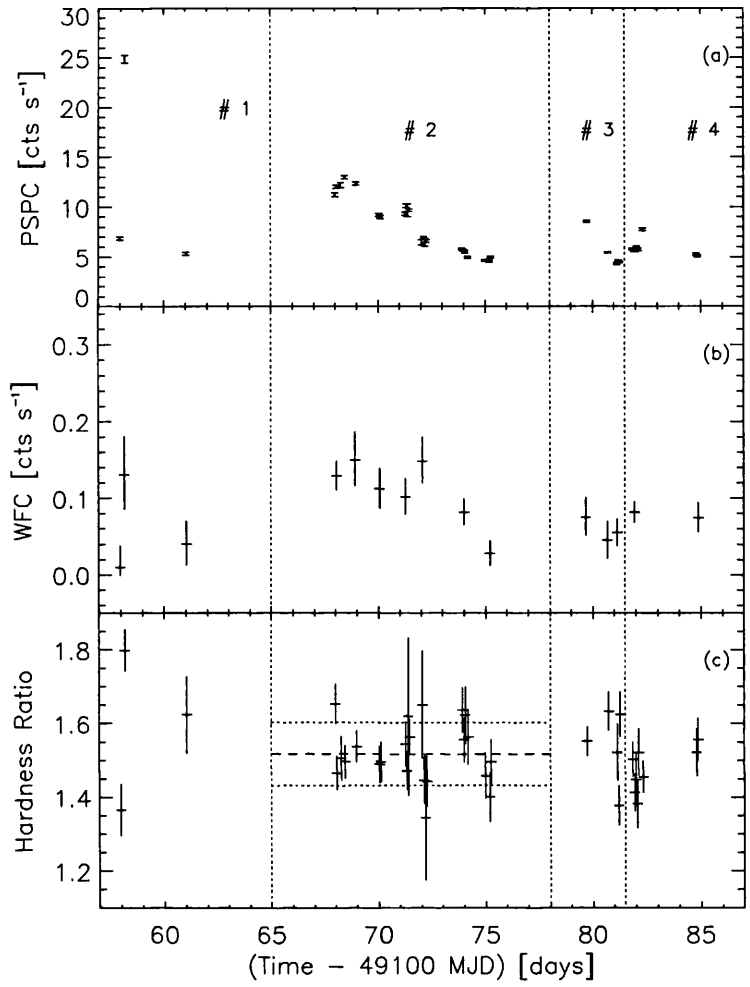

Figure 3.1: *The ROSAT PSPC (a) and WFC (b) lightcurves of HR 5110 reveal a number of very large flare events which occured in this system over a period of ∼ a month. For reference purposes these flares have been numbered in order. The WFC EUV countrate is seen to follow that of the PSPC. (c) The hardness ratio seems to indicate a different behaviour in the temperature decay between the first flare (which experiences an impulsive rise and then decay) and the much longer-duration second flare which remains fairly constant during the outburst (to within the 1σ errors - represented by the dotted lines).*

Spectrum N°.	Start Time [MJD]	End Time [MJD]	Integration Time [ks]
1	49157.934	49158.068	1.253
2	49158.068	49158.268	0.564
3	49160.938	49161.138	0.676
4	49167.879	49168.012	0.962
5a	49168.012	49168.146	1.017
5b	49168.212	49168.346	0.517
5c	49168.413	49168.546	0.793
5d	49168.947	49169.080	1.109
6	49169.948	49170.215	1.926
7	49171.149	49171.549	2.447
8	49171.950	49172.350	1.647
9	49173.818	49174.286	4.092
10	49174.886	49175.353	3.136
11a	49179.625	49180.092	1.197
11b	49180.092	49180.826	2.194
12	49181.026	49181.360	3.607
13a	49181.760	49182.228	5.379
13b	49182.228	49182.428	1.366
14	49184.697	49184.963	3.140

Table 3.1: *Table detailing the time bins within which the spectra were extracted.*

Figure 3.1 shows the that the count-rate for the initial very large flare (denoted #1 in the figure) rises from 6.87±0.17 ct/s to 24.91±0.38 ct/s over a period of $\sim$ 4.8 hours and then falls again to 5.34±0.17 ct/s over a period $\lesssim$ 2.9 days. Although the large magnitude of the peak count-rate is striking, any determination and/or supposition concerning the nature of this flare is limited due to the large data gaps present. The long decay time of the first flare can therefore considered to be an upper limit. However, the light curve exhibited for the second outburst is more complete, although it demonstrates a morphology different from that of light curves typical of stellar two-ribbon flares (e.g. Ottmann & Schmitt, 1994; Pallavicini et al. 1990). Although not as peaked as the first flare, it is of much longer duration, and decays from a

count rate of 12.99±0.19 ct/s to 4.96±0.10 ct/s over a period of $\sim$ 7.5 days. By way of comparison, the outburst reported in chapter 2 was seen to decay from 11.30±0.12 ct/s to 5.11±0.08 ct/s over a period $\sim$ 3 days. Following the second outburst, there are two further smaller flares; the remnants of the first are seen in the decay stage (its initial rise is missing due to data gaps) and the final flare is seen to decay from 7.74±0.11 ct/s to 5.05±0.09 ct/s over a period $\lesssim$ 2.5 days, the uncertainty being due to data gaps.

Spectrum N°.	kT [keV]	EM [10^{53} cm^{-3}]	α	K_0[a]	N_H [10^{19} cm^{-2}]	χ^2_ν	(dof)
1	1.05±0.08	2.04±0.78	1.90±0.12	(7.70±1.22)×10^{-3}	3.54±1.06	1.01	(89)
2	1.11±0.08	5.24±2.35	1.51±0.06	(4.06±0.35)×10^{-2}	2.87±0.81	0.97	(132)
3	0.90±0.06	1.63±0.45	2.34±0.20	(4.93±0.96)×10^{-3}	8.90±2.46	1.03	(57)
4	0.98±0.21	1.59±1.20	1.73±0.82	(1.80±0.19)×10^{-2}	4.52±1.05	1.00	(110)
5a	0.88±0.06	1.50±0.46	1.79±0.07	(1.78±0.11)×10^{-2}	3.86±0.91	0.77	(42)
5b	1.26±0.19	7.09±3.32	2.16±0.26	(1.13±0.40)×10^{-2}	7.08±1.89	1.18	(21)
5c	1.10±0.05	4.64±1.34	2.07±0.12	(1.52±0.22)×10^{-2}	6.98±1.29	1.03	(38)
5d	0.98±0.09	3.28±1.10	2.05±0.10	(1.46±0.18)×10^{-2}	6.79±1.08	1.17	(47)
6	0.89±0.27	2.13±0.31	2.03±0.70	(1.00±0.07)×10^{-2}	5.24±0.85	1.15	(130)
7	0.93±0.10	2.17±0.66	1.95±0.07	(1.20±0.10)×10^{-2}	5.16±0.72	0.87	(145)
8	0.89±0.03	1.91±0.28	2.06±0.10	(5.93±0.63)×10^{-3}	3.75±0.92	1.09	(106)
9	0.88±0.02	1.40±0.16	1.99±0.06	(6.01±0.37)×10^{-3}	5.08±0.75	1.10	(141)
10	0.90±0.03	1.04±0.18	1.91±0.07	(5.56±0.40)×10^{-3}	4.02±0.82	0.96	(128)
11a	0.86±0.03	1.71±0.29	1.77±0.06	(1.08±0.07)×10^{-2}	3.06±0.73	1.15	(134)
11b	0.83±0.05	0.99±0.21	1.95±0.08	(6.51±0.05)×10^{-3}	5.56±0.11	1.01	(113)
12	0.86±0.03	0.92±0.15	1.99±0.07	(5.06±0.35)×10^{-3}	5.01±0.88	1.17	(129)
13a	0.89±0.02	1.29±0.14	1.89±0.05	(6.47±0.33)×10^{-3}	3.40±0.54	1.51	(148)
13b	1.02±0.10	1.97±0.79	1.87±0.10	(9.47±1.21)×10^{-3}	3.95±0.98	0.89	(108)
14	0.97±0.07	1.67±0.42	2.09±0.11	(4.96±0.66)×10^{-3}	5.62±0.94	1.12	(130)

[a] In units of photons/cm^2/s/keV normalised at 1 keV.

Table 3.2: *This table shows the results of fitting a Raymond and Smith plus power-law model to the PSPC data.*

Also shown in Fig. 3.1 is the hardness ratio obtained for the observation. As mentioned in the previous chapter, this can be used as an approximate indi-

cator of temperature and reveals the temporal variation in temperature during the outbursts. The hardness ratio was defined (as in chapter 2) as the hard band counts (0.29 – 2.00 keV) divided by the soft band counts (0.1 – 0.28 keV). In the second outburst, although an impulsive phase is observed, the relatively small temperature rise is short-lived, and the temperature then remains essentially constant (to within the errors) for the duration of the event. In contrast, the first flare demonstrates a relatively larger and rapid rise in temperature during the impulsive phase followed by a decay. Thus a distinct difference between the temperature variations seen in the first flare and the second long-duration outburst can clearly be seen, and suggests possibly different physical processes occuring within these flare events. The temporal variation of the temperatures of the two final flares, however, is much more poorly constrained due to the data gaps.

3.3.2 The Spectral Analysis

In order to investigate the spectral evolution with time during this observation, I split the time series into 19 time-bins, and within each I extracted a spectrum. The times delimiting these spectra are given in table 3.1. The spectra were then background subtracted, exposure corrected and corrected for vignetting effects as in chapter 2, and converted into a format which could be used by the XSPEC spectral fitting package. The consistently best fits obtained for all the spectra used (as found in chapter 2) were either a combined Raymond and Smith plasma and power-law model with interstellar column and all parameters left free (i.e. *five* d.o.f.— See table 3.3.1) or a four-temperature Raymond and Smith optically thin plasma model, with the four temperatures *fixed* as before at 10^6, 3×10^6, 10^7, and 3×10^7K — (See tables 3.3.2). Again this corresponds to *five* degrees of freedom.

Spectrum N°	EM_1 [a] $[10^{53}\,cm^{-3}]$	EM_2 $[10^{53}\,cm^{-3}]$	EM_3 $[10^{53}\,cm^{-3}]$	EM_4 $[10^{53}\,cm^{-3}]$	N_H $[10^{19}\,cm^{-2}]$	χ^2_ν	(dof)
1	1.97±0.56	0.43±0.15	0.79±0.22	0.82±0.69	7.2±2.0	1.07	(89)
2	3.12±1.48	0.82±0.42	0.78±0.63	43.89±21.49	5.5±2.1	1.01	(132)
3	3.62±1.32	0.48±0.20	1.29±0.28	4.12±0.80	14.7±3.7	1.08	(57)
4	3.85±1.13	0.83±0.23	0.66±0.33	16.78±1.24	9.9±2.2	1.09	(110)
5a	4.04±0.98	0.98±0.23	0.98±0.33	15.83±1.21	8.74±1.78	0.92	(42)
5b	6.63±2.08	0.43±0.34	1.32±0.49	17.07±1.65	1.32±0.29	1.56	(21)
5c	8.26±1.91	0.64±0.28	1.71±0.42	16.50±1.41	14.4±2.3	1.30	(38)
5d	7.91±1.55	0.72±0.24	2.20±0.35	13.27±1.13	14.4±1.9	1.24	(47)
6	4.12±0.73	0.65±0.15	1.72±0.22	8.64±0.71	10.8±1.5	1.3	(130)
7	3.79±0.63	0.80±0.14	1.38±0.20	10.99±0.72	9.9±1..3	1.01	(145)
8	1.93±0.44	0.51±0.13	1.44±0.19	5.43±0.59	6.8±1.6	1.15	(106)
9	1.61±0.31	0.59±0.08	1.01±0.12	5.43±0.39	8.1±1.3	1.15	(141)
10	1.61±0.33	0.32±0.08	0.79±0.12	4.99±0.41	8.5±1.5	1.01	(128)
11a	2.25±0.49	0.52±0.14	1.51±0.21	9.45±0.73	7.3±1.5	1.25	(134)
11b	2.01±0.51	0.60±0.11	0.89±0.16	5.29±0.51	10.3±2.0	1.12	(113)
12	1.80±0.35	0.42±0.01	0.80±0.11	4.19±0.36	10.1±1.6	1.25	(129)
13a	1.67±0.51	0.40±0.07	1.00±0.10	5.80±0.37	7.3±1.0	1.7	(148)
13b	1.94±0.56	0.66±0.16	0.74±0.22	9.72±0.79	6.8±1.8	0.90	(108)
14	2.06±0.40	0.38±0.09	1.01±0.02	4.89±0.41	10.2±1.6	1.17	(130)

[a] Emission measures 1–4 fitted with fixed temperatures $(1, 3, 10, 30) \times 10^6$ K respectively.

Table 3.3: *This table shows the results of fitting a four-temperature Raymond and Smith model to the PSPC data.*

3.3.3 Emission Measure Distribution Variations

In contrast to the initial, almost uninterrupted, three day observations of a large outburst presented in chapter 2, these observations show the physical state of HR 5110 before, during and after such an event. This of course is assuming that the second flare i.e. the long duration event, is a similar event to that in chapter 2. Also comparisons can be made between the several flare events which were observed.

The spectral parameters obtained using the four-temperature thermal plasma

model were used to plot emission measure distribution curves for the observation. To enable a much closer examination of the individual flare events, I split up the PSPC light curve into separate flare events and obtained an emission measure distribution plot for each one. These are shown in Figures 3.2–3.4 with the corresponding PSPC light curves plotted alongside. (The numbers correspond to the spectra numbers given in table 3.1.)

It can be seen from Fig. 3.1, that during the first flare there is a noticeable increase in temperature (as judged by the variation in hardness ratio) during the impulsive rise of the flare, as expected, followed by a decay. This is also demonstrated in Fig. 3.2, which shows that the largest variation in the emission measure is provided by the hottest component (at 3×10^7 K), indicating the large amount of material undergoing heating during the rise phase of this flare. Unlike the flare observed in chapter 2, the decay of this flare clearly shows skewing of material to lower temperatures, as the heated plasma cools.

The second outburst however, behaves differently. Although the rise of the second outburst was not observed, Fig. 3.1 shows that a smaller increase in hardness ratio (e.g. temperature) has occured. During the remainder of this second outburst, the hardness ratio variations remain constrained to within $1\,\sigma$ of their weighted mean and may be considered constant to within the errors. Thus by analogy to the outburst described in chapter 2, one might assume that continuous heating is occurring. Examination of the emission measure distribution for the second outburst corroborates this.

If one neglects the slight increases in the emission measure due to the rise in the PSPC count rate on day MJD 49171 (spectrum n^{o}·7), the emission measure distribution shows an essentially steady fall in the magnitude of the emission measure at all temperatures. Little skewing of the emission measure distribution is evident (which would have been indicative of cooling), but instead

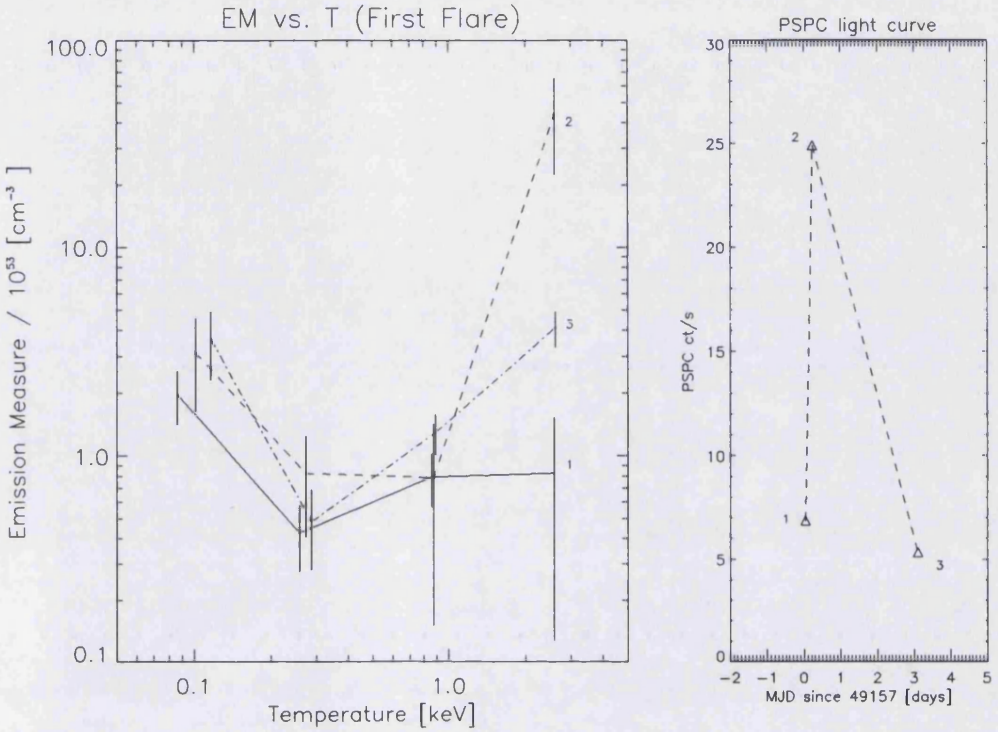

Figure 3.2: *A time resolved emission measure distribution plot for the first flare. Note that the points have been slightly displaced in temperature for clarity.*

substantial heating must have been taking place to maintain the temperatures observed.

3.3.4 Analyses of the Observed Flares

The analyses methods described and developed in chapter 2 are, where possible, now applied to the flare events described in this chapter. In this way a comparison between these flare events and that of chapter 2 can be made.

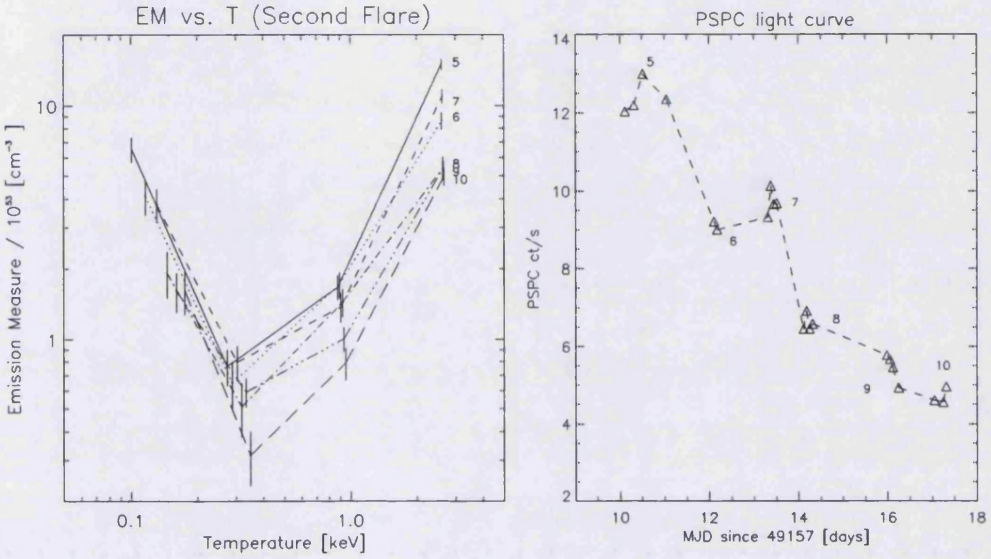

Figure 3.3: *A time resolved emission measure distribution plot for the second flare. Note that the points have been slightly displaced in temperature for clarity.*

The First Flare

For the first flare, the coverage provided only three spectra (N°. 1–3 in table 3.3.2), i.e. before the flare, peak of the flare and post-flare. This was due to the large data gaps present in the data. The data gaps between the peak of the flare and the post-flare point make it quite difficult to state with any certainty whether this last decay point is actually part of this flare decay, part of some post flare coronal enhancement, or even part of another flare. I therefore did not fit a flare model to this flare. Instead, I obtained upper and

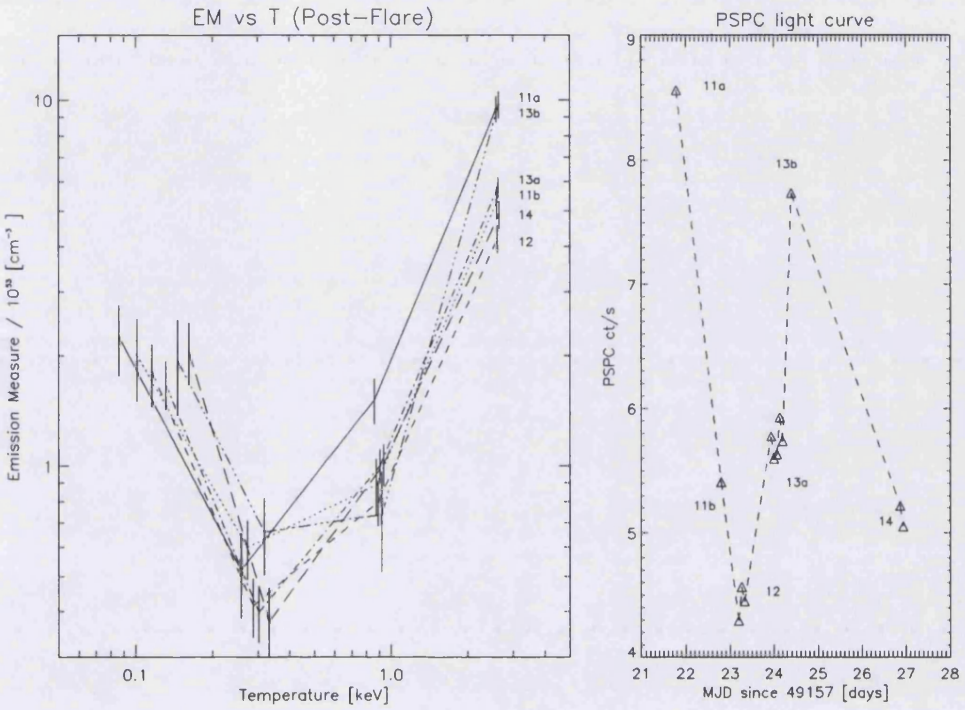

Figure 3.4: *A time resolved emission measure distribution plot for the final two flares. Note that the points have been slightly displaced in temperature for clarity.*

lower limits for the total derived thermal energy output.

I used the parameters derived from the four-temperature Raymond & Smith spectral models to do this. For each of the four temperature plasmas, I calculated an energy loss rate by multiplying the emission measure at that temperature by the radiative loss function given in table 3.4 (from Raymond 1979). Summing the four energy loss rates provided the total energy decay rate for each spectral time bin. To find the *upper* limit I integrated the area under a "join-the-dots" of the energy decay rate curve over the observed time of this

Table 3.4: *Radiated Power function (erg cm^3 s^{-1}) as a function of temperature (from Raymond 1979)*

T [K]	Log_{10} T	$10^{23}P_{rad}$
1×10^6	6.0	11.6
3×10^6	6.5	8.76
1×10^7	7.0	4.13
3×10^7	7.5	1.84

first flare. I obtained a *lower* limit by simply multiplying the energy decay rates (derived from the emission measures for each spectrum) by the corresponding integration time for each point. In this way I constrained the thermal energy output of this flare to lie between 1×10^{35} and 2×10^{37} ergs. This is comparable to typical values of very large stellar two-ribbon flares previously observed in RS CVns e.g. AR Lac has also been observed to undergo a large flare which produced a total energy output of 1×10^{37} erg (Ottmann & Schmitt 1994). A flare on Algol (although not an RS CVn, this system also exhibits RS CVn phenomenology) produced a total output energy of 10^{35} ergs (White et al., 1986; Van den Oord et al., 1989). See also Tables 1.1—1.2 in chapter 1.

The Second Flare

The coverage of the second flare was much better than that of the first, with 10 spectra extracted (N°. 4—10 in table 3.3.2). From these spectra, the thermal energy decay rates could be calculated as described above. Attempts at fitting a variety of Kopp and Poletto flare models to these decay rates were then made (using $n = 3-17$). These yielded very poor fits to the data, with a best fit χ^2_ν of 25.4 (with 4 d.o.f) for a KP model of $n = 3$. As can be seen from Fig 3.5, the KP model would give a fairly good (by eye) fit to the data, except that on day MJD 49171 the PSPC count rate rises again (as does the

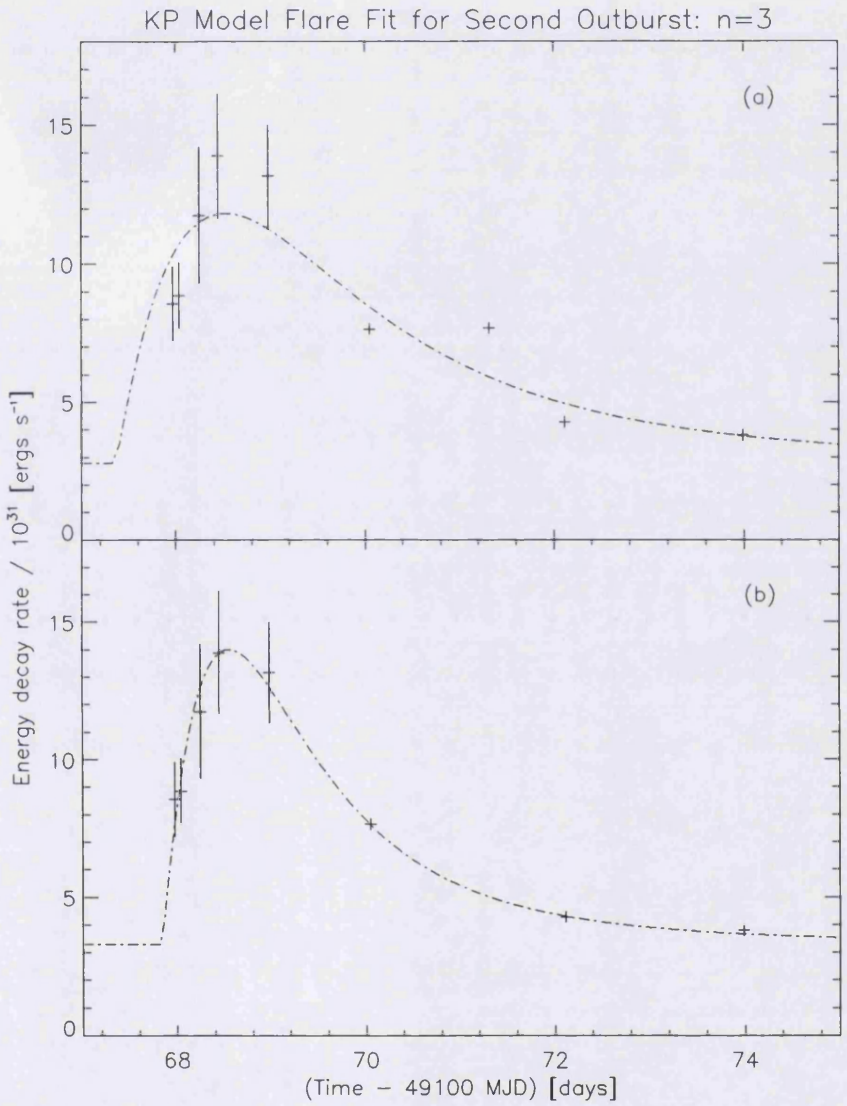

Figure 3.5: *Best fit n=3 KP model for the second flare. (a) This uses all the derived energy decay data points. Note that the second peak in the data is the main cause of the poor fit.* ($\chi^2_\nu = 25.4$) *(b) The second peak has been excluded and the fit greatly improved* ($\chi^2_\nu = 0.7$).

energy decay rate) which results in the very poor fit.

This second peak may possibly be due to sympathetic flaring occurring elsewhere in the system. The observed lightcurve would therefore be the result of superposition of count rates from separate events. However, limited by resolution, such a distinction cannot be made, and the possibility that the second peak may be part of the original outburst cannot be ruled out.

In order to see how well the KP model would fit without this 'extra' peak, I removed it from the energy decay data and again attempted to fit KP models, for n values of 3,9 and 17. The fits obtained were greatly improved, with typical $\chi^2_\nu \sim 0.7$ for *all* the values of n (see table 3.5). Thus it would be impossible to distinguish between orders of n purely on statistical grounds. Note however, that this inability to distinguish between orders of n, is a common occurrance when attempting to fit the KP model to flare data (e.g. Poletto et al. 1988).

Table 3.5: *Flare parameters for the long duration event.*

n	3	9	17
latitudinal width (degrees)	53°	20°	10°
% of stellar surface	20%	3%	1%
$t_s \times f_s$ (10^{40} erg)	1.12 ± 0.06	5.68 ± 0.29	16.90 ± 1.28
t_0 (days)	0.79 ± 0.09	0.74 ± 0.09	0.96 ± 0.11
f_0 (10^{31} erg/s)	3.25 ± 0.10	3.31 ± 0.11	3.33 ± 0.10
χ^2_ν	0.63	0.75	0.78
E_{Bol} (10^{37} erg)	1.89 ± 0.10	1.84 ± 0.09	1.80 ± 0.14
B_m (Gauss)	880 ± 23	3310 ± 85	7750 ± 295
H_m (10^{10} cm)	18.37	6.58	3.57
V_i (km/s)	26.9	10.3	4.3
n_e (10^{10}cm^{-3})	1.2–0.7	5.7–3.44	14.4–8.5

The KP model-fitting procedure (described in chapter 2), derives probability distributions for four fit-parameters. These are: t_0, the start time of the

flare, f_0, the quiescent flux level and $t_s \times f_s$, a parameter related to the energy released during the flare (with t_s, a time constant for the KP model, and f_s a luminosity scaling factor). The scaling of the energy decay rate curve (parameter $t_s \times f_s$), normalised to the area of the KP model (for a particular value of n), gives a value for the outburst energy. I thus obtained outburst energy values of 1.80–1.89$\times$ 10^{37} erg for n values of 17–3 respectively, and these results are tabulated in table 3.5.

For n values of 3–17, the derived magnetic field strength values ranged between 0.9 and 7.8 kG respectively. The field strength for the $n = 17$ case, is approaching an order of magnitude greater than typically found in RS CVn systems (Donati et al., 1990; Bastian, 1994). However, the lower n values (3–9) are more consistent with these typical values and with the magnetic field strength cited in chapter 2 of 0.5 kG (which was a lower limit).

Also given in table 3.5, are various other physical and geometric parameters for the X-ray emitting region, derived from the flare model fits. V_i is the initial upward velocity of the reconnecting point, defined as $V_i = H_m/t_0$, where H_m is the maximum height reached (equal to the separation of the footpoints in the KP model). Velocities derived for HR 5110 are found to be similar in magnitude to those derived for EQ Peg, Proxima Centauri and the Sun (Poletto et al. 1988; Kopp & Pneuman, 1976).

The electron densities, n_e, were calculated using the sum of the four-temperature emission measures, (for spectra 5–10 in table 3.3.2) and assuming a semicylindrical volume for the flaring loop arcade. Note that the derived electron density values for $n \lesssim 9$ are at the lower end of the range of values typical of two-ribbon flares in RS CVns (Jeffries & Bedford, 1990; Van den Oord et al., 1988).

The Third and Fourth Flares

An examination of the emission measure distribution for the third and fourth flares show a similar decay to the second outburst with the shape of the curves remaining essentially the same. As in the case of the first flare, the small number of data points ruled against a KP model fit. Instead decay times were estimated to derive various flare parameters (see below in Section 3.3.5).

3.3.5 General Decay Phase of the flares

In chapter 2, I introduced the methodology of Van den Oord et al.(1988) to derive flare loop parameters from observed quantities such as the count-rate and temperature *e*-folding times of the flare, and emission measures at the start of the flare decay. I then extended this method to account for the possibility of further heating during the decay phase of the flare. This extended methodology is now applied to the flare observations presented in this chapter. The required observable quantities were obtained as follows:

A plot of the natural logarithm of the flare count-rates versus time is shown in Figure 3.6. From this plot, I performed a least squares fit to provide count-rate decay times, τ_d, of $\lesssim 161$ and 613 ks for the first and second outbursts respectively. Note that the decay time for the first flare is poorly constrained (as are those for the final two flares) due to the large data gaps. Thus the effective decay time and derived loop height for this flare, should be considered an upper limit.

The temperature decay times for the flares could not explicitly be measured, because the spectra had been fitted with four-temperature thermal plasma models, where the temperatures had been *fixed.* I therefore used the e-folding time for the hardness ratio in the decay phase of the flares, as an estimate of their temperature decay times. (Recall that any variation in temperature

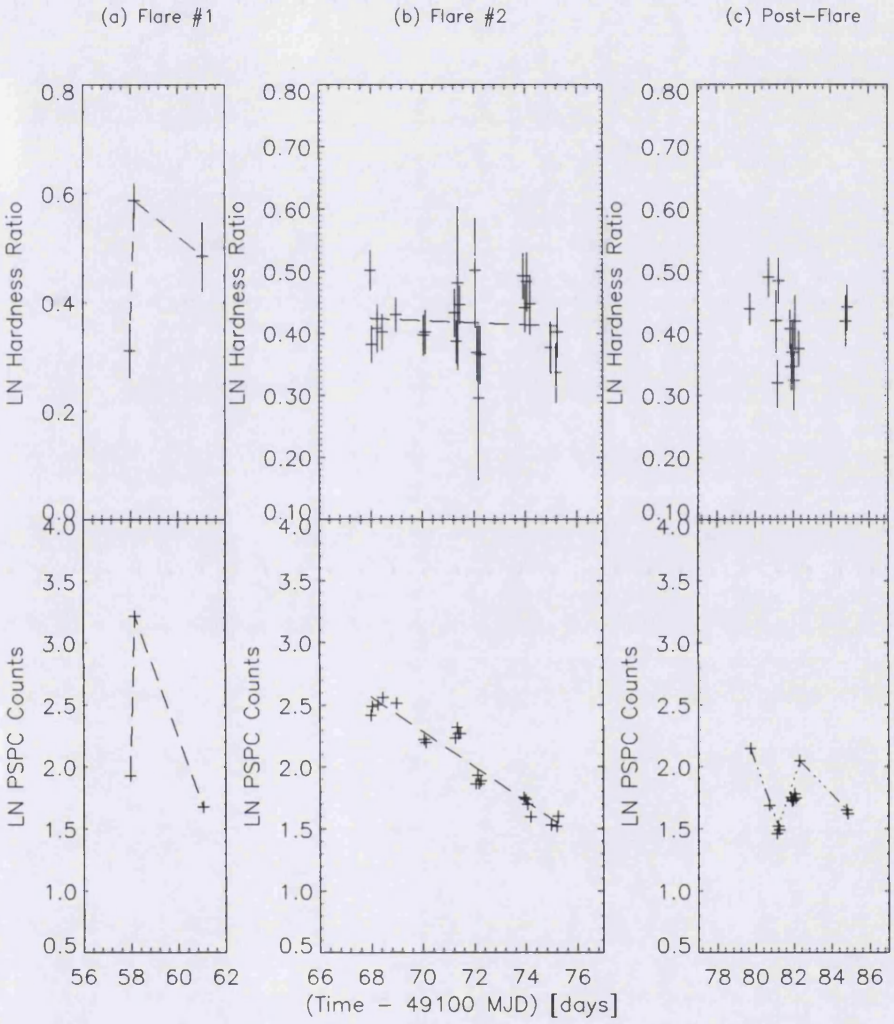

Figure 3.6: *This figure shows that the decay of both the PSPC count-rate and temperature (hardness ratio) of the flares is essentially exponential. Thus e-folding times for these parameters can be obtained and used to derive cooling times for the flares.*

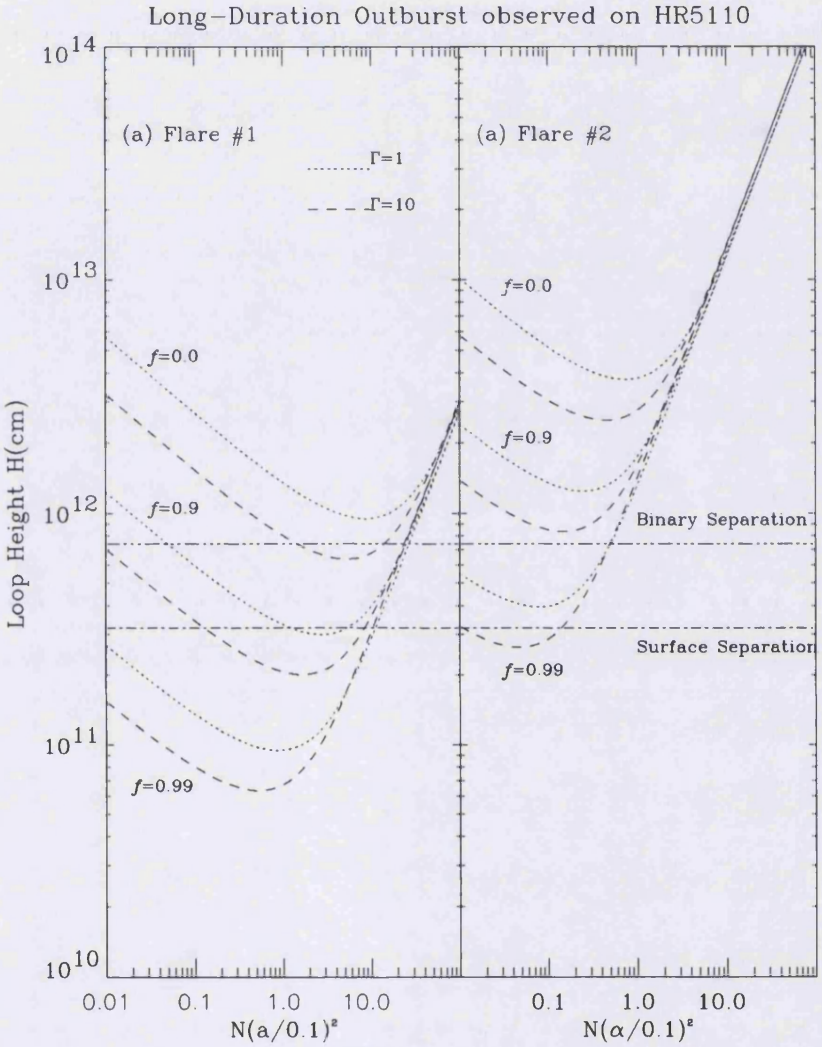

Figure 3.7: *This plot shows the minimum loop heights for the first and second flares, as a function of the unknown parameter, $N\alpha_{0.1}^2$, for Γ values of 1 and 10, where N is the number of flaring loops and α is the aspect ratio of the loop, normalised to 0.1 (a value typical of Solar flares). The labelling convention used for flare #1 is used throughout. Note that for both flares, minimum loop heights of the order of the binary separtion are derived. However for the first flare, the large derived loop heights may have been due to an over-estimation of the decay times due to poor PSPC coverage. Separations were taken from Strassmeier etal. (1988). See text for details.*

should produce a corresponding hardness ratio variation). This gave decay times of $< 2.4 \times 10^6$ and 5.1×10^7 s for the first and second outbursts respectively. This reduces to effective decay times, $\tau_{\rm eff}$, of $< 2.9 \times 10^5$ and 1.2×10^6 s respectively. In the case of the third and fourth flares, the decay of the hardness ratio is poorly constrained. A constant hardness ratio could be assumed (indicating continuous heating, as suggested by the emission measure distribution curves) in which case effective decay times of 4.1×10^5 and 1.0×10^6 s are inferred for the third and fourth flares respectively. However, as in the case of the first flare, these decay times should be considered upper limits due to the poorer PSPC coverage.

The high-temperature component (30 MK), gives the largest emission measure for the flares. I therefore used the initial decay emission measures of this component in the calculations, as these would dominate. These emission measures were $\rm EM_0 = 43.9$ and $16.5 \times 10^{53}\,\rm cm^{-3}$ for the first and second flares respectively.

The minimum loop heights could now be calculated and plotted as in chapter 2. Figure 3.7 compares the calculated minimum loop heights for the first and second flare, for various heating fractions, f and loop expansion factors, Γ. The heating fractions were equivalent to 0, 90 and 99% of the radiative losses, and loop expansion factors considered are for $\Gamma = 1$ — loop with constant cross section— denoted by the solid line, and $\Gamma = 10$ — slightly expanding cross-section—denoted by the dashed line (see chapter 2 for details). Also indicated in the plot are the binary and surface separation of the component stars in the system.

Note that particularly in the second outburst, loop heights greater than the surface separation are obtained, and are comparable with those found for the outburst in chapter 2; i.e. with no heating present, loop heights of 4×10^{12} cm

and 3×10^{12} cm are obtained for this chapter and chapter 2, respectively.

Substitution of the minimum loop heights, H_{min} and corresponding $N\alpha^2$ into the definition of emission measure,

$$EM = \int n_e^2 dV = \frac{\pi}{8} n_e^2 L^3 (\Gamma + 1) N\alpha^2 \ \ cm^{-3}$$

gives a value for the electron densities within the flares (where n_e is the electron density, and α is the aspect ratio of the loop). For the first flare, electron densities ranging from $2\times10^8 - 2\times10^{10}$ cm^{-3} are obtained for heating fractions, f of 0 – 99% of the radiative losses respectively. The upper limit of the electron densities for this flare is 2–3 orders of magnitude lower than for compact flares observed on RS CVn systems (Foing et al. 1994). However it is certainly in the range of typical values for two-ribbon flares on RS CVn systems, given by Van den Oord et al. (1988) and this lends some support to the identification of the first flare as possibly being two-ribbon in nature.

Similarly, electron densities for the second outburst range from 4×10^7 – 4×10^8 cm^{-3}. Note that the electron densities calculated for the second outburst are $\gtrsim 2$ orders of magnitude lower than typical two-ribbon flare values (Van den Oord et al. 1988) and 2 – 3 orders of magnitude lower than those calculated using the KP models. This is because in the KP model, the maximum loop height is constrained to being of the order of the width of the flaring region, thus reducing the flaring volume. By increasing the heating fraction to 99.5% of the radiative losses, a loop height constrained to that of the KP model is possible (since larger amounts of heating require lower loop heights to produce a particular effective decay time). In this case however, the corresponding value for $N\alpha_{0.1}^2 \sim 0.03$ and is approximately two orders of magnitude smaller than typical values for Solar flares, indicating loops which are proportionately long and thin. In a dynamically active magnetic field configuration, demonstrated by HR 5110, the question of stability of such long, thin loops must be raised.

A proper study of the stability of such long thin loops is needed to provide better constraints on the physical parameters of such flaring loops and thus cope with any new possible flare geometries. However, assuming such loops are stable, it can be seen that the derived electron density ($7.5\times10^9\,\mathrm{cm}^{-3}$) is similar in magnitude to that found by the KP analysis, although lower by a factor $\lesssim 2$. Thus the electron density is dependent on the assumed loop height of the flare, which in turn requires knowledge of the amount of heating present. If better constraints on the electron density could be obtained via line diagnostics from high spectral resolution missions such as ASCA (or missions such as AXAF and XMM launched recently) the amount of heating present during the outburst could therefore be better constrained.

For a given heating fraction, the electron densities were also found to be essentially independent of the loop expansion factor, as a larger loop expansion factor results in a corresponding decrease in loop height. This is in agreement with Collier Cameron (1988) who investigated the properties of coronal loop structures of lengths $\gtrsim$ stellar radii for the rapidly rotating active star, AB Doradus. This followed an EXOSAT observation of flaring activity on this star by Collier Cameron et al. (1988) which suggested loop heights in the range 2–4 R_*.

3.4 DISCUSSION

The readiness with which such large loop structures can occur in an active system is demonstrated by the number of recent reports of large flares with long decay times which hint at loop heights of a few stellar radii. These have been observed on a variety of systems e.g. HR 5110 (Wonnacott & Graffagnino, 2000 – which uses some of the results of this chapter; Graffagnino et al., 1995) CF Tuc (Kuerster, 1995; see also next chapter), Algol (Ottmann, 1996),

AR Lac (Ottmann & Schmitt, 1994), Speedy Mic (Kuerster, 1994), AU Mic (Cully et al., 1994), and EV Lac (Schmitt, 1994). The outburst energies displayed in these events have stretched the upper limits of the range of values normally accredited to these systems.

The existence of large stellar loops on chromospherically active single stars raises interesting questions for the development of understanding of the stellar flare phenomenon, particularly when one considers that the Solar-stellar analogy is often an inherent assumption in active-star research: larger energies produced in stellar flares are seen to be a result of the magnetic field being amplified by the dynamo effect due to rapid rotation in a single star (e.g., AB Dor). However, greater amplification of the dynamo effect can be achieved by tidally induced forces within a close binary system.

One of the differences between such large loops in single and binary system could be expected to be the magnetic-field configuration. Uchida and Sakurai (1985) investigated the interactions between the magnetic fields of the two components of RS CVn, assuming a dipole-like field for both stars. Both components were modelled to contain an 'active longitude belt' (ALB) – a large collection of spots, with a collective magnetic field strength of $\sim$ 1kG. The magnetic field configurations for both stars were then computed as the stars rotated. The models showed the usual magnetic loop configurations of active regions observed on the Sun, but also revealed a larger system of loops connecting both stars. These connections would be lost as differential rotation moved any given spot into the ALB, forcing the adjacent spots to take up any surplus magnetic flux. Large pole-to-pole loops would result, as further reconnection between the component stars took place.

If this model is correct, then one may conjecture that the increased flaring state of HR 5110 reported in this paper may have been due to the reconnection

occuring between such large coronal loops as spots are moved into the ALB. Reconnection occuring on such a large scale may account for the continued heating observed in the longer duration flares seen in this system. The high flaring state of HR 5110, and differing morphology of the various flare events, reveal a dynamic magnetic configuration; this may be the normal state of affairs for HR 5110, as hinted by the frequency of such events in the system (twice, in observations separated by two years). Whether this is a result of HR 5110's systemic parameters or is an evolutionary phase which HR 5110 is undergoing, the extreme magnitudes of the energies, duration, electron densities and inter-binary sizes of the flares calculated above, certainly reveal a flare event which differs noticeably from typical two-ribbon stellar flares.

3.5 SUMMARY

A 33ks pointed ROSAT observation of HR 5110 has revealed extreme flaring activity on the system over a period of approximately a month. A number of flare events are identified: An initial very large flare is tentatively identified as being a two-ribbon flare, with energy $\sim 10^{37}$ erg. A long duration event, lasting 7.5 days, followed and exhibited a different morphology in its light curve and signs of continuous heating. It is suggested that this event is similar to the long duration event observed two years previously on the system and detailed in chapter 2. The bolometric outburst energy of the long-duration event is found to be $\sim 2 \times 10^{37}$ erg. Finally, two relatively smaller flares were also observed. Effective decay times for all four flares are found to be of the order 10^5 to 10^6 seconds. From this, derived loop heights of the order of the inter-binary separation (or greater) are found for all four flares, and the second flare (the long duration event) possesses the greatest loop height. Electron densities typical of a two-ribbon flare are derived for the first flare: this is in contrast with

the electron densities derived for the long duration event which are two orders of magnitude lower. Combined with the continuous heating present during the long duration event and the different light curve morphology, this may be indicative of different flare processes from those of the first flare. Furthermore, the size of the loop heights gives further support to the supposition that this may have been an inter-binary flare. The observations presented in this chapter add to the growing pool of evidence, which demonstrate that conditions within the short period RS CVn HR 5110 may be indeed favourable for the production and support of the inter-binary flare phenomenon. However HR 5110 is a non-eclipsing system. Further constraints on these events could therefore be gleaned from the observation of such an outburst from an eclipsing system. Such an event was observed on the system CF Tucanae and the analysis of this event is described in the next chapter.

Chapter 4

CF Tucanæ — A Southern Perspective

There is a theory which states if ever anyone finds out what the universe is for and why it is here, it will instantly disappear and be replaced by something evan more bizarre and inexplicable.

There is another theory which states this has already happened ....

"Hitch-Hikers Guide to the Galaxy", Douglas Adams.

4.1 NOTES ON CF TUCANÆ

Although CF Tucanæ ($\alpha_{2000.0} = 00^h\,52^m\,58.3^s$; $\delta_{2000.0} = -74°\,39'\,07''$,) is a relatively bright (7^{th}-magnitude) southern object, and was first classified as variable by Strohmeier, Knigge and Ott in 1965. Strong Ca II H and K emission from this system was reported by Bidelman and Macconnel (1973)

and later confirmed by Hearnshaw and Oliver (1977) leading them to classify it as an RS CVn system. The system lies at a distance of 54 parsecs, comprising G0V and K4IV components which orbit each other with an inclination of $\sim 71°$ and an orbital period of 2.798 days (Strassmeier et al. 1993).

This orbital period is reported to be *increasing* at the rate of 1 sec/year in direct contrast to the norm for RS CVns (Thompson, Coates and Anders 1991). Thompson et al. partly attribute this to mass-loss from the more active component via coronal holes, a scenario first proposed for RS CVn systems by Hall and Kreiner (1980). Detection of an infra-red excess in the system by Busso et al. (1987) using IRAS observations led them to suggest the possible presence of circumstellar material in the system which would add some weight to the proposed scenario of Hall and Kreiner. However infra-red observations of the system by Antonopoulou (1987) revealed redder colours in the JHK bands than expected, suggesting possibly that the spectral types of the components had been given a wrong classification. Thus higher resolution infra-red spectral work is required to help answer the question of whether there is possible mass-loss within this system.

In the optical wavelength regime, analysis of UBV photometry data by Budding and McLaughlin (1987) revealed a small photometric variation, which they attributed to a reflection effect, as in the case of HR 5110 (Hall 1980). These observations, however, did not provide full phase coverage. Other observations which however did, included those of Collier Cameron, Hearnshaw, and Austin (1981). Their observations dislayed a photometric wave ($\Delta m \sim 0.3$) which they attributed to the presence of starspots.

CF Tucanæ was found to be an X-ray source by the low-energy detector (LED) carried onboard the *HEAO 1* satellite. The system has since been detected in the ROSAT PSPC all-sky survey, and its PSPC X-ray light curve

displays rotational modulation (Kürster and Dennerl 1993). They suggested this was due to coronal inhomogeneities which correlated well with the position of starspots revealed by contemporaneous optical Doppler imaging of the system. This prompted Kürster to propose for additional observing time during the pointed phase of the ROSAT mission. The proposal was accepted, and the observations were made during the ROSAT AO-2. The results of Kürster's analysis were reported briefly in conference proceedings, (1995) and revealed that during the pointed observation CF Tucanæ underwent a 9-day flare. This observation was of particular interest to the work herein. The physical similarities between HR 5110 and CF Tucanæ imply that an inter-binary flare scenario envisaged for HR 5110 could also be applicable to CF Tucanæ. If this is so, then the higher orbital inclination of CF Tucanæ may provide further spatial information on these events. The pointed data were therefore re-analysed as part of this thesis project and are the subject of this chapter.

4.2 THE DATA

The 64 ks pointed ROSAT observation of CF Tucanæ was carried out over a period of a month, between October 2 and November 11 1992. As mentioned above, a preliminary lightcurve of these observations for conference proceedings revealed that CF Tucanæ had undergone a long duration outburst lasting several days (Kürster 1995). Archived PSPC and WFC (S1a filter) data were retrieved from MPE and the LEDAS database respectively.

4.3 THE ANALYSIS

The analysis methods followed those detailed in the previous chapters, using the ASTERIX suite of programs. I obtained clean times for the observation

and these were applied in extracting the light curves and spectra. (To obtain the lightcurves the data were again binned on the orbital period of ROSAT).

4.3.1 The Lightcurves

The observations, which were spread out over a period of $\sim$ 5 weeks, revealed a large flare, which lasts just over 9 days, followed by a quiescent phase, which is separated from the initial long duration outburst by a data gap of a few days. The PSPC and WFC lightcurves can be seen in Figs. 4.1 and 5.1 for the flare and quiescent portions of the observation respectively.

Unlike the observations of HR 5110 reported in chapters 2 and 3, the start and impulsive rise of this flare were seen. From a quiescent PSPC count rate of 2.5 counts/s on MJD 48903.7 (a factor $\sim$ 2 greater than found in the ROSAT all-sky survey) a peak value of just under 33 count/s was reached in $\sim$ 1.9 days. The decay phase of this flare can be seen to follow in two distinct stages: an initial rapid decay lasting just over a day (with an *e*-folding time $\sim$ 0.8 day) followed by a more gradual decay time lasting $\sim$ 7 days (*e*-folding time $\sim$ 4.5 days).

4.3.2 Spectral Analysis and Comparison of Spectral Models

I extracted and background subtracted a total of thirty-two PSPC spectra covering the whole observation (see table 4.1 for details). I chose the start and end times for each spectrum by examining the PSPC lightcurve and hardness ratio plots for any obvious spectral changes and/or data gaps. Twenty spectra cover the flare stage and twelve cover the quiescent stage of the observation. This large number of spectra allowed spectral variations to be followed as the flare progressed.

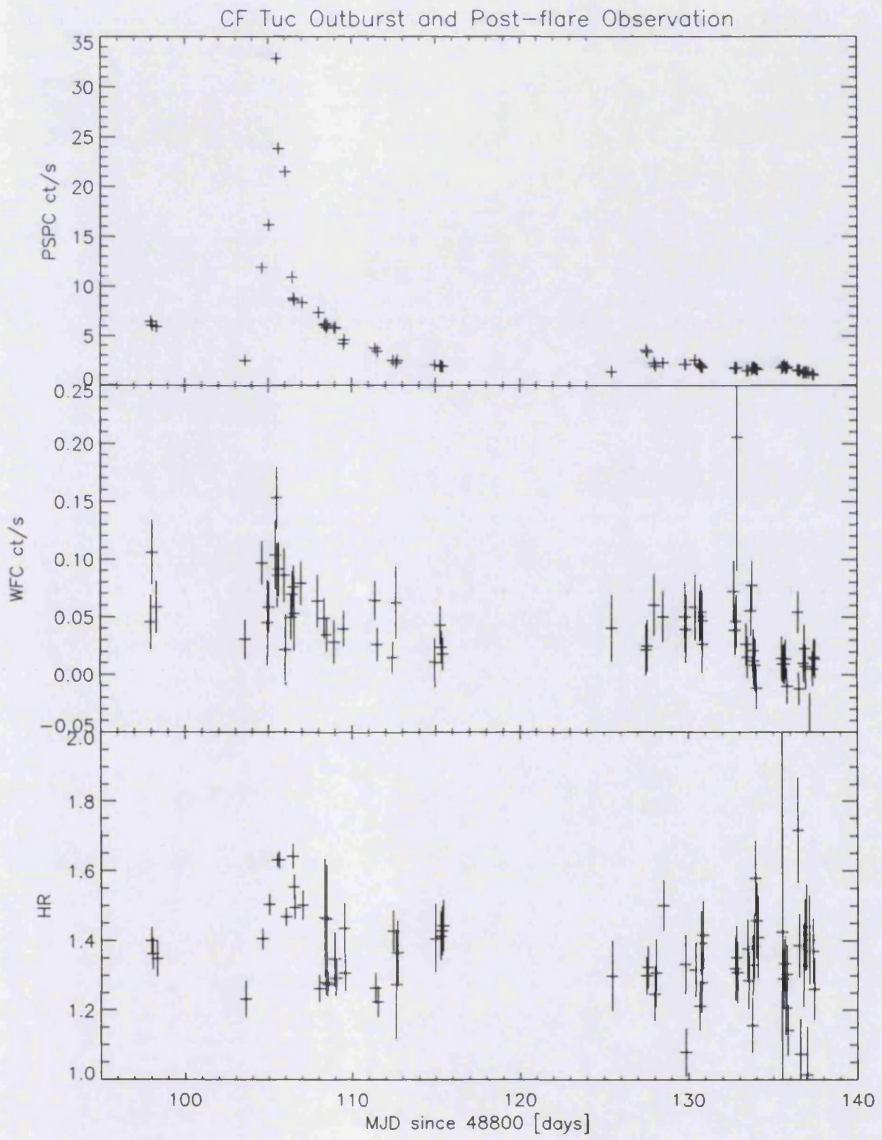

Figure 4.1: *The ROSAT PSPC (a) and WFC (b) lightcurves for the CF Tucanæ observation (flare and postflare).*

#	Start Time [MJD]	End Time [MJD]	Phase	Integration Time [ks]
1	48897.98	48898.18	2.59	2.453
2	48898.24	48898.51	2.68	0.757
3	48903.45	48903.79	4.55	1.344
4	48904.45	48904.79	4.91	1.244
5	48904.92	48905.19	5.09	1.056
6	48905.39	48905.52	5.22	1.457
7	48905.59	48905.72	5.27	1.424
8	48905.92	48906.19	5.45	1.061
9	48906.32	48906.52	5.54	2.706
10	48906.52	48906.72	5.62	1.433
11	48906.92	48907.19	5.80	1.054
12	48907.93	48908.13	6.16	1.056
13	48908.26	48908.66	6.29	2.752
14	48908.86	48909.13	6.47	0.994
15	48909.40	48909.59	6.65	1.368
16	48911.33	48911.60	7.32	2.772
17	48912.33	48912.53	7.68	1.492
18	48912.60	48912.80	7.77	0.784
19	48914.87	48915.34	8.62	1.898
20	48915.34	48915.54	8.75	2.609
21	48925.36	48925.56	12.33	0.806
22	48927.43	48927.70	13.13	1.898
23	48927.90	48928.63	13.40	2.634
24	48929.70	48929.97	13.94	1.490
25	48930.30	48930.97	14.20	3.822
26	48932.70	48932.97	15.01	2.482
27	48933.37	48933.64	15.23	2.115
28	48933.71	48934.04	15.36	4.642
29	48935.50	48936.00	16.04	4.363
30	48936.53	48936.74	16.35	2.001
31	48936.79	48937.03	16.44	2.585
32	48937.03	48937.52	16.57	3.065

Table 4.1: *Table detailing the time bins within which the spectra were extracted. Spectra N$^{os.}$ 1—20 cover the flare outburst, and N$^{os.}$ 21—32 cover the post-flare* (quiescent) *stage of the outburst.*

The PSPC spectra were extracted as for previous chapters using 6 and 12 arcminute radii circles for the source and background respectively. Within each spectrum time-window, a list of 'clean times' was used to select the data from periods of a specified lower background (as performed for HR 5110). PHA channels 1-11 and 200-256 were ignored (see chapter 2 for details therein).

Two-Temperature Thermal Plasma Models

As reported in previous chapters, a multi-temperature thermal plasma model fits the HR 5110 data better than two-temperature models previously favoured for stellar coronae (despite having the same number of free parameters). However, in the case of CF Tucanæ, due to the poorer signal-to-noise ratio, a two-temperature thermal plasma model does give acceptable fits as judged by the reduced chi-squared (see Table 4.2). These results are displayed graphically in Figs. 4.2 and 4.3 where the evolution of the two-temperature model components are shown.

The reduced chi-squared values obtained for these fits are all fairly reasonable. However, examination of the two-temperature fits displayed in Fig. 4.2, shows that the column density dropped by $\sim$ factor 4 to its minimum value at the peak of the flare. I decided to investigate whether this was an artifact of the fitting process, by checking to see if any correlation existed between the column density and the low-temperature emission measure derived from the spectral fits.

Correlations between fitted parameters

Correlation plots for the two-temperature fits are displayed in Fig. 4.4 for the flare and post-flare portions of the observations. In order to obtain some quantitative estimate of the significance of any correlation (or lack thereof) I

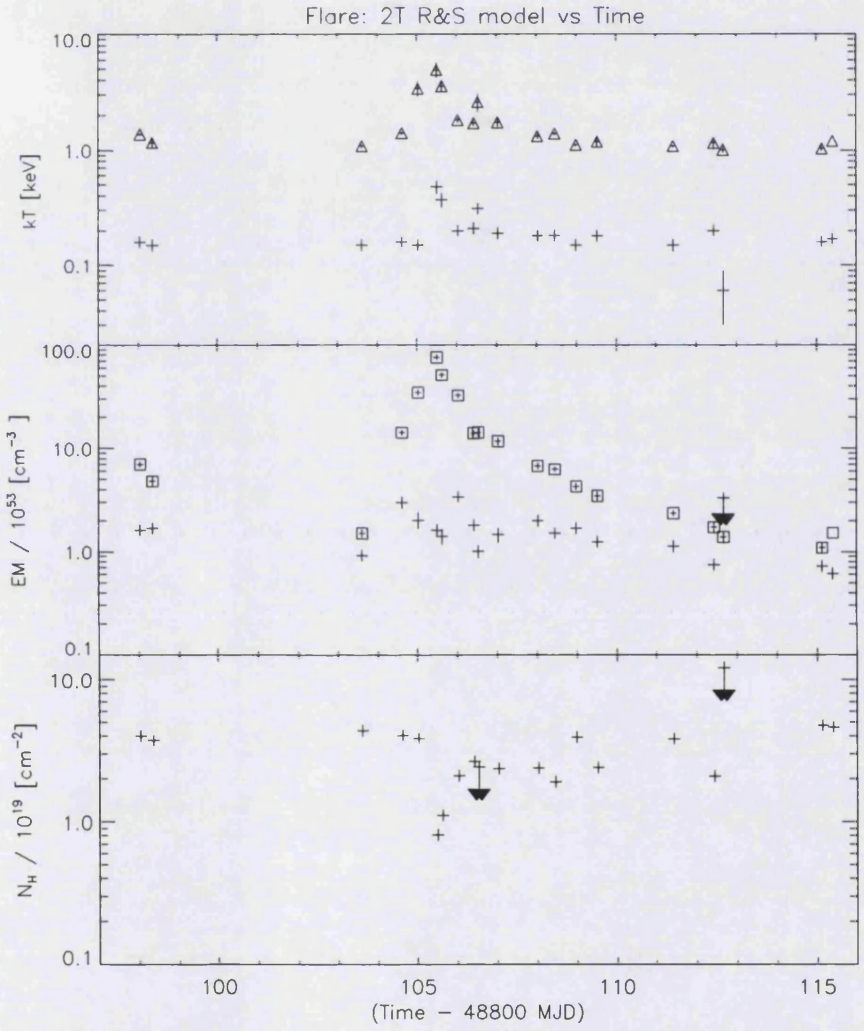

Figure 4.2: *Temperature, emission measure and Hydrogen column-density variations derived from a 2T-Raymond and Smith thermal plasma model fitted to spectra covering the CF Tucanæ flare.*

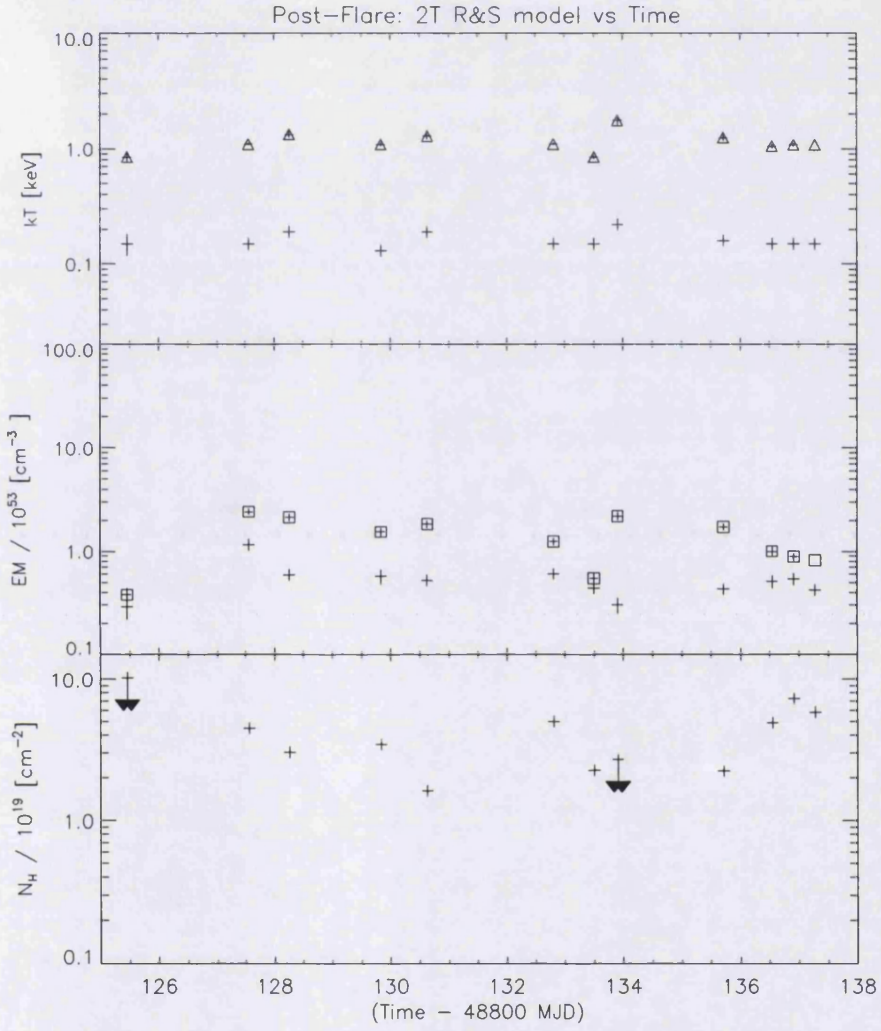

Figure 4.3: *Temperature, emission measure and Hydrogen column-density variations derived from 2T-Raymond and Smith thermal plasma models fitted to spectra covering the CF Tucanæ post-flare (quiescent) stage.*

#	kT_1 [kev]	EM_1 [10^{53} cm^{-3}]	kT_2 [kev]	EM_2 [10^{53} cm^{-3}]	N_H [10^{19} cm^{-2}]	χ^2_ν	(dof)
1	0.16 ± 0.01	1.62 ± 0.14	1.38 ± 0.03	7.05 ± 0.38	4.00 ± 0.63	1.07	(189)
2	0.15 ± 0.01	1.69 ± 0.21	1.16 ± 0.09	4.80 ± 0.46	3.72 ± 1.04	0.93	(189)
3	0.15 ± 0.01	0.90 ± 0.10	1.08 ± 0.03	1.49 ± 0.13	4.39 ± 1.27	1.19	(189)
4	0.16 ± 0.01	2.97 ± 0.27	1.41 ± 0.03	14.15 ± 0.76	4.06 ± 0.66	1.25	(189)
5	0.15 ± 0.01	2.00 ± 0.34	3.40 ± 0.45	34.68 ± 2.00	3.87 ± 0.71	1.12	(169)
6	0.48 ± 0.06	1.61 ± 0.17	4.93 ± 0.68	76.43 ± 3.60	0.81 ± 0.02	1.18	(183)
7	0.37 ± 0.05	1.41 ± 0.23	3.58 ± 0.34	51.30 ± 2.52	1.11 ± 0.22	1.28	(183)
8	0.20 ± 0.01	3.39 ± 0.39	1.83 ± 0.08	32.47 ± 1.77	2.10 ± 0.51	1.32	(171)
9	0.21 ± 0.01	1.80 ± 0.17	1.71 ± 0.08	14.05 ± 0.75	2.65 ± 0.49	1.29	(189)
10	0.310 ± 0.03	1.01 ± 0.14	2.61 ± 0.45	14.24 ± 1.11	$\lesssim 2.42$	1.29	(153)
11	0.19 ± 0.01	1.46 ± 0.23	1.74 ± 0.13	11.68 ± 0.88	2.36 ± 0.82	1.10	(189)
12	0.18 ± 0.01	1.98 ± 0.19	1.32 ± 0.06	6.75 ± 0.49	2.38 ± 0.76	1.11	(189)
13	0.18 ± 0.01	1.50 ± 0.11	1.39 ± 0.04	6.25 ± 0.34	1.90 ± 0.52	1.31	(159)
14	0.15 ± 0.01	1.68 ± 0.17	1.11 ± 0.02	4.27 ± 0.28	3.92 ± 0.91	1.29	(189)
15	0.18 ± 0.01	1.24 ± 0.12	1.18 ± 0.09	3.46 ± 0.31	2.40 ± 0.82	1.06	(189)
16	0.15 ± 0.01	1.13 ± 0.09	1.08 ± 0.02	2.36 ± 0.13	3.83 ± 0.68	1.31	(189)
17	0.20 ± 0.01	0.74 ± 0.08	1.15 ± 0.13	1.72 ± 0.21	2.09 ± 1.05	0.99	(189)
18	0.06 ± 0.03	$\lesssim 3.3$	1.01 ± 0.05	1.39 ± 0.18	$\lesssim 12.1$	1.34	(51)
19	0.16 ± 0.01	0.72 ± 0.08	1.03 ± 0.04	1.09 ± 0.10	4.76 ± 1.28	1.12	(189)
20	0.17 ± 0.01	0.61 ± 0.07	1.19 ± 0.09	1.52 ± 0.14	4.64 ± 1.16	1.06	(189)
21	0.15 ± 0.03	0.29 ± 0.07	0.85 ± 0.07	0.38 ± 0.06	$\lesssim 10.2$	0.95	(189)
22	0.15 ± 0.01	1.16 ± 0.11	1.10 ± 0.02	2.43 ± 0.15	4.47 ± 0.92	1.22	(110)
23	0.19 ± 0.01	0.59 ± 0.07	1.33 ± 0.07	2.13 ± 0.17	3.03 ± 0.99	1.14	(108)
24	0.13 ± 0.01	0.57 ± 0.09	1.09 ± 0.03	1.54 ± 0.13	3.46 ± 1.61	1.50	(68)
25	0.19 ± 0.01	0.52 ± 0.05	1.29 ± 0.07	1.83 ± 0.14	1.62 ± 0.70	1.34	(123)
26	0.15 ± 0.01	0.60 ± 0.07	1.10 ± 0.02	1.24 ± 0.09	4.99 ± 1.27	1.00	(189)
27	0.15 ± 0.01	0.44 ± 0.05	0.85 ± 0.03	0.55 ± 0.05	2.26 ± 1.06	1.34	(189)
28	0.22 ± 0.02	0.30 ± 0.05	1.76 ± 0.15	2.19 ± 0.18	$\lesssim 2.7$	1.20	(126)
29	0.16 ± 0.01	0.43 ± 0.04	1.25 ± 0.06	1.73 ± 0.12	2.23 ± 0.67	1.03	(127)
30	0.15 ± 0.01	0.51 ± 0.07	1.05 ± 0.04	1.00 ± 0.09	4.90 ± 1.46	1.08	(67)
31	0.15 ± 0.01	0.54 ± 0.07	1.08 ± 0.03	0.89 ± 0.07	7.26 ± 1.66	1.40	(69)
32	0.15 ± 0.01	0.42 ± 0.05	1.08 ± 0.03	0.82 ± 0.07	5.81 ± 1.48	0.98	(74)

Table 4.2: *Spectral Fitting results using a two-temperature Raymond and Smith thermal plasma model. Spectra N^{os} 1—20 cover the outburst stage, whilst N^{os} 21—32 cover the post-flare stage.*

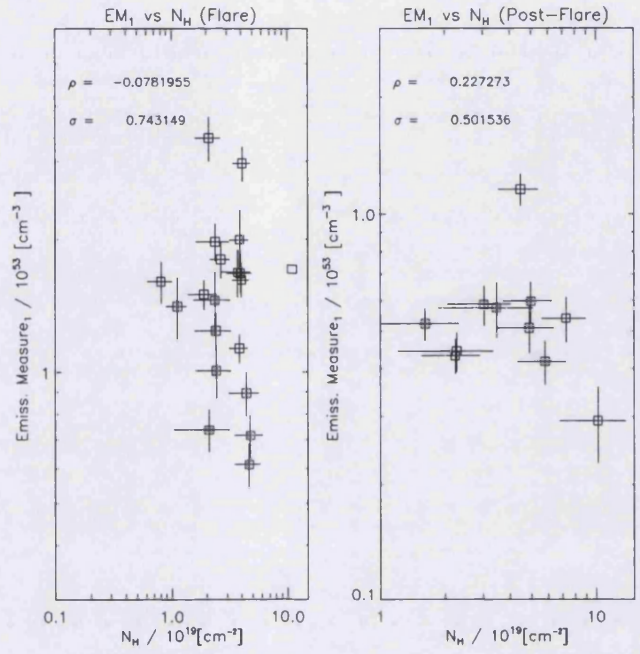

Figure 4.4: *Correlation plots for the low-temperature emission measure component and the hydrogen column density derived from the two temperature spectral fits. Note that no significant correlation is found for either the flare or post-flare portion of the observation.*

calculated the Spearman's rank correlation coefficient, ρ, for the two variables of interest, and these are noted on the corresponding plots.

Rank correlations, in general, provide a more robust statistical measure of correlation between any two quantities of interest than linear correlation coefficients. No *a priori* knowledge of the relationship between the two quantities is assumed. Instead, knowledge of the position (or rank) which a particular data point possesses within the variables of interest is required (see Press et al. 1992 for a more complete disussion on Rank correlations). Spearman's rank

correlation coefficient is defined thus:

$$\rho = \frac{\Sigma_i (R_{x_i} - \overline{R}_x)(R_{y_i} - \overline{R}_y)}{\sqrt{\Sigma_i (R_{x_i} - \overline{R}_x)^2} \sqrt{\Sigma_i (R_{y_i} - \overline{R}_y)^2}} \tag{4.1}$$

where R_{x_i}, R_{y_i}, denote the ranks of the data-points within the variable of interest, X and Y.

A value of $\rho = 1.0$ signifies a perfect correlation and $\rho = -1.0$ signifies a perfect anti-correlation of the two variables. I used the Interactive Data Language (IDL) software package to produce these plots and it includes a function which calculates ρ and the significance, σ, of any correlation found, which lies in the range 0.0—1.0. Small values of σ indicate significant correlations.

These show no correlation between the cool-component plasma and the column density for either the flare or the post-flare stages of the observation as judged by the derived Spearman's rank correlation coefficient, with $\rho = -0.08$ ($\sigma = 0.74$) and 0.23 ($\sigma = 0.50$) for the flare and post-flare respectively.

If there was an obvious problem with the spectral fitting process then one might expect more of a correlation between the coolest temperature plasma and column density, since the relatively lower energy photons which characterize the cooler plasma, would be more readily absorbed. However none exists. Another point worth mentioning is that during the flare, the fitted temperature of the hot component plasma rises to values well above the notional range covered by the ROSAT band-pass. Although the presence of such high-temperature plasma should be detectable by ROSAT, and the two-temperature models probably provide only an approximation to the real situation (Schmitt 1994), another approach may be warranted. I decided to refit the spectra with a multi-temperature thermal plasma model.

Multi-Temperature Thermal Plasma Models

As discussed in chapter 2, a multi-temperature thermal plasma model more properly reflects the physical conditions within the corona, wheras simple one or two temperature models provide a first approximation. In order to provide a better comparison between the spectral results of CF Tucanæ and those of HR 5110, I again fitted four-temperature thermal plasma models, following the spectral fitting methods described for HR 5110. The results of these can be found in Table 4.3.

In Kürster's analysis of the pointed ROSAT CF Tucanæ data (Kürster, 1995), a four-temperature thermal plasma model was also employed to fit the spectra. However, his method differs from the method used in this thesis in that he first fitted the quiescent spectra with a two-temperature thermal plasma model and obtained a mean value for these temperatures and corresponding emission measures. The flare spectra were then fitted with a four-temperature thermal plasma model with two of the temperatures and emission measures fixed to the mean quiescent values. The other two-temperature components (denoting the flare emission) were allowed to vary freely, isolating them from the underlying quiescent coronal emission.

This method is fairly standard and has been used several times previously, e.g. by Ottmann and Schmitt (1994; 1996); by fixing the quiescent temperatures and emission measures, one implicitly assumes that the global coronal emission remains unaffected by the superimposed outburst. In general this approximation can be justified with regard to most flares, particularly for smaller flares. Also consideration of instrument resolution and background and signal-to-noise of the data may dictate that more complicated models are not warranted. However, if an outburst were of a much larger nature, as for instance in the case of inter-binary flares, then it is not clear whether the coronal mag-

Table 4.3: *Spectral Fitting results using a four-temperature Raymond and Smith thermal plasma model.*

#	EM_1 [a] $[10^{53}\,cm^{-3}]$	EM_2 $[10^{53}\,cm^{-3}]$	EM_3 $[10^{53}\,cm^{-3}]$	EM_4 $[10^{53}\,cm^{-3}]$	N_H $[10^{19}\,cm^{-2}]$	χ^2_ν	(dof)
1	2.30 ± 0.46	0.53 ± 0.09	0.59 ± 0.13	8.61 ± 0.49	10.76 ± 1.55	0.94	(189)
2	2.41 ± 0.73	0.44 ± 0.15	1.04 ± 0.21	5.64 ± 0.63	10.71 ± 2.57	0.90	(189)
3	1.37 ± 0.43	0.34 ± 0.08	0.44 ± 0.10	1.66 ± 0.28	12.82 ± 3.01	1.18	(189)
4	4.02 ± 0.88	1.00 ± 0.18	0.93 ± 0.25	17.67 ± 0.99	10.42 ± 1.62	1.03	(189)
5	4.76 ± 1.22	1.16 ± 0.23	$\lesssim 1.90$	30.68 ± 1.51	10.54 ± 1.75	1.12	(169)
6	1.65 ± 0.84	2.38 ± 0.27	1.00 ± 0.38	62.10 ± 2.59	3.77 ± 1.06	1.41	(188)
7	3.55 ± 0.96	1.54 ± 0.24	1.30 ± 0.34	43.41 ± 1.91	7.25 ± 1.26	1.22	(183)
8	4.26 ± 1.04	1.88 ± 0.26	1.03 ± 0.36	35.35 ± 1.70	7.57 ± 1.35	1.21	(171)
9	2.19 ± 0.50	1.05 ± 0.12	0.86 ± 0.16	15.17 ± 0.73	8.97 ± 1.37	1.05	(189)
10	1.28 ± 0.46	0.76 ± 0.14	0.88 ± 0.20	12.39 ± 0.74	5.88 ± 1.69	1.20	(153)
11	2.60 ± 0.80	0.67 ± 0.16	0.71 ± 0.23	12.43 ± 0.82	10.38 ± 2.23	0.99	(189)
12	2.50 ± 0.65	0.88 ± 0.15	0.89 ± 0.20	8.00 ± 0.64	9.54 ± 1.98	0.99	(189)
13	1.34 ± 0.30	0.73 ± 0.08	0.49 ± 0.11	7.69 ± 0.44	6.69 ± 1.32	1.22	(159)
14	2.62 ± 0.66	0.37 ± 0.13	1.20 ± 0.19	4.92 ± 0.54	11.38 ± 2.25	1.29	(189)
15	1.14 ± 0.37	0.59 ± 0.10	0.70 ± 0.14	4.06 ± 0.40	7.80 ± 2.16	1.05	(189)
16	1.59 ± 0.31	0.38 ± 0.06	0.75 ± 0.09	2.61 ± 0.25	11.05 ± 1.68	1.28	(189)
17	0.68 ± 0.29	0.42 ± 0.07	0.41 ± 0.10	1.91 ± 0.27	8.61 ± 2.94	0.94	(189)
18	0.89 ± 0.18	0.18 ± 0.02	0.49 ± 0.12	2.31 ± 0.36	9.99 ± 4.04	1.00	(51)
19	1.07 ± 0.34	0.31 ± 0.06	0.45 ± 0.079	1.00 ± 0.20	13.55 ± 3.08	1.15	(189)
20	0.83 ± 0.27	0.24 ± 0.06	0.27 ± 0.08	1.87 ± 0.20	12.39 ± 2.86	1.04	(189)
21	0.18 ± 0.14	0.17 ± 0.08	0.27 ± 0.10	$\lesssim 3.15$	14.65 ± 2.84	0.96	(189)
22	1.82 ± 0.44	0.37 ± 0.08	0.68 ± 0.11	2.79 ± 0.30	12.82 ± 2.25	1.22	(110)
23	0.85 ± 0.29	0.26 ± 0.06	0.31 ± 0.08	2.47 ± 0.23	11.62 ± 2.75	0.93	(108)
24	0.97 ± 0.31	0.34 ± 1.15	0.48 ± 0.09	1.82 ± 0.27	10.60 ± 2.85	1.43	(68)
25	0.53 ± 0.15	0.24 ± 0.05	0.30 ± 0.06	2.13 ± 0.18	7.43 ± 1.91	1.16	(123)
26	1.23 ± 0.35	0.13 ± 0.07	0.39 ± 0.07	1.34 ± 0.18	15.52 ± 3.03	1.08	(189)
27	0.54 ± 0.16	0.23 ± 0.05	0.46 ± 0.06	$\lesssim 3.81$	8.56 ± 2.53	1.37	(189)
28	0.37 ± 0.13	0.18 ± 0.04	0.16 ± 0.06	2.23 ± 0.16	7.38 ± 2.12	1.02	(126)
29	0.47 ± 0.12	0.13 ± 0.05	0.28 ± 0.06	2.07 ± 0.16	6.86 ± 1.71	0.95	(127)
30	0.79 ± 0.30	0.17 ± 0.07	0.34 ± 0.07	1.16 ± 0.20	13.23 ± 3.60	0.92	(67)
31	1.11 ± 0.38	0.16 ± 0.06	0.28 ± 0.07	1.00 ± 0.16	18.70 ± 3.82	1.30	(69)
32	0.73 ± 0.25	0.14 ± 0.05	0.26 ± 0.06	0.90 ± 0.14	15.39 ± 3.56	0.97	(74)

[a] emission measures 1–4 fitted with fixed temperatures $(1, 3, 10, 30) \times 10^6$ k respectively.

netic loop configurations would be affected on a global scale, perhaps changing the parameters of the underlying (quiescent) emission. Thus, if the underlying component has changed during the outburst, but is assumed fixed in the fitting procedure, the outburst parameters derived will in some way be biased due to the imposed constraints. However, by fixing the four-temperatures and allowing the emission measures to vary (the method used in this chapter as well as chapters 2 and 3) this biassing does not occur. Instead, the emission measures of plasma at those temperatures are sampled, resulting in a better description of the overall spectral behaviour. It should be emphasised that the derived emission measure at a particular temperature is simply the linear sum of quiescent plus flare components at that temperature, *even if* the quiescent component changes.

The evolution of the four temperature components with time is displayed in graphical form in Figs. 4.5 and 4.6. Note that the greater temporal coverage of the CF Tucanæ observation (in comparison with the second ROSAT observations of HR 5110) reveals variations in the emission measure with a behaviour far more intricate than that seen in the HR 5110 outbursts.

4.3.3 Flare Analysis

The light-curve morphology displayed by the CF Tucanæ flare is not typical of most stellar X-ray flares. Instead as with all the largest flare events described in this thesis, the flare decays in two phases: a rapid decay followed by a more gradual one. Minimum loop heights for this flare were calculated following the methods outlined in the previous chapters. I obtained the *e*-folding time for the gradual decay phase, and since the hot component best describes the flare plasma, I used the dominant (30 MK) emission measure obtained from the four-temperature plasma model fits, for the time when the decay rate changes

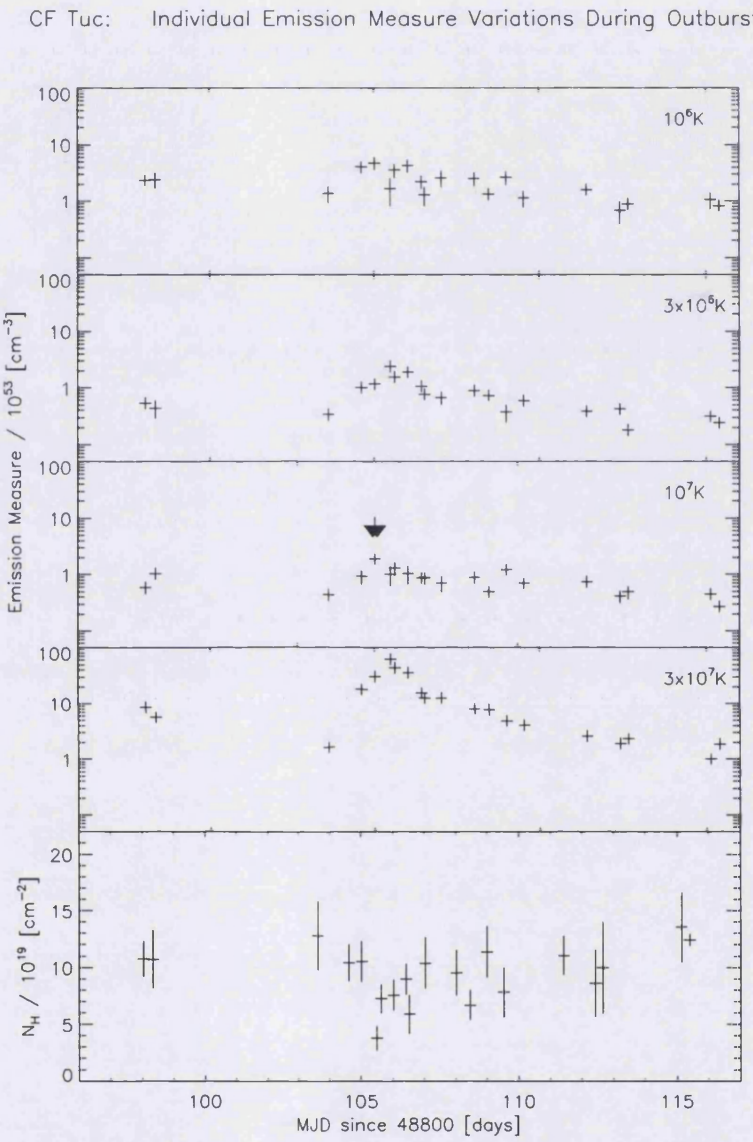

Figure 4.5: *Emission Measure and Hydrogen column density variations derived from a 4T-Raymond and Smith thermal plasma model fitted to spectra covering the CF Tucanæ flare*

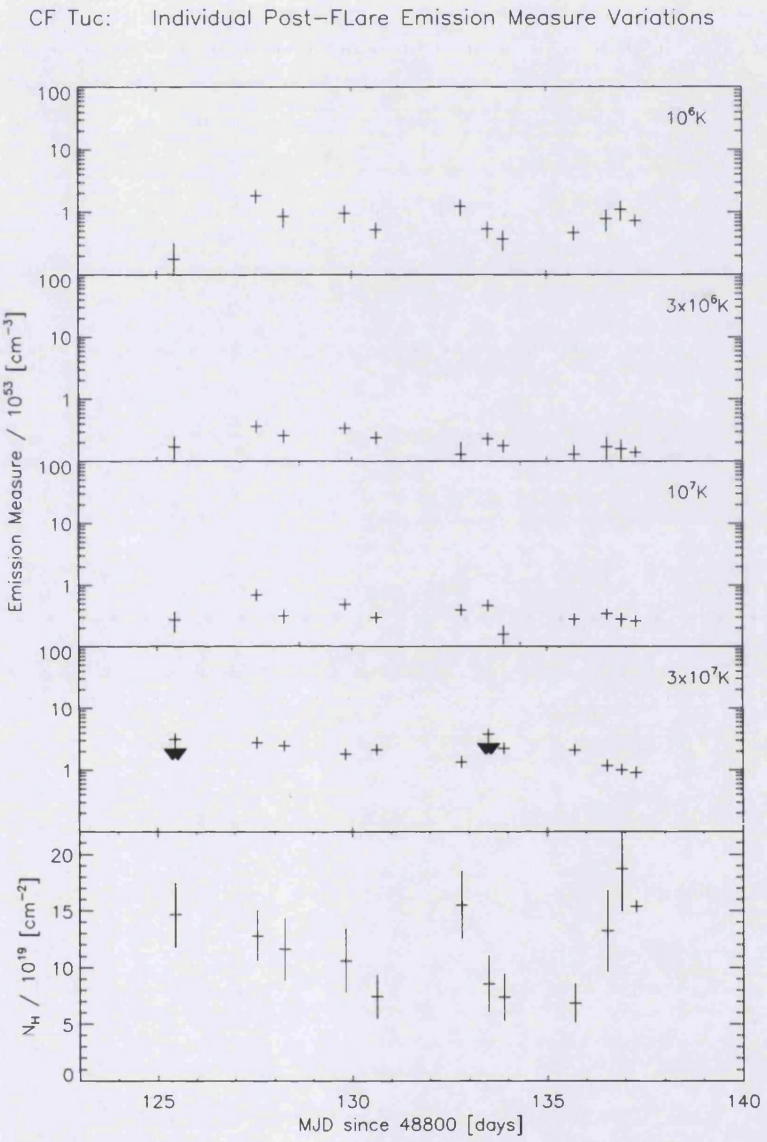

Figure 4.6: *Emission Measures and Hydrogen column density variations derived from a 4T-Raymond and Smith thermal plasma model fitted to spectra covering the CF Tucanæ post-flare stage.*

to a more gradual phase (e.g. for spectrum N°. 10, MJD 48906.62).

No *e*-folding time could be derived for the temperature decay, as the corresponding hardness ratio decay was difficult to constrain, due to the poorer signal-to-noise of these data (in comparison with those of the original HR 5110 observation). However, using only the lightcurve decay time as the effective decay time only introduces a 10% difference from a more correctly determined effective decay time (e.g. Collier Cameron 1989) used in the rest of this thesis, and therefore I calculated the minimum loop heights using the value of the lightcurve decay time. A loop height of $\sim 1.2 \times 10^{12}$ cm was obtained for a rigid loop structure ($\Gamma = 1$), assuming a zero heating fraction. This is approximately half the height calculated for the HR 5110 outburst loop in chapter 2. The results can be seen in Fig. 4.7.

In the case where a zero heating fraction is applied, loop heights of the order of the binary separation can be derived. If continuous heating was occuring, the minimum loop height would be lower than this value. With a heating fraction of 90%, the minimum loop height is reduced to 30% of that with no heating present. Thus for $\Gamma = 1$ the loop height is $\sim 4 \times 10^{11}$ cm, i.e. over half the inter-binary separation of 7.4×10^{11} cm and equal to the surface separation of the system (using radii of 3.3 and $1.7 R_{\odot}$ for the K and G components respectively given in the Strassmeier 1993 catalogue).

Flare model fits were performed to constrain the flare parameters. As in previous chapers, I used the standard Kopp and Poletto models and I also tested for quasi-static cooling. The results can be seen in Figures 4.8 and 4.9. For the Kopp and Poletto model, energy decay rates were derived as described in chapter 3, using the spectral fit parameters of the four-temperature fits. Kopp and Poletto models for $n = 3, 5, 7, 9, 13$, and 17, were produced and fits were made. However, all of these models produced very poor fits as judged by

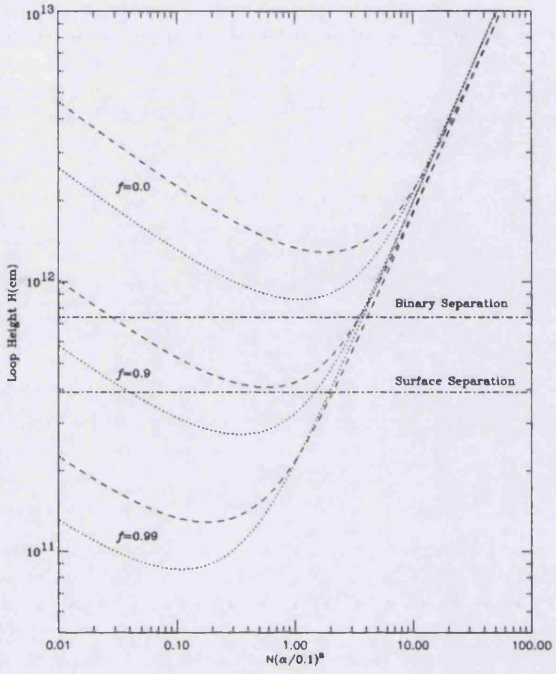

Figure 4.7: *Derived minimum loop heights are plotted for CF Tucanæ outburst decay times, assuming various heating fractions (f = 0—99%), and loop expansion factors. Dashed lines represent loops of constant cross-section ($\Gamma = 1$). Dotted lines represent loops of expanding cross-section ($\Gamma = 10$).*

their χ^2_ν values with the *best* fits giving a $\chi^2_\nu \sim 5$.

Unlike the long-duration outburst for HR 5110 discussed in chapter 3 (where improved fits were obtained by removing the 'second peak', see section 3.3.4) the temperal coverage of the CF Tucanæ outburst was less interrupted than that of HR 5110, thus leaving no room for such an ambiguity. Kürster and Schmitt's attempts at fitting Kopp and Poletto models in their analysis of the same data also produced poor statistical fits. However, future re-analysis of

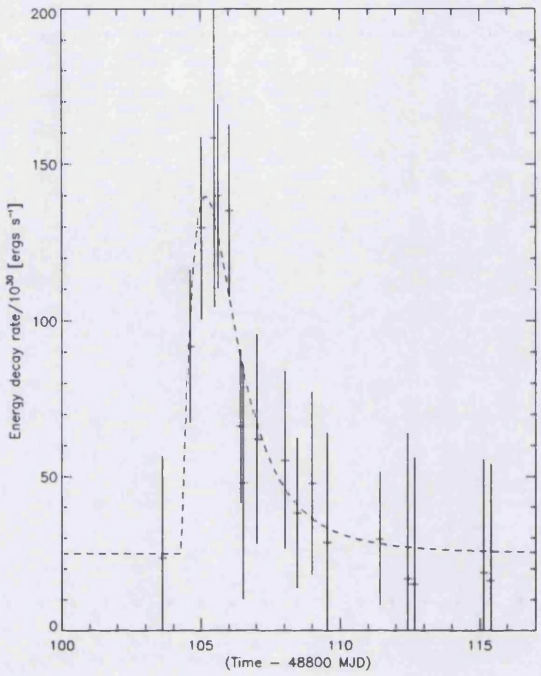

Figure 4.8: *An example of an attempted Kopp and Poletto fit to the outburst data. Best fits obtained (as judged by the reduced chi squared) for all values of loop orders, were* $\chi^2_\nu \sim 5$.

these data may benefit from splitting up the lightcurve into much finer time-bins to better constrain the behaviour of the flare decay, and thus perhaps improve the fit.

For completeness, I tested for quasi-static cooling during the decay phase of the flare. If during the decay phase the flare had cooled quasi-statically, then the ratio of radiative and conductive cooling times would have remained constant i.e.

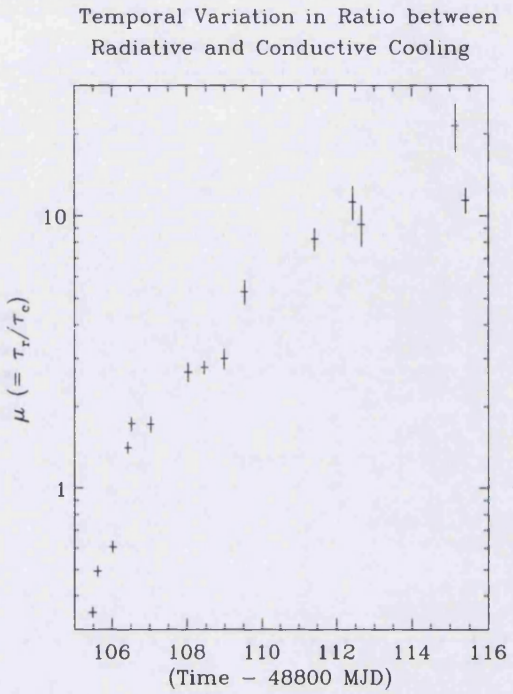

Figure 4.9: *This plot clearly demonstrates that the ratio of radiative and conductive cooling times does not remain constant during the decay phase of the flare.*

$$\mu = \frac{\tau_r}{\tau_c} = 2.6 \times 10^{-3}(H_{10} N \alpha_{0.1}^2)\frac{T_7^{13/4}}{EM_{53}} = \text{constant},$$

where H_{10} is the loop height in units of 1×10^{10} cm, T_7 in units of 10^7 K and EM_{53} is in units of 10^{53} cm^{-3} (equation 2.16 from chapter 2).

The temperature and emission measures that I used are those of the hot (30 MK) component, whose variations more closely follow the behaviour of the light curve, and is the more dominant component, (see Fig. 4.6). As seen from

Fig. 4.9 it is clear that μ does not remain constant during the decay of the flare, indicating that quasi-static cooling is not taking place. Instead, an increase in μ is observed to occur in two stages. An initial rapid increase in μ suggests that conductive cooling is predominant in the beginning stages of flare decay. Radiative cooling then dominates for the remaining majority of the flare decay. This is consistent with what has been observed on the Sun (e.g. Craig 1981). Note therefore, that the non-constant behaviour of μ during the flare decay is indicative that the flare could not have been compact in nature.

4.4 SUMMARY

In this chapter I have discussed ROSAT observations of another long-duration flare, this time occuring on the RS CVn system CF Tucanæ. Unlike the HR 5110 observations presented in earlier chapters, these observations show the state of the system prior, during, and as will be seen in the next chapter, after the long-duration event itself, thus allowing examination of the system at all relevant stages. The impulsive rise of the flare was observed and again the light-curve morphology of the flare behaved differently from that of most stellar X-ray flares, displaying an initial rapid decay lasting over a day followed by a much more gradual decay stage lasting approximately seven days. A quasi-static cooling analysis showed that such cooling was not taking place indicating that the flare could not be compact in nature. An outburst energy of $\sim 2 \times 10^{37}$ ergs was derived for the flare and an attempt to fit Kopp and Poletto flare models to the data produced poor fits with best fit $\chi^2_\nu \sim 5$ for a range of n values. Thus Kopp and Poletto models did not produce good statistical fits to the data. Although these flare models were again inadequate to describe the flare decay, future re-analysis of these data may benefit from binning the data with greater time resolution, in order to better constrain the

flare decay. Analysis of the flare decay also revealed loop heights of the order of the inter-binary separation, as was the case for HR 5110. Thus it is possible that the observation presented in this chapter provides a further example of an inter-binary flare within RS CVns. In the following chapter, I will examine the post-flare quiescent state of the system and highlight the consequences to the sytems environment in the aftermath of such large outbursts.

Chapter 5

CF Tucanæ — The Aftermath

"Properly speaking, of course, there is no such thing as a return to nature, because there is no such thing as a departure from it. The phrase reminds one of the slightly intoxicated gentleman who gets up in his own dining room and declares firmly that he must be getting home...."

G. K. Chesterton *from Chesterton Review, August, 1993*

5.1 THE POST-FLARE/QUIESCENT STAGE

So far in this thesis, I have concentrated my discussions on the analysis applied to the long-duration flare events observed in both HR 5110 and CF Tucanæ. In chapter 3 it was noted that following the HR 5110 outburst the X-ray countrate of the post-flare stage did not return to that of the (presumed) quiescent value from the all-sky survey. Instead the countrate was at a level of twice the survey value when the observation ended approximately ten days after the

long duration event. Similarly, the CF Tucanæ observations presented in the previous chapter were of sufficient duration to reveal even more detail of the post-flare coronal behaviour, and provided a further twelve days of coverage following a post-flare data gap of nine days. This chapter will therefore present the analysis of this post-flare data and the results obtained.

Figure 5.1 shows the post-flare lightcurves for CF Tucanæ in both the PSPC and WFC and also includes the PSPC hardness ratio for this portion of the observation. The hardness ratio was defined as the counts from the hard band (0.29 – 2.00 keV) divided by the counts in the soft band (0.1 – 0.28 keV). Note that at the start of the *quiescent* stage (on $\sim$ MJD 489125.5) the PSPC countrate had reached the survey value of 1.01 $\pm$ 0.09 ct/s (to within 3σ of the survey value), however after another data gap (this time of only two days) the count-rate increased by approximately a factor three, due to a small flare. Closer examination of the post-flare PSPC light curve reveals a number of small peaks, the amplitudes of which decreased with time, and by the end of the observation the countrate has again reached the all-sky survey value.

As CF Tucanæ is a partially-eclipsing system, I decided to phase the PSPC and WFC light curves in order to search for eclipses and/or evidence of rotational modulation within the system. Note that previous WFC observations of active stars demonstrating rotational modulation are quite sparse. Amongst the WFC survey observations, analysis of a large, homogeneous, sampling of active stars (127 in total) undertaken by Tsikoudi and Kellett (1997) found no statistical evidence for rotational modulation. Instead the authors ascribed variabililty in their data to possible small scale *milliflaring*. Although no RS CVns were included in their study, the authors believed that a follow-up study, being carried out at the time on the RS CVns, would also fail to find evidence of rotational modulation (Kellett 1997). Unfortnately results from this

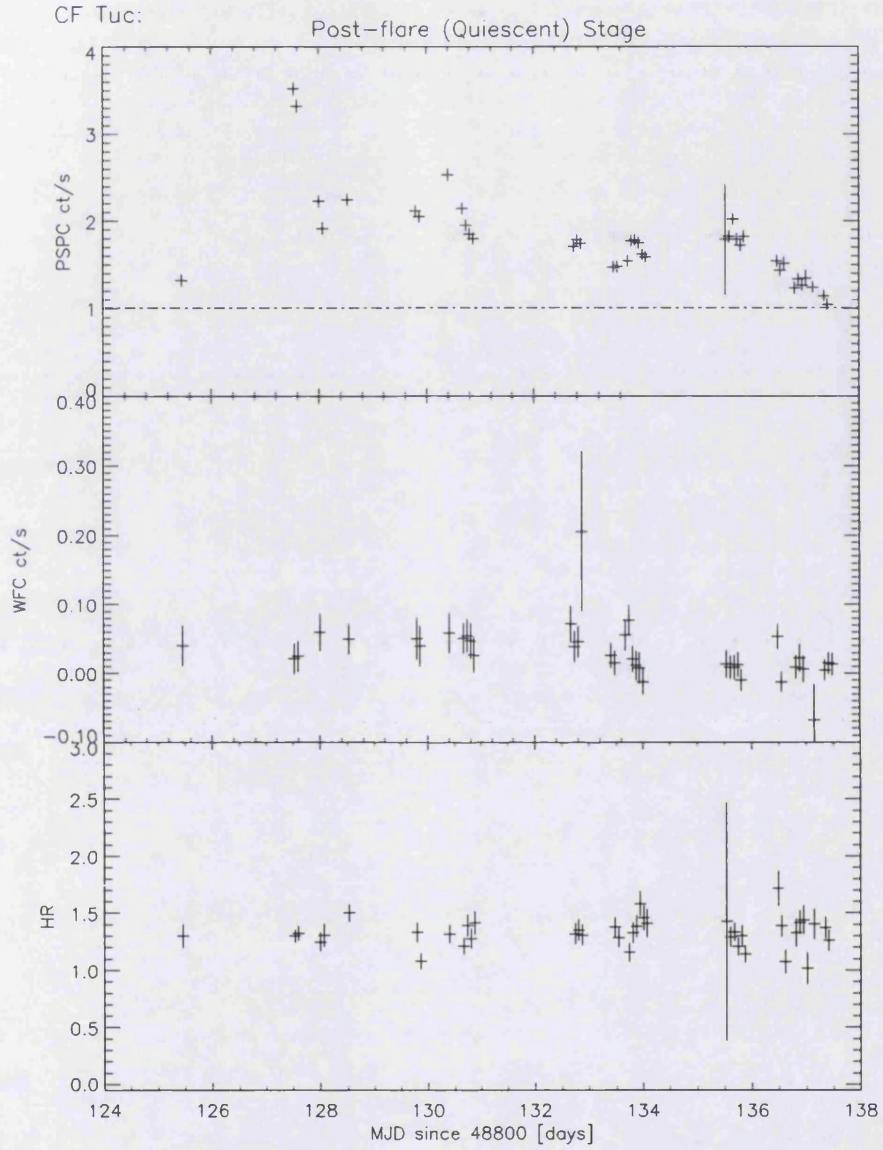

Figure 5.1: *The ROSAT PSPC (a) and WFC S1a Filter (b) lightcurves of the CF Tucanæ quiescent phase. (Note that the errors for the PSPC count-rates are hidden by the symbol used) The Dash-dotted line denotes the survey count-rate given by Kürster and Dennerl (1993).*

follow-up study have yet to be published. However, results from an analysis of the WFC survey observation of the RS CVn system V711 Tau by Barstow et al. (1992) certainly does suggest the presence of rotational modulation. Although Barstow et al.'s interpretation is somewhat tentative due to the poor temporal coverage and noise present in their data, later EUVE observations of V711 Tau have definitively reinforced this result of rotationally-modulated EUV emission (Drake et al. 1994).

In order to phase the data, I first converted the Modified Julian dates of each data point into a Heliocentric Julian date. The phase of each data point was then calculated using,

$$\phi = (t - t_0)/P$$

where ϕ is the phase, P is the period (2.797673 days from Kürster, 1995), t and t_0 are the Heliocentric Julian Date of the observation and zero-phase respectively, with t_0 taken from the ephemeris of Budding (1985). The reported increase in orbital period of 1 s/year (Thompson et al. 1991) has a negligible effect on this ephemeris and the following results. Here zero-phase is defined as the phase of optical primary eclipse.

Determination of the *quiescent* counts within both the PSPC and WFC lightcurves were selected as follows: a mean count-rate was obtained from the post-flare portion of the PSPC (0.1 – 2.0 keV) observation. The sum of the mean countrate and three-sigma error (2.52 ct s^{-1}) was then used as an upper limit for the quiescent counts in the PSPC. The whole PSPC light-curve was then examined and times for count-rates below the cut-off value were selected.

WFC counts from these quiescent time bins were extracted and then binned into ten phase-bins to improve count statistics. The phased WFC lightcurve is displayed in Figure 5.2. Notice the depression clearly evident, in which the WFC countrate drops to a minimum at $\phi \sim 0.5$ by $\sim$ 56% from its

peak value at phase $\phi \sim 0.0$, i.e. the dip occurs at secondary optical minimum. If one recalls the introductory discussion above concerning the detection of rotational-modulation, this is clearly an interesting discovery in the CF Tucanæ system. A search for similar behaviour in the PSPC lightcurves was therefore attempted, with the aim of providing insight into the post-flare coronal structure.

The resulting phased PSPC hard and soft band light curves are displayed in Figs 5.3 and 5.4. They have been plotted using different symbols for successive pairs of orbital cycles, with the symbols and their corresponding cycle numbers plotted for each light curve in its adjoining key. The corresponding hard and soft band lightcurves have also been plotted using the same symbols in order to more easily identify these cycles.

Both phased lightcurves show what could be described as a wave-like variation with minimum countrate occuring around phase $\phi = 0.5$ for each band. This would be consistent with evidence for rotational modulation found in the survey PSPC observations (Kürster and Dennerl 1993). However, note that for the observations presented in this chapter, full phase coverage of each orbital cycle is not available. Orbital cycles 1566–1568 provide the most complete orbital coverage, and this only in the case of the hard-band lightcurve. Thus any interpretation of the phased PSPC lightcurves must be made with this in mind and therefore is tentative.

Phased Hard-Band Lightcurve

Although the depression in the phased lightcurve may be due to rotational modulation indicating the presence of an active region (see section 5.1.1 for further discussion), other interpretations are possible. The observed wave-like variation may not be a real effect and could simply be due to the incomplete

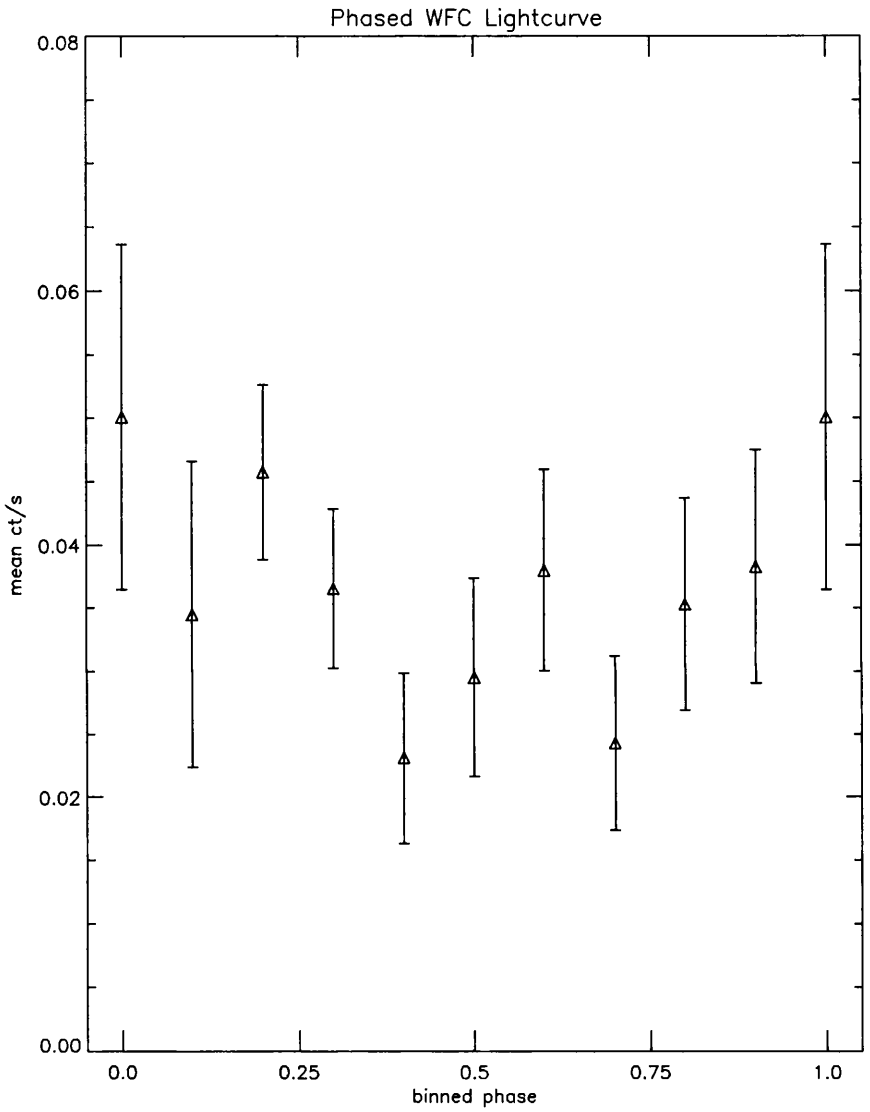

Figure 5.2: *The Phased WFC lightcurve of the quiescent stage of the CF Tucanæ observation. The quiescent counts have been binned into ten phase-bins and plotted.*

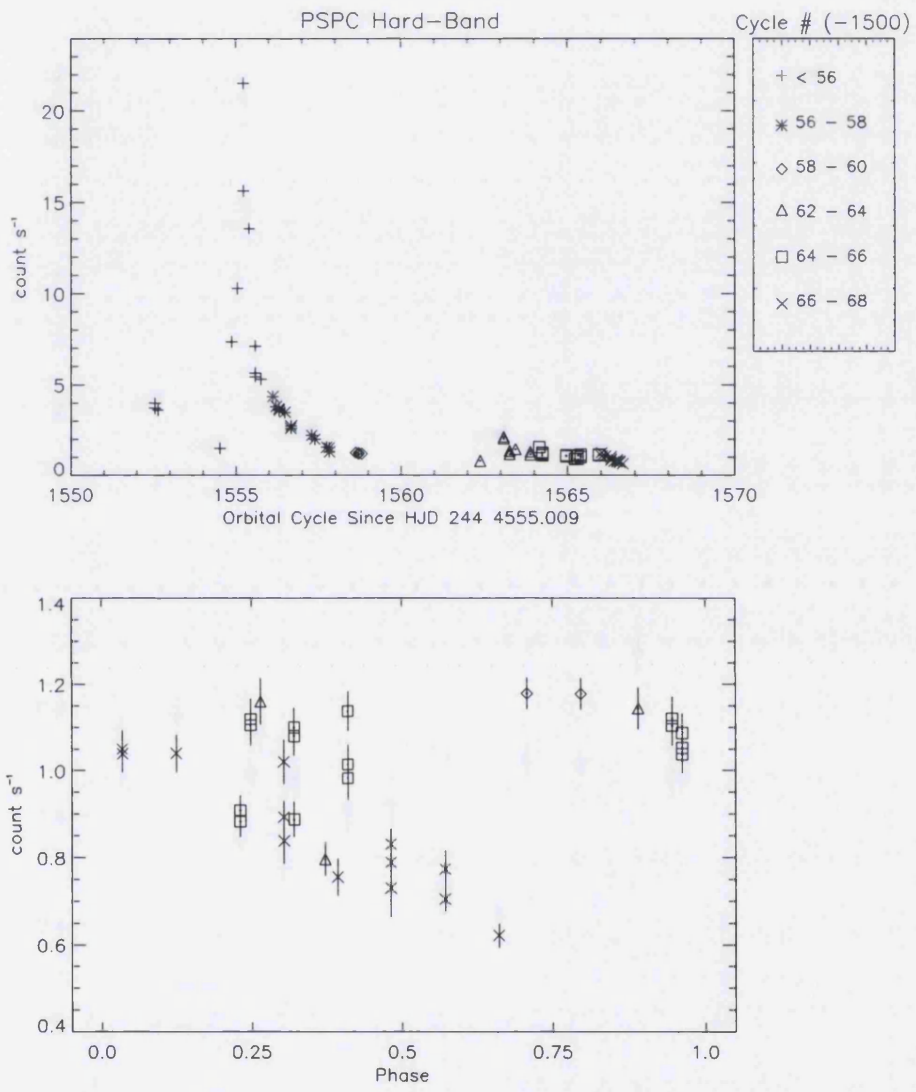

Figure 5.3: *The top panel displays the PSPC hard-band lightcurve of the entire CF Tucanæ observation. The different symbols denote different orbital cycles and are identified with their corresponding cycle number in the key. The lower box displays the phased lightcurve using the same plotting symbols.*

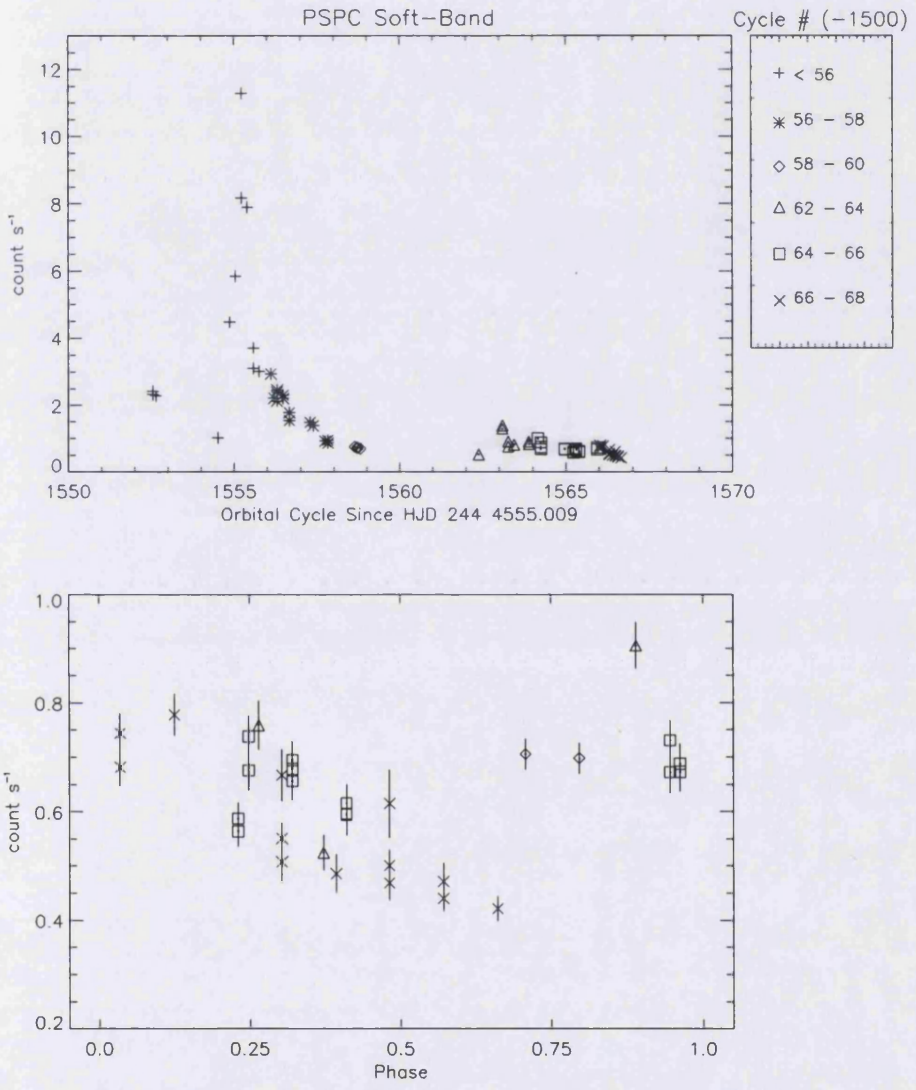

Figure 5.4: *The Phased PSPC soft-band lightcurve of the entire CF Tucanæ observation. The different symbols denote different orbital cycles and are identified with their corresponding cycle number in the key. The lower box displays the phased lightcurve using the same plotting symbols.*

phase coverage in most of the orbital cycles. The observed depression in countrate could therefore be stochastic in nature and perhaps result from the decay of a number of small flares. If the variations are real however, an alternative explanation is that an eclipse has been observed.

X-ray observation of eclipses in binary systems are often used as structural probes to derive spatial information about the extent of the coronæ (e.g. White 1986). Thus in order to try and deduce the post-flare coronal structure, I assumed that the depression observed in the lightcurves is due to an eclipse within the system, and examined the hard and soft-band PSPC phased lightcurves, following the methodology of previous authors (e.g. Ottmann 1994).

In the hard band, a depression is observed around phase $\phi = 0.5$, i.e., during secondary optical eclipse (corresponding to eclipse of the K-star component), with $\sim$ 40% reduction in countrate from maximum. Such a large reduction would not be unexpected, as the secondary K-star is presumed to be the more active component, and therefore would provide most of the X-ray flux.

Note that the depression actually begins prior to $\phi = 0.5$, beginning at $\phi \sim 0.4$ at the beginning of cycles 1564–1566. (Note also that the start of eclipse seems to occur at an earlier phase towards the end of cycles 1564-1566 and later - this is discussed below in the section on column density variations). The scale height of the corona on the K star can be constrained, using this value for ϕ. Fig. 5.5 displays a representation of the system used to calculate the height of the quiescent corona, using the stellar radii $R_G = 1.67\mathrm{R}_\odot$, $R_K = 3.32\mathrm{R}_\odot$ and binary separation, $A = 10.7\mathrm{R}_\odot$ (Strassmeier et al. 1993). In Fig. 5.5 and the following calculation, $H_K = R_K + H_C$, where H_C is the coronal scale height. For simplicity and ease of calculation, the inclination of

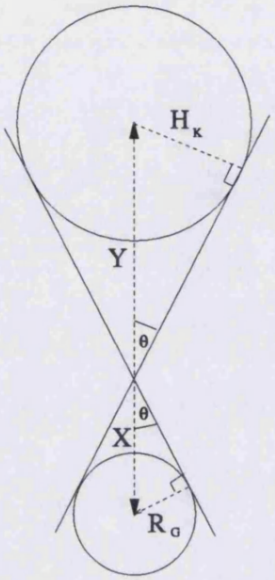

Figure 5.5: *Diagram to aid in visualising the eclipse of the CF Tucanæ system, assuming total eclipse (a simplifying approximation) used in deriving the coronal scale height of the CF Tucanæ system. (See text for details.)*

the system, ($\sim$ 71°, Strassmeier et al. 1993) has been assumed to be 90°. In reality an inclination of 71° would introduce a fractional decrease in the eclipse duration of 92% compared with that of a 90° inclination. Thus the following calculations provide lower limits.

The angle θ in Fig. 5.5 represents the phase difference observed, $\Delta\phi$, between optical minimum at $\phi = 0.5$ and the start of eclipse, which for the end of cycles 1564–1566 occured at $\phi = 0.4$, making $\theta = 2\pi\Delta\phi = (2\pi \times 0.1)$. I employed the method followed by Ottmann in his analysis of Algol (1994), to produce the following relations and derive a value for the coronal scale height. The binary separation of the system ($10.7\mathrm{R}_\odot$, Strassmeier 1992) can be written as:

$$X + Y = 10.7\mathrm{R}_\odot \tag{5.1}$$

From Fig. 5.5 it can be seen that the phase difference, represented by angle θ [$= \sin(2\pi\Delta\phi)$], can be expressed as,

$$\sin(2\pi\Delta\phi) = \frac{R_G}{X} = \frac{H_K}{Y} \tag{5.2}$$

Substitution of equation 5.1 into 5.2 and rearranging the result gives,

$$H_K = 10.7\mathrm{R}_\odot \sin(2\pi\Delta\phi) - R_G \tag{5.3}$$

By substituting the values of R_G into equation 5.3 a value of $4.62\,\mathrm{R}_\odot$ for H_K is obtained. However H_K is the sum of the K star radius and its coronal height, therefore subtracting R_K from this value gives a coronal height of $1.3\mathrm{R}_\odot$ for the K star. If I repeat this calculation and use the value of $\Delta\phi = 0.25$ (i.e the phase difference value for the latter end of cycle 1564-1566 and later cycles) then I obtain a value of $5.2\mathrm{R}_\odot$ for the coronal height. If this earlier phase eclipse is due to circumstellar material or some pronounced coronal structures resulting from the outburst, then this provides a constraint on the extent of such material/structures. Thus the *height* of the K star corona (H_C)can be constrained to $1.3\mathrm{R}_\odot \lesssim H_C \lesssim 5.2\mathrm{R}_\odot$. Ottmann et al. (1993) derived a coronal height of $1.9\mathrm{R}_\odot$ for the K star in AR Lac using EXOSAT observations, a value comparable with the lower limit derived above. Thus the CF Tucanæ results appear quite reasonable.

Phased Soft-Band Variations

As mentioned above, the variation with phase of the soft-band lightcurve is not as pronounced as in the hard-band. Again some uncertainty in this interpretation is introduced due to incomplete orbital phase coverage and data scatter. However assuming that the interpretation of this depression as being due to an eclipse is correct, the calculations detailed in the previous section can again be performed. The eclipse in this case starts at $\phi \sim 0.25$ (as for the

early start of eclipse in the hard-band) constraining the softer X-ray emission to a coronal scale height of $H_C \lesssim 5.2 R_\odot$. Obviously the uncertainty in the calculated values for the scale heights of the K stars corona are increased by the fact the system is only partially eclipsing. Thus the polar regions of the K star which would be visible and any active regions on the K star, not eclipsed by the primary, will contribute to the observed X-ray lightcurve.

Post-Flare Column Density Variations

Transitory increases in the hydrogen column density during flares have previously been detected. Examples include a flare during an *Einstein* observation of Proxima Centauri (Haisch et al. 1983), and a ROSAT pointed observation of a long duration flare on the RS CVn system AR Lac (Ottmann & Schmitt 1994). I decided to examine the column density values for CF Tucanæ to see if any similar behaviour was exhibited.

Fig. 5.6 compares the fitted hydrogen column density as a function of orbital phase for both the flare and post-flare portions of the CF Tucanæ observation. Also plotted is the weighted mean of the column density for the whole observation, $N_{H_o} = (8.8 \pm 2.5) \times 10^{19} cm^{-2}$. This is of the order of the local neutral hydrogen distribution ($\sim 10^{19} cm^{-2}$ from Paresce 1984) at the Galactic longitude and latitude of CF Tucanæ ($l = 302°.81$, b=–42°.48).

Note that both the flare and post-flare column densities are generally in good agreement at the one sigma level (denoted in Figure 5.6 by dotted lines), although the post-flare column density may appear to be slightly higher. [Weighted mean column densities are $N_{H_f} = (8.3 \pm 2.2) \times 10^{19} cm^{-2}$ and $N_{H_{pf}} = (10.4 \pm 2.8) \times 10^{19} cm^{-2}$ for flare and post-flare respectively.] A comparison between the four-temperature and corresponding two-temperature fit results (e.g. Figs. 4.3 and 4.6 of chapter 4) displays a similar behaviour in the

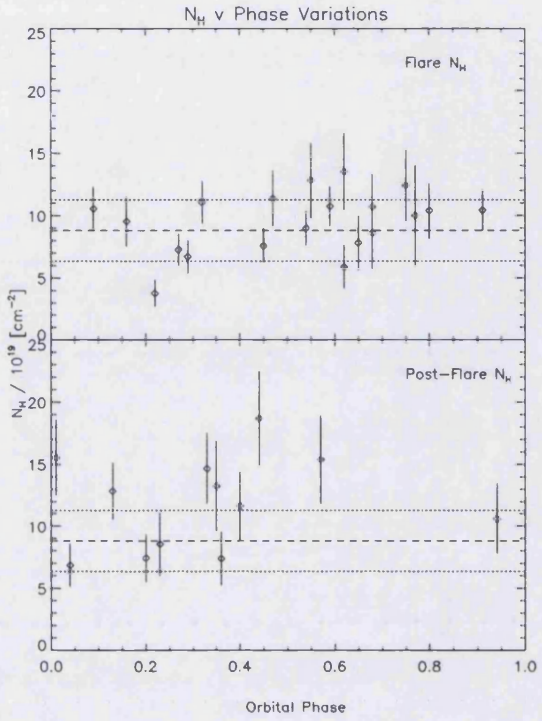

Figure 5.6: *Flare and post-flare variation of the hydrogen column density with phase are plotted. In both cases, the weighted mean hydrogen column density (for the whole observation) is denoted by dashed lines. Dotted lines indicate one-sigma errors.*

column-density value variations, particularly with regards to the higher value point at phase 0.44 (originating in spectrum N°· 31). Although examination of the corresponding Tables 4.3 and 4.2 reveal that this spectrum produced a relatively poor fit, other spectra with poorer fits (as judged by their χ^2_ν values) did not produce such large deviations in column density from the mean. To help determine the statistical significance of this apparent increase in column density, I employed the IDL hypothesis testing routine, RS_TEST, on

the flare and post-flare column density values. This IDL procedure performs a Wilcoxon rank-sum test on two sample populations, which tests the hypothesis that they both share the same mean of distribution at some significance level (in this case at the 0.05 significance level – see IDL on-line help and Walpole & Myers, 1985 for further details). For the flare and post-flare column density values, the IDL procedure returns a computed probability of 0.04, marginally less than the required 0.05 significance level. Therefore the hypothesis that the flare and post-flare column density remains the same may be rejected, and the increase in column density considered statistically significant.

As noted previously, when examining the phased PSPC lightcurves, the later cycles display an eclipse earlier in phase, which may be indicative of some possible extended post-flare coronal structure such as prominences or perhaps circumstellar material. The general increase in column density would certainly seem consistent with this scenario. An increasing amount of evidence in the literature already points to the existence of extended material analogous to solar prominences in these systems. Much of this work has been carried out in the optical regime, where, for instance, excess absorption in Hα has been interpreted as due to the presence of stellar prominences. This is true not only for RS CVns (e.g. Hall et al. 1990; Hall and Ramsey 1992) but also for other active stars including BY Dra systems (Barden et al.1985) and single active stars (e.g. Robinson and Collier-Cameron 1986; Collier-Cameron and Robinson 1989) where they have been interpreted as stellar coronal condensations of cooler neutral material, supported by magnetic field structures. These structures also seem to be quite commonplace in RS CVns as demonstrated by Hall and Ramsey's (small) sample, where eight out of ten systems displayed evidence of stable co-rotating prominence like material (1992). These stellar prominences have also been shown to be much larger than their solar coun-

terparts, with radial extents of several solar radii (e.g. $\sim 4R_\odot$ and $\sim 9R_\odot$ for the RS CVn system SS Boo and the active single star AB Dor respectively — Hall et al. 1990; Collier Cameron 1991) and thus would also be consistent with the height estimates for the CF Tucanæ coronal structures calculated in this chapter.

A crude estimate of the particle density within this extended material can be made, from the increase in column density, assuming this to be a local effect. The column density increase is defined as

$$\Delta N_{\rm H} = n_{\rm H_l} \times d_l,$$

where $\Delta N_{\rm H}$, $n_{\rm H_l}$, and d_l are the change in column density, local particle density and local column length respectively. The increase in the weighted mean column density of post-flare and flare portions of the observation is known from the values given above ($0.87 \times 10^{19} < \Delta N_{\rm H} < 3.2 \times 10^{19}{\rm cm}^{-2}$), and the length can be taken from the coronal height constraints previously calculated ($1.3R_\odot \lesssim H_C \lesssim 5.2R_\odot$). Thus particle densities of the order $10^7\,{\rm cm}^{-3}$–$10^9\,{\rm cm}^{-3}$ can be inferred. The higher of these two values borders the low end of the scale for solar prominences (e.g. Schmieder 1988). Obviously, this is a crude estimate and highly dependent on the assumed geometry (e.g. the much larger volume in the coronal structures), and density stratification of the suspected prominence material. With the recent launch of the next generation X-ray telescopes (Chandra and XMM-Newton) higher spectral/spatial resolution observations will be obtained. These will help provide more accurate density determinations, possibly via density sensitive line ratios.

5.1.1 Comparison With The Survey Observations

As mentioned in Section 4.1, Kürster and Dennerls analysed ROSAT All-Sky Survey PSPC data of CF Tucanæ (Kürster and Dennerl 1993). From unpub-

lished contemporaneous optical observations, they found an inclination of 64° for the system (in contrast to the previous 71° given by Strassmeier et al. 1988, 1993), suggesting even more of the K star is visible at eclipse. They also observed wave-like variations in their phased PSPC lightcurves of CF Tucanæ, with X-ray maximum occurring at $\phi = 0.8$. Owing to the lower inclination, they attributed these variations to rotational modulation as opposed to eclipses. They were able to model their phased lightcurve with a two-spot coronal model (on the more active K star) and this agreed well with near simultaneous Doppler images which they obtained showing a large spot group covering $0.7 \lesssim \phi \lesssim 0.95$. Their Doppler images are shown in Fig. 5.7.

Fig. 5.7 shows a large spot group around phase 0.75, which corresponds with the survey PSPC maximum. The pointed PSPC observation presented in this chapter, also reveal a maximum occuring near quadrature, especially in the hard-band (see Fig. 5.3). It is known that in the Solar case, sunspots are produced (constrained to certain latitude regions), disappear, and then new spot groups reappear in the proximity of the previous group, with certain longitudes being favoured. The longitudes where such active regions occur have become known as Active Longitude Belts (ALBs). If the wave-like variations in the phased lightcurve are due to rotational modulation induced by the presence of active regions, then this pointed observation, which reveals X-ray maximum near quadrature, (i.e. very close to that found for the survey observations) would seem to indicate the presence of an active longitude belt at this phase for CF Tucanæ. However, such an assertion is tentative at best and cannot solely be made on the basis of just two sets of observations. Further observations are obviously required for this system. However, note that recent studies are increasingly in favour of the existence of preferential longitudes for spot production, to explain the apparent longevity of prominence-like material as

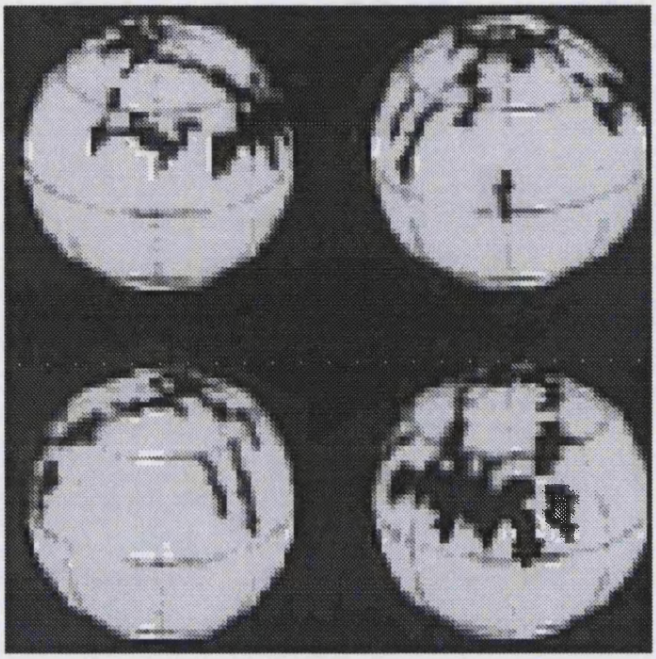

Figure 5.7: *Doppler images of CF Tucanæ from optical observations taken by Kürster and Dennerl. The four phases shown are: 0.0 (top left), 0.25 (top right), 0.5 (bottom left), 0.75 (bottom right). Contemporaneous ROSAT PSPC all-sky survey observations of CF Tucanæ (not shown) show an X-ray maximum occuring at* $\phi = 0.8$. *From Kürster and Dennerl, 1993.*

recurring features associated with the ALB (e.g. Rodonó et al. 1995).

5.2 A DISCUSSION OF KÜRSTER AND SCHMITT'S 1996 PAPER

As noted in section 4.1, the main motivation in analysing the archived ROSAT data of CF Tucanæ was to compare the observations with those of HR 5110. This was felt to be particularly important, as the CF Tucanæ observations

had only been published in conference proceedings. Soon after completion of this chapter, Kürster and Schmitt published a more detailed paper than the previous conference paper in which they analysed their data in more detail (Kürster and Schmitt 1996 – hereafter referred to as KS96).

The main findings of their paper are in agreement with those presented in this chapter (which is understandable since the same dataset is analysed). However a number of differences are present. As mentioned in section 5.1, any interpretation of the phased quiescent lightcurve is tentative due to the mainly incomplete orbital phase coverage. The authors of KS96 were in agreement with this and therefore refrained from presenting an orbital phased lightcurve analysis. However for areas where the analyses follow similar paths, namely the spectral and flare analysis, a comparison is now made to highlight and briefly discuss the differences present. (Note that KS96 does *not* include an analysis of the WFC data).

In both cases, a similar number of spectra were extracted (32 and 35 spectra for this Chapter and KS96 respectively) arising primarily as a consequence of the data gaps present in the observation. Naturally these spectra differed in the binning of the data and to a lesser extent to the different analysis packages used (ASTERIX plus XSPEC versus SASS and EXSASS).

In the KS96 spectral analysis of the data, the variety of component Raymond and Smith thermal plasma models explored by Kürster and Schmitt was mainly restricted to the following:

1. single temperature plasma models with a low metallicity abundance,
2. two-temperature plasma models with metallicity at the solar level, and
3. four-temperature plasma models with metallicity at the solar-abundance level.

Thus these authors restricted the number of free parameters to three or five, for the single and the multi-component models respectively.

The four-temperature fit models reported in KS96 however, differ from those used in this thesis in that they were only applied to the flare spectra. For these spectra, two of the temperature components were fixed at the mean values of the quiescent spectra (which were modelled with two-temperature component models), the other two components allowed to vary freely. This is discussed more fully in section 4.3.2, where it is suggested that the method employed in this thesis may be more applicable in the case of large flares (such as this one), as no assumptions are made about the underlying global quiescent emission with the "triggering" effect of large scale flaring. This assertion (that the method employed in this thesis is more favourable) may be justified by the fact that statistically better spectral fit results are reported in this thesis (as judged by the χ^2_ν values) than in KS96. [4]

---

[4]Comparison of the spectral results themselves between this thesis and KS96 can obviously be made for the two-temperature models, particularly with regards to the quiescent spectra. Similar values for both hot and cool component temperature and emission measures are obtained for those spectra which produced statistically reasonable results. The values from KS96 tend to be marginally higher with correspondingly lower values for the column density, than those presented in this thesis. As noted above however statistically better spectral fit results are reported in this thesis (as judged by the χ^2_ν values) than in KS96. Of the spectral fits reported in this thesis, 29/32 (91%) of the four-temperature model fits and 24/32 (75%) of the two-temperature model fits produced $\chi^2_\nu \lesssim 1.3$. In both cases the remaining fits produced $\chi^2_\nu \lesssim 1.5$. This can be contrasted with the spectral fit results reported in KS96 where only 14/35 (40%) of the multi-temperature model fits and 22/35 (63%) of the single-temperature model fits produced $\chi^2_\nu \lesssim 1.3$. For the KS96 paper, of the remaining spectral fits, only 9/21 and 3/11 produced $\chi^2_\nu \lesssim 1.5$ for the

In analysing the flare event itself, both the results presented in this chapter and those presented in KS96 are concluded similarly; namely that this flare can neither be described adequately by quasi-static cooling nor by standard Kopp and Poletto models. KS96 provide a much more detailed quasi-static cooling analysis, but the authors eschew the use of a light-curve decay analysis to derive minimum loop heights. Instead, they derived flare loop heights via the quasi-static analysis with results comparable to those calculated in this thesis. Note that Kürster and Schmitt employ different systemic parameters for CF Tucanæ than those given in section 4.1 (which were obtained from the Strassmeier et al. catalogue 1988;1992). Kürster and Schmitt's systemic parameters (from as yet unpublished optical data) give the following values: $R_G = 4.6R_\odot$, $R_K = 1.5R_\odot$, and inclination $\sim 64°$. The flare heights which these authors derived ($H = 2.8$—8.0×10^{11}cm) are *still* of the order of the binary separation and comparable to those presented in this chapter. Thus, my main resuts are not contested.

5.3 SUMMARY OF RESULTS FOR CF TUC

In this chapter the post-flare stage of the 1992 CF Tucanæ long duration flare event was examined. Although phase coverage was incomplete at most of the orbital cycles, the pointed WFC data indicated possible rotational modulation or eclipse in the EUV emission. This result (although tentative) is important as it adds to the very few WFC observations demonstrating this phenomen in RS CVns and is in contrast to what has been found in some other (non-RS CVn) active stars. Analysis of the phased post-flare PSPC data also re-

---

multi-temperature and single-temperature models respectively (the majority of fits producing $\chi^2_\nu \gtrsim 2$.

vealed variations in both the hard-band and soft-band lightcurves. However it is also possible that the variations may have been due to small flares (and therefore spurious) which combined with the poor orbital coverage could have given rise to the appearance of a depression in the phased lightcurve. By assuming that these variations were true and due to coronal eclipses as opposed to rotational modulation, the spatial extent of the corona was inferred, and found to be comparable with values previously found for other RS CVns. Variations in later orbital cycles seemed to indicate eclipses that were earlier in orbital phase. This indication combined with a slight statistically significant increase in the column density for the post-flare spectra, may indicate the presence of possible circumstellar or extended material in the system, resulting from the outburst. It is suggested that superflares may trigger post-flare prominence production. In the next chapter, the results from previous chapters will be reviewed and discussed in the light of results from contemporaneous work, and suggestions for future work will be made.

Chapter 6

A Final Discussion And Conclusions

And now,
The end is near,
And so I face,
The final curtain,...

"My Way", Paul Anka

6.1 A SUMMARY OF RESULTS

In this thesis I have reported the analyses of ROSAT observations of very large flare events on two RS CVn systems with similar binary separations. Although RS CVns are known to experience flaring activity which dwarfs that observed on the Sun, these observations have demonstrated energetics and

flare durations greater than is normally found even in these systems. The main hypothesis of this thesis is that these systems have experienced flaring of an inter-binary nature, and this chapter will now summarize the main results which have been found to support this, and suggest future avenues of research to further investigate this phenomenon.

6.1.1 Flare Lightcurve Characteristics

In chapters two and three of this thesis, I described observations of the RS CVn system HR 5110, and their analyses. The first observation, made in June 1991, provided a detailed look at this system with a 73 ks pointing lasting just over one orbital period. This gave a much higher signal-to-noise dataset than the follow-up observation (a 33 ks pointing), taken two years later, which produced snapshots of the system over a period of a month. Both observations, however, serendipitously revealed the system to be in extremely active states and are redisplayed in Fig. 6.1(a), where they have been overlaid (see below for details).

The most striking features of these observations were the two long-duration flare events (hereafter referred to as LDE's) which occurred on both occasions, and which lasted of the order of several days. In the 1991 observation, the initial rise of the LDE was missed and was already undergoing a state of decay, with the PSPC count-rate declining to half its initial value over three days. The almost continuous temporal coverage however, showed the decay to proceed smoothly with a steep decline, followed abruptly by a 'kink', wherafter the decline was more gradual, until a final observed PSPC count-rate, almost three times larger than the (presumably quiescent) all-sky survey value, was reached. The follow-up observation of June 1993 also revealed an LDE which was monitored over a period of seven and a half days and fortunately also included the peak of the event. After decaying to two-thirds of the peak

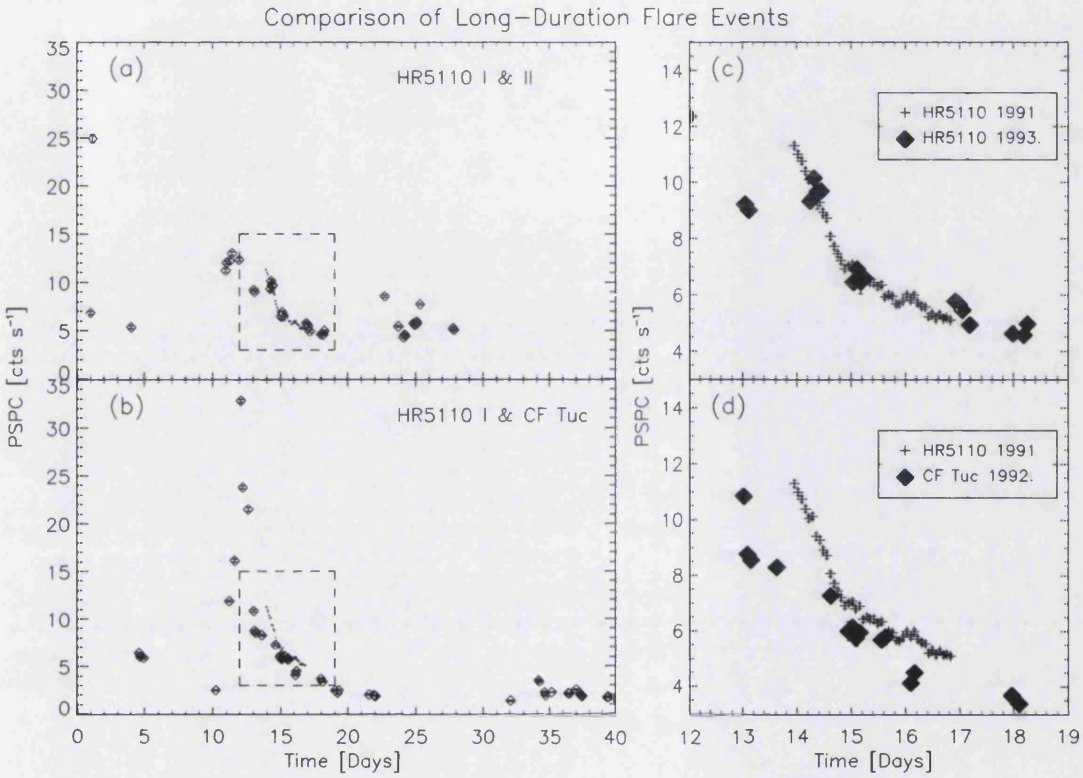

Figure 6.1: *A comparison of the June 1991 HR 5110 LDE lightcurve with those of the 1993 HR 5110 (a) and 1992 CF Tuc LDEs respectively (b). These display the complete June 1993 HR 5110 and October 1992 CF Tuc PSPC observations (denoted by the open diamond symbols) upon which the 1991 HR 5110 LDE (denoted by dots) has been overlayed (highlighted by the dash-lined square). The time-axis is given in units of days since the beginning of the 1993 observation and is purely arbitrary. Figs. (c,d): These show magnified views of the overlayed 1991 HR 5110 LDE with the 1993 HR 5110 and CF Tuc LDE lightcurves repectively: the 1991 HR 5110 LDE is denoted by plus-signs, and the both the 1993 HR 5110 and CF Tuc LDEs are denoted by filled diamonds. See text for details.*

count-rate (a period of three days) a second peak was observed after which the LDE continued to decay over approximately four days to a level comparable to the final count rate of the 1991 observation.

The 1993 LDE had been preceded by a high count-rate flare (although this was poorly monitored), and was followed by a couple of smaller count-rate flares with possible post-flare coronal enhancement. Aside from the obviously greater durations of the decay phase of the LDE flares (when compared with many other stellar flares previously reported in the literature), another notable difference is that of the lightcurve morphology of these events. In the 1993 observation, it is impossible to determine whether the second peak is part of the same LDE, after having undergone further reconnection for instance, or whether the second peak belongs to a separate flare, in which case the lightcurve is simply the resulting superposition of these two flare events. However, if one compares the 1993 LDE with the previous outburst, two years earlier, a similarity in the morphology of the two light-curves is evident and one could deduce that a similar event had occurred. This is demonstrated in Fig. 6.1(a) and (c).

In Fig. 6.1(a), I have plotted the June 1993 PSPC observation (with datapoints denoted by open diamond plotting symbols), against the number of days since the beginning of the observation. I then overlayed the June 1991 PSPC observation (denoted by dot plotting symbols. Error bars for these points were excluded so as not to clutter the diagram). The 1991 lightcurve was then shifted along the time-axis until the two decay curves coincided in terms of count-rate. Note that *no* vertical shift or scaling is applied to either of the lightcurves. These two overlaid decay curves are highlighted by the dash-lined square, and a magnified view presented in Fig. 6.1(c), where the 1993 lightcurve is denoted by filled diamonds (with no error bars to prevent clutter-

ing) and the 1991 lightcurve denoted by crosses (error bars are plotted but the errors are contained within the symbols). If one considers that these two decay curves are from two distinct flare events separated by a couple of years, one of which is a partial observation of the flare (albeit with good temporal resolution) and the other provides snapshots of the entire event, the similar decay profiles compare favourably.[5] This is highlighted further when contrasted with the 1991 HR 5110 and overlayed 1992 CF Tuc flare decay lightcurves plotted in Fig. 6.1(b). Like the HR 5110 follow-up observation, the CF Tuc observation provided snap-shots of the system covering a period of about a month. Unlike the observations of HR 5110, however the start and impulsive rise of the flare were well monitored, as was the flare decay, which progressed in two stages. From a high count-rate peak (over twice that of the 1993 HR 5110 LDE peak value) an initial rapid decline followed, lasting just over a day, until the count-rate was reduced by two-thirds. A more gradual decline then followed, lasting about seven days. Fig. 6.1(d) shows a magnified view of the dashed line square within Fig. 6.1(b) and reveals that both the rapid and gradual decay of the CF Tuc flare are steeper than those of the 1991 HR 5110 flare. Thus even though the decays follow a similar morphology (i.e. the flare decay comprises both a rapid followed by a more gradual decay), the two decay curves could not be adequately co-aligned as was the case for the two HR 5110 curves. This may arise from the fact that although CF Tuc and HR 5110 are systemically similar, they are not identical. If these LDE's are inter-binary in nature, any systemic differences (however slight) could affect the global magnetic field configuration of the two component stars, upon which such an outburst may be dependant.

---

[5] A reduced chi-squared test between these two decay curves gave a value of 1.3, indicating a reasonable agreement between the two decay curves.

6.1.2 Flare Analyses Results

Flare analyses of the three LDEs presented in this thesis produced similar conclusions, namely, that standard flare models, whether describing compact flares and employing quasi-static cooling or describing two-ribbon flares using Kopp and Poletto models, were statistically inadequate to describe the behaviour of the LDEs.

This is the first time that such departures from these standard flare models have been unambiguously identified, particularly with regard to the high signal-to-noise data of the 1991 HR 5110 observation and the well-monitored CF Tuc observation. Independently, Kürster and Schmitt (1996) reached similar conclusions about the CF Tuc observation. This in no way suggests that these models are invalid or no longer of use in other cases. Rather in these analyses, the behaviour of these LDEs cannot be satisfactorily described by such flare models. The need for further work into the modelling of these flares is strongly recommended and is discussed below in section 6.3. However another cause may be to blame. Although the lightcurve for the first flare observed on HR5110, displayed a very smooth decline (even when binned in 100s time bins the smooth decline was consistent with that dispayed when binned at the ROSAT orbital period) the poor fits to the Kopp and Poleto models may also be attributed to the need for finer time resolution. Particularly for the other flares, where interpretation of the flare lightcurve behaviour is to some extent dependent on the data gaps present, in which further flaring acitivity may have occured. Future renanalysis of these data may require to take this need in to effect.

Indications of continued heating during the flare decay (particularly conclusive for the 1991 HR 5110 observation via interpretation of the hardness ratio and the crude emission measure distribution plots) led to the amendment of

the Van den Oord light-curve decay analysis method used in this thesis, which enabled me to derive minimum loop heights for these LDEs. These were of the order of the binary separation for these long-duration events.

In order to obtain independent confirmation of these results I contacted Dr. Fabio Reale at Palermo University who has helped to develop a method to derive the length of flaring structures, independently of any heating during the flare decay. The methodology has recently been published for YOHKOH observations of Solar flares[6] (Reale et al. 1997) and more recently has been extended to include the relevant conversion factors required for ROSAT instruments (Reale & Micela 1998). Reale applied his method to the data reported in chapter 2, and also derived loop heights of the order of the surface separation for the 1991 HR 5110 LDE (Reale 1996) thus confirming the results presented in this thesis.

The existence of such large flaring coronal structures in RS CVn systems, larger than found on the Sun, appears consistent with the picture currently emerging of the RS CVn coronal environment. The greater coronal activity levels in these sytems, indicative of stronger magnetic fields strengths, combined with lower surface gravities, would allow larger magnetic structures to be produced. Thus even ordinary two-ribbon flares on RS CVns would exhibit dimensions and energies larger than found in the solar case, as can be seen from Table 1.1–1.4 of the introduction chapter.

---

[6]The method involves finding a relationship between the light curve decay time, and the slope in a density-temperature (n-T) diagram of the flare decay, by using hydrodynamic simulations of the decay of single flaring loops, and assumming various values for loop length and heating functions. From this relationship an expression of the loop length as a function of the light curve decay time and of the slope in the n-T diagram can be derived.

However, the greater extent of quiescent coronal structures within these systems, can present opportunities for interaction between these structures at the inter-binary level. As mentioned in chapter 1, eclipse modulation mapping of EXOSAT data of AR Lac suggested the existence of high-temperature, low-density structures of large extent (Schrijver 1985; White et al. 1987,1988). A more detailed approach has been applied by Preś et al. (1995) who used a 3D iterative deconvolution technique (again applied to EXOSAT LEIT and ME data) which helped them to model the soft X-ray emission distribution within the eclipsing system TY Pyx. In their analysis, the presence of interconnecting loops between the component stars of this system was strongly suggested. Similar analyses, this time performed on ASCA GIS observations of AR Lac, showed that the most probable model solutions of the data, pointed to interconnecting *quiescent* coronal structures (Siakowski et al. 1996) confirming the earlier results of Preś et al.

This scenario remains consistent with radio observations of RS CVns which have shown that emission from extended coronal structures, of comparable size to that of the whole binary system, are prevalent in RS CVn systems (e.g. Mutel 1985; Trigilio, Leto and Umana 1998). Further examples include the presence of intersystem thermal plasma suggested to explain the variablility observed in 6 cm quiescent observations of UX Ari through absorption (Wilson & Lang, 1987). Similarly, Lestrade's (1996) analysis of VLBI observations of the RS CVn systems UX Ari and σ CrB also strongly suggests that the source of quiescent radio emission is within the intra-binary region.

These radio observations are particularly relevant to the understanding of the X-ray results, because although the emission processes involved at radio and soft X-ray wavelengths are fundamentally different (involving non-thermal and thermal electron populations respectively), a number of studies

have demonstrated that these emissions appear correlated (e.g. Drake et al. 1989,1992; Güdel & Benz 1993;1994) and may in fact be co-spatial in origin (Franciosini & Chiuderi-Drago 1995). However, the exact relationship between these thermal and non-thermal populations of electrons has yet to be developed and further work is required in this field.

The stability of such large coronal structures has been investigated in a small number of theoretical studies. The most significant of these studies are those of Uchida and Sakurai (1983), who first explored this scenario and demonstrated that inter-linking loops between active regions on binary stars are feasible. Further investigation into the interaction between the magnetic fields of binary stars includes that of Vahia (1995) who showed that during rotation of the stars the magnetosphere of one star can envelop that of the other. Other work includes that by van den Oord (1988) who investigated the stability of filaments supported by magnetic structures interacting between the component stars of a binary system.

However, as yet no detailed modelling of inter-binary flares *per se* has been done. This seems to be an area which requires attention, particularly with the growing number of observations which are increasingly pointing to such phenomena, including those in this thesis. Furthermore, the studies of Uchida and Sakurai and that of Vahia, present simplified models of this scenario in which the magnetic fields are allowed to interact *in vacuo*. In reality the existence of an extended corona (demonstrated by the radio and X-ray observations) and inter-binary material (suggested by infra-red observations) would suggest plasma permeated by these magnetic fields. Any interaction would therefore involve more than just a change in the magnetic topology, but would also produce current sheets, which may help to power these flares as reconnection occurs. Thus, continued work in this area is required and further suggestions

will be outlined below in section 6.3.

6.1.3 Flare Spectral Characteristics

As was noted in chapter 2, analyses of the high signal-to-noise spectra extracted from the 1991 HR 5110 observation, demonstrated that multi-temperature thermal plasma models produced the best fits. All other attempted combinations of models proved statistically inadequate as judged by the χ^2_ν value. However one must keep in mind that the ROSAT PSPC is a broad-band instrument. Therefore in fitting multi-temperature models to ROSAT data one is constrained by the number of free parameters that can legitimately be used, owing to the low number of independent energy bins available to the PSPC (Saxton 1996). The multi-temperature models used in this thesis were restricted to just five free parameters by the number of independent energy bins at the 90In this way, the number of free parameters fitted remain the same as would be the case if standard two-temperature thermal plasma models plus an absorption component had been fitted. This is consistent with the method and choice of models used in fitting other high signal-to-noise ROSAT spectra reported in the literature, where multi-temperature models have been used (e.g. Jeffries 1992; Drake et al. 1994) and points to a more physically realistic multi-temperature plasma distribution within stellar coronal structures. A further constraint imposed on the choice of temperatures is that of the intrinsic temperature resolution limit, which is independent of the energy resolution of the instrument. This is discussed in Appendix A.

6.2 SPECTRAL RESULTS FROM CONTEMPORANEOUS OBSERVATIONS

The question of deriving valid spectral parameters is further complicated by recent ASCA and EUVE observations of RS CVns and active stars suggesting coronal metal abundances lower than found in the Sun by a factor 3–10 (Antunes et al. 1994; White et al. 1994; Drake et al. 1994; Singh et al. 1995; Schmitt et al. 1996). These authors have been able to model their spectra with the canonical two-temperature thermal plasma models, described in the introduction chapter, and varying the abundances for a large number of elements, (increasing the number of fitted parameters in the process). This is possible for both ASCA and EUVE spectra due to the greater spectral resolution available in comparison to that of ROSAT. One could therefore ask whether such sub-Solar abundances could be detected in ROSAT PSPC spectra. This issue has recently been addressed by Singh et al. (1996) and Bauer and Bregman (1996) who have shown that spectral models with sub-Solar abundances can provide reasonable statistical fits to PSPC spectra with typical integration times of a few kiloseconds or lower. However, derived temperatures and absorption columns values are then dependent on the assumed metallicity value, varying by as much as a factor 2 between solar and sub-solar abundance values reported in the literature (Bauer and Bregman 1996).

As reported previously, when analysing the PSPC spectra presented in Chapter 2, attempts at incorporating sub-Solar abundances in both single and two-temperature thermal plasma models were made. However, as mentioned in Chapter 2, aside from the best-fit models used in this thesis, *all* other combination of models yielded statistically poor fits with typical values of $\chi^2_\nu \gtrsim 2$.

How can the spectral results from this thesis (which uses multi-temperature plasma model with solar abundances) therefore be reconciled with those reporting sub-Solar abundances? The answer may lie in the fact that sub-Solar abundances derived from ASCA observations generally relate to quiescent coronal emission. The few ASCA observations which have observed both quiescent and flare emission, have reported significant elemental abundance increase (e.g. from 0.2 to 0.9 for Fe) during the flare rise (Linsky, Gudel, Nagase 1997; Mewe et al. 1997). Such large abundance variations could therefore account for this discrepency. Note also that for spectra of integration times comparable to those described in chapter 2, a multi-temperature source model can be reasonably fitted by a two-temperature thermal plasma model with sub-Solar abundances, and vice-versa (assuming the same source at the same count-rate — see Appendix A). Thus for spectra with low integration times, it would be impossible to determine uniquely both abundances and temperature stratification based on PSPC spectra alone.

6.3 FUTURE WORK

The ROSAT observations presented in this thesis provide important results from both HR 5110 and CF Tucanæ, detailing possible inter-binary flaring within these RS CVns systems. However to quantify and understand this flaring phenomenon more fully, further observations are required. The following section will briefly outline the types of observations required, future avenues of research to be investigated, and work which is currently being planned by the author.

As the two observation of HR 5110 suggest, similar outbursts may be quite common in this system. One cannot state with any certainty how frequently such events do occur without further observations. Some authors have sug-

gested that a large flare should occur in RS CVns systems once an orbital cycle (e.g. Ottmann and Schmitt 1994). However, as can be seen from the second HR 5110 observation and that of CF Tuc., (which monitored both these systems over a period of about a month) such a scenario appears to be a little over-optimistic, at least in these two cases. Thus further regular monitoring of RS CVn systems is required in order to improve our statistics of such large events.

Although, this should at the very least improve our knowledge of the statistics concerning these events, the need for higher energy resolution observations is evident from the earlier discussion. To this end, I proposed for, and was awarded observing time with the ASCA satellite (as part of the target of opportunity program). The ASCA window of opportunity to observe HR 5110 was between 15 June 1998 and 17 July 1998. This was coordinated with a planned multi-wavelength observing campaign which I organised with collaboraters in Italy and the United States. This programme involved optical monitoring of HR 5110 (including UBV photometry and H_α spectroscopy)[7], together with contemporaneous Infra-Red photometry and polarimetry[8] and radio monitoring[9] which would have helped to place constraints on the physical extent of the corona. These observations were to provide indications of any increases in activity levels, to trigger ASCA to start observations.

In addition to the flare analyses, the aim was to correlate any flare detections with spot locations (derived from the UBV light curve analysis) and to search for white light flares (e.g. Foing et al., 1994) should the system be in an

---

[7]Observations used the automatic 80 cm and 91 cm telescopes, at Catania Observatory

[8]IR Observations were made at the Turin Observatory

[9]Radio observations utilised telescopes at the VLBI station in Noto

active state when observations commenced. H_α spectroscopy (with a resolution of 0.44 Å) would have allowed detection of mass motion, from line profile features or asymmetry during any observed flares as has been found for some previous smaller flares (e.g. Catalano & Frasca, 1994). The H_α emission light curve would also have been used to infer the presence of surface structure at the chromospheric level, which, combined with the radio observations would have allowed any correlation of magnetic footpoints with the overlying coronal structure to be investigated (e.g. Umana et al. 1995). This in turn could have helped to constrain physical parameters derived from flare models.

If a flare outburst were to have occured, then ASCA target of opportunity observations would have provided high confidence measurements of the Fe K features near 6.7 keV and allowed investigation of the Fe complex near 2 keV. In addition to tracking possible Fe line changes and abundance variations (as a result of extended outbursts), comparison with ASCA data from other RS CVn systems could also have been made. Examination of the harder X-ray region (which is not possible with the ROSAT data) may also have helped to indicate where the emission measure distribution turns over.

Unfortunately, during the period of time when the observations were to be made, HR 5110 was in a very quiet state and no activity indications were evident (Trigilio 1998).

Such observations could have provided a stepping stone from the broad-band observations presented in this thesis to the more exciting results expected from new missions such as Chandra and XMM-Newton. The high energy and spatial resolution of the instruments aboard these satellites (e.g. $E/\Delta E$ approach the order of several hundreds, and spatial resolution $\lesssim 0.5$ arcsec) will provide observations approaching those that solar physicists have already come to expect at X-ray wavelengths. The ability to accurately derive coronal den-

sities from density sensitive line ratios, will provide also help provide definitive values for the flare volumes and geometric extents of such flare events, should an outburst as described in this thesis be observed.

Areas for further research include development of theoretical models, both to better describe the flare observations, and also to investigate the interaction of inter-binary coronal loops in conditions which reflect the physical environment more accurately, as mentioned above in section 6.1.2.

One way in which flare models, (such as Kopp and Poletto used to describe the lightcurve decay) could be improved, would be to compare the physical parameters derived from these models when fitted to high temporal resolution YOHKOH lightcurves of Solar flares for instance, with measurements gleaned from the corresponding high spatial resolution data. The range of observed departures from previously idealised models, could then be incorporated to better constrain these models.

A theoretical investigation of inter-binary flaring within RS CVn systems could be extended by considering how various systemic parameters affect the possibility of such an event. For instance could such a flare event initiate mass transfer in an RS CVn system filling a significant proportion of its Roche Lobe?[10] If so, then what constraints could be placed on the size of the flare and on the systemic parameters for such a trigger to be valid? What would then be the systemic environmental consequences if this were possible? For RS CVns with mass transfer occuring, how would an interbinary flare affect any on-going mass transfer process? If a transitory disk exists, then how would changes in the magnetic field configuration affect this or any circumstellar material and vice versa? What affect would this have on the stability of any

[10]Both HR 5110 and CF Tucanæ fill approximately 80% their Roche Lobes (Strassmeier et al. 1993)

disc/stream interaction? Such an investigation could therefore lead to a better understanding of the evolutionary consequences of this phenomenon.

6.4 A FINAL WORD

The observations presented in this thesis have added to the growing pool of evidence, which demonstrate that conditions within short-period RS CVns are indeed favourable for the production and support of the inter-binary flare phenomenon. Further insight into these Long Duration Flare events await higher spectral resolution observations with ASCA and future X-ray missions such as Chandra and XMM-Newton. The line diagnostic capabilities of these missions will further constrain physical parameters, such as electron densities and temperature structures within these flares. Combined with multi-wavelength observations these will help to clearly identify whether these outbursts are inter-binary in nature and help to produce a more accurate picture of the processes occurring in these events.

Chapter 7

Bibliography

Abbett, W. P., Beaver, M., Davids, B., Georgobiani, D., Rathbun, P., Stein, R. F., 1997. Astrophys. J. **480**, 395.

Agrawal, P. C., Riegler, G., White ,N. E., 1981. Mon. Not. R. Astr. Soc., **196**, 73.

Agrawal, P. C., Rao, A. R., Riegler, G., 1986. Mon. Not. R. Astr. Soc., **219**, 777.

Ambruster, C., Snyder, W. A., Wood, K. S., 1984. Astrophys. J., **284**, 270.

Antiochos, S. K., Noci, G., 1986. Astrophys. J. **301**, 440.

Antonopoulou, E., 1987. Astron. Astrophys. Suppl. Series, **68**, 521.

Antunes, A., Nagase, F., White, N. E., 1994. Astrophys. J. **436**, L83.

Ayres, T. R., Linsky, J. L., 1980. Astrophys. J., **241**, 279.

Basri, G. S., 1987. Astrophys. J.,**316**, 377.

Barstow, M. A., 1985. Space Sci. Rev., **40**, 35.

Barstow, M. A., 1994. priv. com.

Barstow, M. A., Pye, J. P., Bromage, G. E., Flemming, T. A., Guinan, E., 1992. In *Stellar Chromospheres, Coronæ and Winds.* CCP7 Workshop. Jeffery, C. S., Griffin, R. E. M., (eds.)

Barden, S. C., Nations, H. L., 1985. *Bull. A.A.S.*, **17**, 879.

Bastian, T. S., 1994. Space Sci. Rev., **68**, 261.

Batten, A. H., 1973. in *Binary and Multiple System of Stars.*

Bauer, F., Bregman, J. N., 1996. Astrophys. J. **457**, 382.

Belloni, T., Hasinger, G., Izzo, C., 1994. Astron. Astrophys., **283**, 1037.

Benz, A. O., Güdel, M., 1994. Astron. Astrophys., **285**, 621.

Bidelman, W. .P., MacConnel, D. J., 1973. Astron. J., **78**, 687.

Bopp, B. W., Evans, D. S., 1973. Mon. Not. R. Astr. Soc., **164**, 343.

Bopp, B. W., 1983. in *Activity in Red dwarf stars*, IAU coll. No. 71., p.363

Borghi, S., Chiuderi Drago, F., 1985. Astron. Astrophys., **143**, 226.

Branduardi-Raymont, G., Mason, K. O., Warwick, R. S., Carrera, F. J. C., Graffagnino, V. G., et. al., 1994. Mon. Not. R. Astr. Soc., **270**, 947.

Brickhouse, N. S., Drake, J. J., 2000. Rev. Mex. Astron. Astrophys., **9**, 24.

Brickhouse, N. S., Dupree, A. K., Edgar, R. J., Liedahl, D. A., Drake, S. A., White, N. E., Singh, K. P., 2000. Astrophys. J.. *preprint.*

Briel, U. G., Aschenbach, B., Hasinger, G., Hippmann, H., Pfeffermann, E., Predehl, P., Schmitt, J. H. M. M., Schwentker, O., Voges, W., Zimmermann, U., George, M., Snowden, S. L., Turner, T. J., David, L., Harnden Jr., F. R., Kearns, K. E., Zombeck, M. V., Barstow, M. A., Osborne, J. P., Pye, J. P., Watson, M., West, R. G., Willingale, R., 1996. ROSAT Users Handbook.

Brown, J. C., 1971. Solar Physics. **18**, 489.

Budding, E., 1985. Publ. Astron. Soc. Pac., **97**, 584.

Budding, E., Mclaughlin, E., 1987. Astrophys. Space Sci., **133**, 45.

Burnight, T. R, 1949. Phys. Rev. **76**, 165.

Busso, M., Scaltriti, F., Persi, P.,Roberto, M., Silvestro, G., 1987. MNRAS., **234**, 445.

Busso, M., Scaltriti, F., Origlia, L. Persi, P. Ferrari-Toniolo, M., 1988. Astron. Astrophys., **183**, 83.

Byrne, P. B., 1989. Solar Physics, **104**, 61.

Byrne, P. B., 1996. in IAU Symposium N° 176. Kluwer Academic publ. (Dordrecht)., Strassmeier, K. G., Linsky, J. L., (eds.) p.299.

Canfield, R. C., Cheng, C. C., Dere, K. P., Dulk, G. A., Mclean, D. J., Robinson, R. D. Jr., Schmahl, S. A., Schoolman, S. A., 1980. in *Solar Flares*, ed. Sturrock, P. A., p. 451.

Cannon, C. J., 1985. Astrophys. J., **289**, 363.

Canuto, V. M, Goldman, I., Mazzitelli, I., 1996. Astrophys. J., **473**,550.

Cash, W., Bowyer, S., Charles, P., Lampton, M., Garnure, G., Riegler, G., 1978. Astrophys. J., **223**, L21.

Catalano, S., Rodonó, M., 1967. Mem. Soc. Astr. Ital., **38**, 395.

Catalano, S., Rodonó, M., 1969. in *Non-periodic Phenomena in Variable Stars* ed. Detre, L., p. 435.

Catalano, S., Rodonó, M., 1974. Mem. Soc. Astr. Ital., **38**, 395.

Catalano, S., 1990. in *Active Close Binaries*, Proceedings of the A.S.I. N° 319, p.347. Kluwar Academic Publ.

Catalano, S., Frasca, A., 1994. Astron. Astrophys., **287**, 575.

Catura, R. C., Acton, L. W., Johnson H. M., 1975. Astrophys. J., **196**, L47.

Charles, P., Walter, F., Bowyer, S., 1979. Nature, **282**, 691.

Charles, P. A., 1983. in *Activity in Red Dwarf Stars* IAU. Coll. N°. 71, p.415, eds. Byrne, P. B. & Rodonó, M., publ. Reidel, Dordrecht.

Chisari, D., Lacona, G. 1965. Mem. Soc. Astr. Ital., **36**, 433.

Ciaravella, A., Peres, G., Maggio, A., Serio, S., 1995. Astron. Astrophys. In 9^{th} Cambridge Workshop on Cool Stars, Stellar Systems and the Sun, Pallavicini, R., Dupree, A. K.,eds. p.257.

Collier Cameron, A., 1988. Mon. Not. R. Ast. Soc, **233**, 235.

Collier Cameron, A., Hearnshaw, J. B., Austin, R. R. D., 1981. Mon. Not. R. Ast. Soc, **197**, 769.

Collier Cameron, A., Bedford, D. K., Ricinski, S. M., Vilhu, O., White, N. E., 1988. Mon. Not. R. Ast. Soc, **231**, 131.

Collier Cameron, A., Robinson, R. D., 1989. Mon. Not. R. Ast. Soc, **236**, 57.

Collier Cameron, A., Woods, J. A., 1992. Mon. Not. R. Ast. Soc, **258**, 360.

Conti, P. S., 1967. Astrophys. J., **149**, 629

Covino, S., Tagliaferri, G., Pallavicini, R., Mewe, R., Poretti, E., 2000. Astron. Astrophys., **355**, 681.

Craig, I. J. D., 1981. In *Solar flare magnetohydrodynamics*, ed. Priest, E. R., p.286.

Craig, I. J. D., Brown, J. C., 1986. *Inverse Problems in Astronomy*, publ. Adam Hilger Ltd, Bristol.

Craig, I. J. D., McClymont, A. N., Underwood, J. H., 1978. Astron. Astrophys., **70**, 1.

Cully, S. L., Fisher, G. H., Abbott, M. J., Siegmund, O. H. W., 1994. Astrophys. J., **435**, 449.

Demircan, O., 1987. Astrophys. S. S., **136**, 201.

Dempsey, R. C., Linsky, J. L., Fleming, T. A., Schmitt, J. H. M. M., 1993a. Astrophys. J. Suppl. Series, **86**, 599.

Dempsey, R. C., Linsky, J. L., Schmitt, J. H. M. M., Fleming, T. A., 1993b. Astrophys. J., **413**, 333.

Donati, J. -F., Semel, M., Rees, D. E., Taylor, K., Robinson, R. D., 1990. Astron. Astrophys., **232**, L1.

Doyle, J. G., Butler, C. J., Byrne, P. B., Rodonó, M., Swank, J., Fowles, W., 1989. Astron. Astrophys., **223**, 219.

Doyle, J. G., Kellett, B. J., Byrne, P. B., Avgoloupis, S., Mavridis, L. N., Seiradakis, J. H., Bromage, G. E., Tsuru, T., Makishima, K., M^{c}Hardy, I. M., 1991. Mon. Not. R. Astr. Soc., **248**, 503.

Doyle, J. G., Kellett, B. J., Butler, C. J., Byrne, P. B., Neff, J. E., Brown, A., Fox, D., Linsky, J. E., Bromage, G. E., Avgoloupis, S., Mavridis, L. N., Seiradakis, J. H., Mathiouakis, M., Murphey, H. M., Krzesinski, J., Pajdosz, G., Dadonas, V., Sperauskas, J., van Wyk, F., Marang, F., Olah, K., Collier Cameron, A., Antonopoulou, E., Rovithis, P., Rovithis-Livaniou, H. 1992a. Astron. Astrophys. Suppl. Ser., **96**, 351.

Doyle, J. G., Van den Oord, G. H. J., Kellett, B. J., 1992b. Astron. Astrophys., **262**, 533.

Drake, J. J., 1998. Astrophys. J., **496**, L33.

Drake, S. A., Simon, T., Linsky, J. L., 1989. Astrophys. J. Suppl. Series, **71**, 905.

Drake, S. A., Simon, T., Linsky, J. L., 1992. Astrophys. J. Suppl. Series, **82**, 311.

Drake, S. A., White, N. E., Smale, A. P., Angelini, L., Marshall, F. E., Pravdo, S. H., 1994. *The Proceedings of the* 1st *Annual ROSAT Science Symposium and Data Analysis Workshop.*

Drake, S. A., Singh, K. P., White, N. E., Simon, T., 1994. Astrophys. J., **436**, L87.

Drake, S. A., Singh, K. P., White, N. E., 1996. in IAU Coll. 152, "Astrophysics in the Extreme Ultraviolet", ed. Bowyer, S., Malina, R. F. (Kluwer publ.) p.147.

Dupree, E., Brickhouse, N. S., Doscheck, G. A., Green, J. C., Raymond, J. C., 1993. Astrophys. J., **418**, L41.

Eaton, J. A., Hall, D. S., 1979. Astrophys. J., **227**, 907.

Eaton, J. A., Henry, G. W., Bell, C., Okorogu, A. 1993. Astron. J., **106**, 1181.

Eker, Z., Doherty, L. R., 1987. Mon. Not. R. Astr. Soc., **228**, 869.

Eker, Z., 1994. Astrophys. J., **445**, 526.

Endl, M., Strassmeier, K. G., Kürster, M., 1997. Astron. Astrophys., **328**, 565.

Favata, F., Schmitt, J. H. M. M., 1999. Astron. Astrophys., **350**, 900.

Feldman, P. A., Taylor, A. R., Gregory, P. C., Seaquist, E. R., Balonek, T. J., Cohen, N. L., 1978. Astron. J., **83**, 1471.

Feldman, P. A., 1979. I.A.U. Circ. N°. 3366

Feldman, P. A., 1983. in *Activity in Red Dwarf Stars* I.A.U. Coll. N°. **71**, p.429, eds. Byrne, P. B., Rodonó, M., publ. Reidel,Dordrecht.

Fekel, F. C., Moffett, T., J., Henry, G. W., 1986. Astrophys. J. Suppl. Series, **60**, 551.

Feldman, U., Widing, K. G., 1990. Astrophys. J., **363**, 292.

Foing, B. H., et al. 1994. Astron. Astrophys., **292**, 543.

Fox, D. C., Linsky, J. L., Veale, A., Dempsey, R. C., Brown, A., Neff, J. E., Pagano, I., Rodonó, M., Bromage, G. E., Kürster, M., Schmitt, J. H. M. M., 1994 Astron. Astrophys., **284**, 91.

Franciosini, E., Chiuderi-Drago, F., 1995. Astron. Astrophys., **297**, 535.

Friedman, H., 1960. Astron. J.**65** 264.

Gaetz, T. J., Salpeter, E. E., 1983. Astrophys. J. Suppl. Series, **52**, 155.

Gehrels, N., Williams, E. D., 1993. Astrophys. J, **418**, L25.

Giacconi, R., Gursky, H., Paolini, F., Rossi, B., 1962. Phys. Rev. Lett. **9**, 439.

Giampapa, M. S., Golub, L., Peres, G., Serio, S., Vaiana, G. S., 1985. Astrophys. J, **289**, 203.

Graffagnino, V. G., Wonnacott, D., Schaeidt, S., 1995. Mon. Not. R. Astr. Soc., **275**, 129.

Gratton, L., 1950. Astrophys. J., **111**, 31.

Griffiths, N. W., Jordan, C., 1998. Astrophys. J., **497**, 883.

Güdel, M., Benz, A. O., 1993. Astrophys. J., **405**, L63.

Güdel, M., Benz, A. O., 1994. Astron. Astrophys., **285**, 621.

Güdel, M., Linsky, J. L., Brown, A., Nagse, F. 1999. Astrophys. J., **511**, 405.

Gursky, H., Giacconi, R., Paolini, F., 1963. Phys. Rev. Lett. **11**, 530.

Haisch, B. M., 1983. in *Activity in Red-Dwarf Stars*, ed. Byrne, P. B., Rodonó, M., publ. Reidel, Dordrecht, p.255.

Haisch, B. M., 1989. Astron. Astrophys., **219**, 317.

Haisch, B. M., Strong, K. T., Rodonó, M., 1991. Ann. Rev. Astron. Astrophys., **29**, 275.

Hall, D., S., 1972. Publ. Astron. Soc. Pac., **84**, 323.

Hall, D. S., 1976. In *Multiple Periodic Variable Stars*, p. 287. ed. Fitch, W. S., publ. Reidel, Dordrecht.

Hall, D. S., Henry, G. W., Vaucher, C. A., Louth, H., Lovell, L. P., Landis, H. J., Brooks, P., Schlegel, R., Wasatonic, R., 1978. I.B.V.S. N°. 1459

Hall, D. S., Kreiner, J. K., 1980. Acta Astronomica, **68**, 521.

Hall, D. S., 1989. I.A.U. Colloquium. **107**, 219.

Hall, J. C., Ramsey, L. W., 1992. Astron. J., **104**, 1942.

Hall, J. C., Ramsey, L. W., 1994. Astron. J., **107**, 1149.

Hameury,J. M., King, A. R., Latosa, J. P., 1986. Astron. Astrophys., **162**, 71.

Hearnshaw, J. B., & Oliver, J. P., 1977. I.B.V.S. N°. 1342.

Heise, J., Brinkman, A. C., Schrijver J., Mewe, R., Gronenschild, E. H. B. M., Den Boggende, A. J. F., Grindlay, J., 1975. Astrophys. J., **202**, L73.

Heise, J., 1988. Mem. Soc. Astr. Ital., **59**, 53.

Hearn, A. G., 1975. Astron. Astrophys., **40**, 355.

Henry, G. W., Eaton, J. A., Hamer, J., Hall, D. S., 1995. Astrophys. J. Suppl. Series, **97**, 513.

Hiltner, W. A., 1947. Astrophys. J., **166**, 481.

Himpel, K., 1936. Astr. Nach., **261**, 233.

Hjellming, R. M., Gibson, D. M., 1980. in *Radio Physics of the Sun*, ed. Kundu, M. R., Gehrels, T. E., 209.

Holt, S. S., Boldt, E. A., Serlemitsos, P. J., White, N. E., Becker, R. H., Mushotzky, R. F., Smith, B. W., 1979. Astrophys. J., **234**, 65.

Hudson, H. S., Canfield, R. C., Kane, S. R., 1978. Solar Physics, **60**, 137.

Huenemoerder, P. P., 1985. Astron. J., **90**, 499.

Huenemoerder, D. P., Ramsey, L. W., Buzasi, D. L., 1990 Astrophys. J., **350**, 763.

Huenemoerder, D. P., Schulz, N. S., Canizares, C. R., Buzasi, D. L., 2000. AAS.,**196**, 3706.

Iben, I., 1989. I.A.U. Colloquium. **114**, 477.

Iben, I., 1991. Astrophys. J. Suppl. Series, **76**, 55.

Jeffries, H., 1961. in *Theory of Probability.* 3rd ed., Clarendon Press, Oxford p. 105. Eq. 10.

Jeffries, R. D., Bedford, D. K., 1990. Mon. Not. R. astr. Soc., **246**, 337.

Jeffries, R. D., 1992. In *Stellar Chromospheres, Coronæ and Winds.* CCP7 Workshop. Jeffery, C. S., Griffin, R. E. M., (eds.)

Jeffries, R. D., 1998. Mon. Not. R. Astr. Soc., **295**, 825.

Jenkins, L. F., 1963. General Catalogue of Trigonometric Stellar Parallaxes. (Yale University Observatory, New Haven).

Jordan, S., Wolff, B., Koester, D., Napiwotzki, R., 1994. Astron. Astrophys., **290**, 834.

Joy, A. H., Humason, M. L., 1949. Publ. Astron. Soc. Pac., **61**, 133.

Kellett, B. J., 1997. priv. comm.

Kron, G. E., 1947. Publ. Astron. Soc. Pac., **59**, 261.

Kuijpers, J., van der Hulst, J. M., 1985. Astron. Astrophys., **149**, 343.

Kopp, R. A., Pneuman, G. W., 1976. Solar Physics, **50**, 85.

Kopp, R. A., Poletto, G., 1984. Solar Physics, **93**, 351.

Kraft, R. P., Burrows, D. N., Nousek, J. A., 1990. Astrophys. J., **374**, 344.

Kuijpers, J., van der Hulst, J. M., 1985. Astron. Astrophys., **149**, 343.

Kürster, M., Dennerl, K., 1993. in *Physics of Solar and Stellar Coronæ: G. S. Vaiana Memorial Symposium.*, ed. Linsky, J. L., Serio, S., Kluwer Academic Publ., Dordrecht, p.443.

Kürster, M., 1995. The Proceedings of the 8th Cambridge Workshop on Cool Stars, Stellar Systems, and the Sun. p.104.

Kürster, M., Schmitt, J. H. M. M., 1996. Astron. Astrophys., **311**, 317.

Landini, M., Monsignori Fossi, B. C., 1972. Astron. Astrophys. Suppl. Ser., **7**, 291.

Landini, M., Monsignori Fossi, B. C., 1973. Astron. Astrophys., **25**, 9.

Landini, M., Monsignori Fossi, B. C., Paresce, F., Stern, R. A., 1985. Astrophys. J., **289**, 709.

Lanza, A. F., Catalano, S., Cutispoto, G., Pagano, I., Rodonó, M., 1998. Astron.. Astrophys., **332**, 541.

Lestrade, J. F., Mutel, R. L., Preston, R. A., Phillips, R. B., 1988. Astrophys. J., **328**, 232.

Linsky, J. L., Ayres, T. R., Basri, G. S., Morrison, N. D., Schiffer III, F. H., Holm, A., Cassatella, A., Heck, A., Macchetto, F., Stickland, D., Wilson, R., Blanco, C., Dupree, A. K., Jordan, C., Wing, R. F., 1978. Nature, **275**, 389.

Linsky, J. L., 1984. In 3^{rd} Cambridge Workshop on Cool Stars, Stellar Systems and the Sun, p.244., Baliunas, S. L., Hartmann, L. W. (eds.)

Linsky, J. L., 1985. Solar Physics **100**, 333.

Linsky, J. L., Gudel, M., Nagase, F., 1997. *Bull. A.A.S.*, **191**, 4412

Little-Marenin, I. R., Simon, T., Ayres, T. R., Cohen, N. L., Feldman, P. A., Linsky, J. L., Little, S. J., Lyons, R., 1986. Astrophys. J., **303**, 780

Maggio, A., Sciortino, S., Vaiana, G. S., Majer, P., Bookbinder, J., Golub, L., Harnden Jr., F. R., Rosner, R., 1987. Astrophys. J., **315**, 687.

Maggio, A., Peres, G., 1995. Astron. Astrophys. **306**, 563.

Majer, P., Schmitt, J. H. M. M., Golub, L., Harnden Jr., F. R., Rosner, R., 1986. Astrophys. J., **300**, 360.

Mewe, R., 1972. Astron. Astrophys., **20**, 215.

Mewe, R., Heise, J., Gronenschild, E. H. B. M., Brinkman, A. C., Schrijver J., Den Boggende, A. J. F., 1975. Astrophys. J., **202**, L67.

Mewe, R., Gronenschild, E. H. B. M., Van den Oord, G. H. J., 1985. Astron. Astrophys. Suppl. Ser., **62**, 197.

Mewe, R., Schrijver, C. J., 1986. Astron. Astrophys., **169**, 178.

Mewe, R., 1991. Astron. Astrophys. Rev., **3**, 127.

Mewe, R., Kaastra, J. S., Schrijver, C. J., Van Den Oord, G. H. J, Alkemade, F. J. M., 1995. Astron. Astrophys., **296**, 477.

Mewe, R., Kaastra, J. S., Van Den Oord, G. H. J., Vink, J., Tawara, Y., 1997. Astron. Astrophys., **320**, 147.

Milano, L., Russo, G., Mancuso, S. 1983. in Activity in Red-Dwarf Stars, ed. Byrne, P. B., Rodonó, M., publ. Reidel, Dordrecht, p.393.

Mitrou, C. K., Doyle, J. G., Mathioudakis, M., Antonopoulou, E., 1996. In 2nd Hellenic Astron. Conf. Proc., p.301. Contadakis, M. E., Hadjidemetriou, J. D., Mavridis, L. N., Seiradakis, J. H., (eds.)

Moore, R., McKenzie, D. L., Svestka, Z., et al. 1980. in Solar Flares, ed. Sturrock, P. A., publ. Colorado Assoc. Univ. Press, Boulder, CO.

Moss, D., 1986. Phys. Rep., **140**, 1.

Mukai, K., 1993. Legacy, **3**, 21.

Mutel, R. L., Lestrade, J. F., 1985. Astron. J., **90**, 493.

Mutel, R. L., Lestrade, J. F., Preston, R. A., Phillips, R. B., 1985. Astrophys. J., **289**, 262.

Mutel, R. L., Su, B., 1990. Astrophys. J., **362**, 299.

Napiwotzki, R., Barstow, M. A., Flemming, T., Holweger, H., Jordan, S., Werner, K., 1993. Astron. Astrophys., **278**, 478.

Neff, J. E., Pagano, I., Rodonó, M., Brown, A., Dempsey, R. C., Fox, D., Linsky, J. E. 1996. Astron. Astrophys., **310**, 173.

Noyes, R. W., Hartmann, L. W., Baliunas, S. L., Duncan, D. K., Vaughan, A. H., 1984. Astrophys. J., **279**, 763.

Osten, R. A., Ayres, T. R., Brown, A., Huenemoerder, D., Drake, J. J., Linsky, J. L., Brickhouse, N., 1999. A.A.S., **195**, 11214.

Ottmann, R., 1993. Astron. Astrophys., **273**, 546.

Ottmann, R., Schmitt, J. H. M. M., Kürster, M., 1993. Astrophys. J., **413**, 710.

Ottmann, R., 1994. Astron. Astrophys., **286**, L27.

Ottmann, R., Schmitt, J. H. M. M., 1994. Astron. Astrophys., **283**, 871.

Ottmann, R., Schmitt, J. H. M. M., 1996. Astron. Astrophys., **307**, 813.

Ottmann, R., Pfeiffer, M. J., Gehren, T., 1998. Astron. Astrophys., **338**, 661.

Owen, F. N., Jones, T. W., Gibson, D. M., 1976. Astrophys. J., **210**, L27.

Owen, F. N., Gibson, D. M., 1978. Astron. J., **83**, 1488. .

Pallavicini, R., Golub, L., Rosner, R., Vaiana, G. S., 1981. Astrophys. J., **248**, 279.

Pallavicini, R., Tagliaferri, G., Stella, L., 1990. Astron. Astrophys., **228**, 403.

Paresce, F., 1984. Astron. J., **89**, 1022.

Pasquini, L., Schmitt, J. H. M. M., Pallavicini, R., 1989. Astron. Astrophys., **226**, 225.

Pettersen, B. R., 1989. Solar Physics, **104**, 299.

Pneuman, G. W., 1982. In *Solar flare magnetohydrodynamics*, ed. Priest, E. R., p.414.

Poe, C. H, Eaton, J. A., 1985. Astrophys. J., **289**, 644.

Poletto, G., Pallavicini, R., Kopp, R. A., 1988. Astron. Astrophys., **201**, 93.

Poletto, G., 1989. Solar Physics, **121**, 313.

Pounds, K. A., et al., 1993. Mon. Not. R. Astr. Soc., **260**, 77.

Popper, D. M, 1970. Astrophys. J., **162**, 925.

Popper, D. M, Ulrich, R. K., 1977. Astrophys. J., **212**, L131.

Press, H. W., Flannery, B. P., Teukolsky, S. A., Vetterling, W. T., 1992. Numerical Recipes. Cambridge Univ. Press.

Prés, P., Siarkowski, M., Sylwester, J., 1995. Mon. Not. R. Astr. Soc., **275**, 43.

Priest, E. R. (ed.), 1981. *Solar Flare Magnetohydrodynamics*

Ramsey, L. W., Nations, H. L., 1980. Astrophys. J., **239**, L121.

Rangarajan, T. N., Verma, R. P., 1983. Mon. Not. R. Astr. Soc., **203**, 1035.

Raymond, J. C., Smith, B. W., 1977. Astrophys. J. Suppl. Series, **35**, 419.

Raymond, J. C., 1979., in *The Solar Transition Region*, by Mariska, J. T. p.38.

Raymond, J. C., 1988. in *Hot, Thin Plasmas in Astrophysics*, ed. Pallavicini, R., p.3.

Reale, F., Peres, G., Serio, S., Rosner, R., Schmitt, J. H. M. M., 1988. Astrophys. J., **328**, 256.

Reale, F., Betta, R., Peres, G., Serio, S., McTiernan, J., 1997. Astron. Astrophys., **325**, 782.

Reale, F., 1996. priv. comm.

Rengarajan, T. N., Verma, R. P., 1983. Mon. Not. R. Astr. Soc., **203**, 1035.

Richards, M. T., Albright, G. E., 1993. Astrophys. J. Suppl. Series, **88**, 199.

Robinson, R. D., Collier Cameron, A., 1986. Proc. Astron. Soc. Aus.**6**, 308.

Rodonó, M., Cutispoto, G., Pazzani, V., Catalano, S., Byrne, P. B., Doyle, J. G., Butler, C. J., Andrews, A. D., Blanco, C., Marilli, E., Linsky, J. L., Scaltriti, F., Busso, M., Cellino, A., Hopkins, J. L., Okkazaki, A., Hayyashi, S. S., Zeilik, M., Helston, R., Henson, G., Smith, P., Simon, T., 1986. Astron. Astrophys. **165**, 135.

Rodonó, M., Byrne, P. B., Neff, J. E., Linsky, J. L., Simon, T., Butler, C. J., Catalano, S., Cutispoto, G., Doyle, J. G., Andrews, A. D., Gibson, D. M., 1987. Astron. Astrophys. **226**, 225.

Rodonó, M., 1992. in *Evolutionary Processes in Interacting Binary Stars*, ed. Kondo, Y., p.71.

Rodonó, M., Lanza, A. F., Catalano, S., 1995. Astron. Astrophys. **301**, 75.

Rodonó, M., Pagano, I., Leto, G., Walter, F., Catalano, S., Cutispoto, G., Umana, G., 1999. Astron. Astrophys., **346**, 811.

Rosner, R., Tucker, W. H., Vaiana, G., S., 1978. Astrophys. J., **220**, 643.

Saar, S., Linsky, J. L., 1985. Astrophys. J., **299**, L47.

Saar, S., et al. 1987. in 27th Liege Int. Astrophys. Coll.

Saxton, R., D., 1991. Starlink User Note 98, Starlink Software Collection.

Saxton, R., D., 1991. Starlink User Note 005, Starlink Software Collection.

Scaltriti, F., Busso, M., Persi, P., Origlia, L., Robberto, M., Silvestro, G., 1987. in the 5th Cambridge Workshop on Cool Stars, Stellar Systems and the Sun, p.188.

Scaltriti, F., Piirola, V., Coyne, G. V., Koch, R. H., Elias, N. M., Holenstein, B. D., 1993a, Astron. Astrophys. Suppl. Ser. **102**, 343.

Scaltriti, F., Busso, M., Ferrari-Toniolo, M., Origlia, L., Persi, P., Robberto, M., Silvestro, G., 1993b. Mon. Not. R. Astr. Soc. **264**, 5.

Schaedt, S., 1993. priv. com.

Schmieder, B., 1988. Astron. Astrophys. **197**, 281.

Schmitt, J. H. M. M., Golub, L., Harnden Jr., F. R, Maxson, C. W., Rosner, R., Vaiana, G. S., 1985. Astrophys. J., **290**, 307.

Schmitt, J. H. M. M., Pallavicini, R., Monsignori-Fossi, B. C., Harnden Jr., F. R., 1987. Astron. Astrophys., **179**, 193.

Schmitt, J. H. M. M., Collura, A., Sciortino, S., Vaiana, G. S., Harnden Jr., F. R., JR., Rosner, R., 1990. Astrophys. J., **365**, 704.

Schmitt, J. H. M. M., 1994. Astrophys. J. Suppl. Series, **90**, 735.

Schmitt, J. H. M. M., Stern, R. A., Drake, J. J., Kürster, M., 1996. Astrophys. J.,**464**, 898.

Schrijver, C. J., 1985. Space Sci. Rev., **40**, 3.

Schrijver, C. J., Lemen, J. R., Mewe, R., 1989. Astrophys. J., **341**, 484.

Schrijver, C. J., Zwaan, C., 1991. Astron. Astrophys., **251**, 183.

Serio, S., Peres, G., Vaiana, G. S., 1981. Astrophys. J., **243**, 288.

Shafer, R. A., Haberl, F., Arnaud, K. A., Tennant, A. F., 1993. XSPEC Users Guide.

Shüssler, M., Solanki, S. K., 1992. Astron. Astrophys. **264**, L13.

Siarkowski, M., Prés, P., Drake, S. A., White, N. E., Singh, K. P., 1996. Astrophys. J. **473**, 470.

Simon, T., Linsky, J. L., 1980. Astrophys. J., **241**, 759.

Simon, T., Linsky, J. L., Schiffer, F. H. III, 1980. In *The Universe at Ultraviolet Wavelengths*, p.435, ed. Chapman, R. D., NASA Conference Publ. N°. 2171.

Simon, T., Linsky, J. L., Schiffer, F. H. III, 1980. Astrophys. J., **239**, 911.

Singh, K. P., Drake, S. A., White, N. E., 1995. Astophys. J., **445**, 840.

Slettebak, A., 1955. Astrophys. J., **121**, 653.

Spitzer, L., 1962. *The Physics of Fully Ionized Gases*

Stern, R. A., Uchida, Y., Tsuneta, S., Nagase, F., 1992a. Astophys. J., **400**, 321.

Stern, R. A., Uchida, Y., Walter, F., Vilhu, O., Hannikainen, D., Brown, A., Veale, A., Haisch, B. M., 1992b. Astophys. J., **391**, 760.

Strassmeier, K. G., Hall, D. S., Zeilik, M., Nelson, E., Eker, Z., Fekel, F. C., 1988. Astron. Astrophys. Suppl. Ser., **72**, 291.

Strassmeier, K. G., Rice, J. B., Wehlau, W. H., Vogt, S. S., Hatzes, A. P., Tuominen, I., Hackman, T., Poutanen, M., Piskunov, N. E., 1991. Astron. Astrophys., **247**, 130.

Strassmeier, K. G., Hall, D. S., Fekel, F. C., Scheck, M., 1993. Astron. Astrophys. Suppl. Ser., **100**, 173.

Strohmeier, W., Knigge, R., & Ott, H., 1965. I.B.V.S. N°. 100.

Sturrock, P., 1968. in *Structure and Development of Solar Active Regions: I.A.U. Symposium N° 35.*, ed. Kiepenheuer, K. O., p.471.

Swank, J. H., White, N. E., Holt, S. S., Becker, R. H., 1981. Astrophys. J., **246**, 208.

Tagliaferri ,G., White, N. E., Doyle, J. G., Culhane, J. L., Hassall, B. J. M., Swank, J. H., 1991. Astron. Astrophys., **251**, 161.

Tagliaferri, G., Covino, S., Cutispoto, G., Pallavicini, R., 1999. Astron. Astrophys., **345**, 514.

Tandberg-Hanssen, E., Emslie, A. G., 1988. *The Physics of Solar Flares*

Tassoul, J. L., 1987. Astrophys. J., **322**, 856.

Tassoul, J. L., 1988. Astrophys. J., **324**, 71.

Tassoul, M., Tassoul, J. L., 1997. Astrophys. J., **481**, 363.

Thompson, K., Coates, D. W., Anders, G., 1991. Proc. Astron. Soc. Aus., **9**, 283.

Tout, C. A., Eggleton, P. P., 1989. Space Sci. Rev., **50**, 165.

Trigilio, C., 1998. Priv. Comm.

Trigilio, C., Leto, P., Umana, G., 1998. Astron. Astrophys., **330**, 1060.

Truemper, J. E. 1991. Sterne & Weltraum, **30**, 234.

Tsikoudi, V., Kellett, B. J., 1997. Mon. Not. R. Astr. Soc., **285**, 759.

Tsuneta, S., Hara, H., Shimizu, T., Acton, L. W., Strong, K. T., Hudsen, H. S.,Ogawara, Y., 1992. Publ. Astron. Soc. Japan, **44**, 63.

Tsuru, T., Makishima, K., Ohashi, T., Inoue, H., Koyama, K., Turner, M. J. L., Barstow, M. A., McHardy, I. M., Pye, J. P., Tsunemi, H., Kitamoto, S., Taylor, A. R., Nelson, R. F., 1989. Publ. Astron. Soc. Japan, **41**, 679.

Turner, T. J., George, I. M., 1993. ROSAT PSPC Calibration Guide, From USA ROSAT Science Data Center and HEASARC.

Uchida, Y., Sakurai, T., 1983., in *Activity in red-dwarf stars*, p.629.

Uchida, Y., Sakurai, T., 1985., in *Unstable Current Systems and Plasma instabilities in Astrophysics*, p.281.

Ulrich, R. K., Popper, D. M., 1974. *Bull. A.A.S.*, **6**, 461.

Umana, G.,Trigilio, C., Tumino, M., Catalano, S., Rodonó, M., 1995. Astron. Astrophys., **298**, 143.

Unruh, Y., Cameron, A. C., 1995. Mon. Not. R. Astr. Soc., **273**, 1.

Vahia, M., N., 1995. Astron. Astrophys., **300**, 158.

Vaiana, G., S., Cassinelli, J. P., Fabbiano, G., Giacconi, ,R., Golub, L., Gorenstein, P., Haisch, B. M., Harnden, Jr., F. R., Johnson, H. M., Linsky, J. L., Maxson, C. W., Mewe, R., Rosner, R., Seward, F., Topka, K., Zwaan, C., 1981. Astrophys. J., **245**, 163.

Van den Oord, G. H. J., 1988. Astron. Astrophys., **205**, 167.

Van den Oord, G. H. J., Mewe, R., Brinkman, A. C., 1988. Astron. Astrophys., **205**, 181.

Van den Oord, G. H. J., Mewe, R., 1989. Astron. Astrophys., **213**, 245.

Vesecky, J. F., Antiochos, S. K., Underwood, J. H., 1979. Astrophys. J., **233**, 987.

Viner M. R., Feldman, P. A., 1979. IAU Circular 3368.

Vogt, S. S., 1979. Publ. Astron. Soc. Pac., **91**, 616.

Vogt, S. S., 1981a. Astrophys. J., **247**, 975.

Vogt, S. S., 1981b. Astrophys. J., **250**, 327.

Vogt, S. S., 1983. in *Activity in Red-Dwarf Stars,* ed. Byrne, P. B., Rodonó, M., publ. Reidel, Dordrecht.

Vogt, S. S., Penrod, G. D., 1983. Publ. Astron. Soc. Pac., **95**, 565.

Vogt, S. S., Hatzes, A. P., Misch, A.. A, Kürster, M., 1999. Astron. Astrophys. Suppl. Series, **121**, 547.

von Steiger, R., Marsch, E., 1994. Space Sci. Rev., **70**, 341.

Walpole, R. E., Myers, R., H., 1985. *Probability and statistics for engineers and scientists* 3rd ed.

Walter, F. M., Charles, P., Bowyer, S., 1978. Astrophys. J., **225**, L119.

Walter, F. M., Cash, W., Charles, P. A., Bowyer, C. S., 1980. Astrophys. J., **236**, 212.

Walter, F. M., Bowyer, C. S., 1981. Astrophys. J., **245**, 671.

Walter, F. M., Gibson, D. M., Basri, G. S., 1983. Astrophys. J., **267**, 665.

Weiler, E. J., 1976. I.B.V.S. N°. 1212.

Weiler, E. J., 1978. Mon. Not. R. Astr. Soc., **182**, 77.

Weiler, E. J., Owen, F. N., Bopp, B. W., Schmidtz, M., Hall, D. S., Fraquelli, D. A., Piirola, V., Ryle, M., Gibson, D. M., 1978. Astrophys. J., **225**, 919.

Weiss, N. O., 1993. in *Physics of Solar and Stellar Coronae*, ed. J. F. Linsky and S. Serio, Kluwer Academic Publishers, p.541.

White, N. E., Sandford, P. W., Weiler, E. J., 1978. Nature, **274**, 569.

White, N. E., Holt, S. S., Becker, R. H., Boldt, E. A., Serlimitsos, P. J., 1980. Astrophys. J., **239**, L69.

White, N. E., Culhane, J. L., Parmar, A. N., Kellett, B., Kahn, S., Van den Oord, G. H. J., Kuijpers, J., 1985. Space Sci. Rev. **40**, 25.

White, N. E., Culhane, J. L., Parmar, A. N., Kellett, B., Kahn, S., Van den Oord, G. H. J., Kuijpers, J., 1986. Astrophys. J., **301**, 262.

White, N. E., Shafer, R., Parmar, A. N., Culhane, J. L., 1987. 5th Cambridge Workshop on Cool Stars, Stellar Systems and the Sun, p.211.

White, N. E., Peacock, A., 1988. Mem. Soc. Astr. Ital., **59**, 7.

White, N. E., Arnaud, K., Day, C. S. R., Ebisawa, K., Gotthelf, E. V., Mukai, K., Soong, Y., Yaqoob, T., Antunes, A., 1994. Publ. Astron. Soc. Japan, **46**, L97.

White, N. E., 1996. In 9^{th} Cambridge Workshop on Cool Stars, Stellar Systems and the Sun, Pallavicini, R., Dupree, A. K.,eds.

White, S. M., Franciosini, E., 1995. Astrophys. J., **444**, 342.

Willingdale, R., 1991. ROSAT UK Newsletter No. 5, p.4

Wilson, R. F., Lang, K. R., 1987. Astrophys. J., **312**, 278.

Withbroe, G. L., Noyes, R. W., 1977. Ann. Rev. Astron. Astrophys., **15**, 363.

Wonnacott, D., 1994. priv. comm.

Wonnacott, D., Graffagnino, V., 2000. in prep.

Zahn, J. P., 1977. Astron. Astrophys., **57**, 383.

Appendix A

Spectral Modelling of Stellar Coronae

... The things we observe don't have the nature we wish them to, but rather, whatever they actually happen to have.

Gorgias of Leontini, Sicily, 5th Century B.C

A.1 X-RAYS FROM HOT OPTICALLY THIN PLASMAS

Over the years several spectral models have been developed which attempt to describe the radiated emissions from hot, optically thin plasmas, as found in stellar coronae. These involve calculations of the plasma emissivity, $\phi(\lambda, T)$ which is related to the measured flux of plasma contained within a volume, V and density, n, by,

$$I(\lambda) = \int_V \phi(\lambda, T) n^2 \, dV$$

Examples of such models include those of Mewe (1972), Landini and Monsignori Fossi (1972), Raymond and Smith (1977), Gaetz and Salpeter (1983), Mewe, Gronenschild and van den Oord (1985), and Landini et al. (1985).

A detailed description of the physical processes for emission within this type of plasma, the steps involved in performing the calculations, and the validity of the assumptions made, can be found in the reviews of Raymond (1988, 1990) and Mewe (1991).

Briefly, in order to simplify the calculations, it is assumed that the plasma is hot, and of relatively low density (fairly reasonable in the case of coronae), the velocity distribution of the electrons is Maxwellian, and that the effects of electric and magnetic fields, and of photoionisation are negligible. Collisional ionisation equilibrium is assumed for the plasma, and the ionisation and recombination rates are computed and used to define this ionisation balance for each element within the plasma. The emissivity of the plasma can then be calculated once the ionisation states of the more abundant elements are known. The basic processes involved are collisional excitation, bremmstrahlung and recombination.

Collisional excitation: For plasmas with temperature $\lesssim 10^7$ K, X-ray emission and hence cooling of the plasma is dominated by spectral lines emitted via electron collisions.

Bremmstrahlung: When an electron passes close to an ion, it is decelerated by the ion's electric field, and in so doing it radiates. This process is more dominant for plasmas with temperature $\gtrsim 10^7$ K.

Recombination: Important contributions to this process come from the hydrogenic and helium-like ions within the plasma (for which the calculations are more simple and reliable). The rate of recombination is

dependant on both the rate of radiative recombination (the opposite of photo-ionisation) and that of dielectric recombination (which dominates in most coronal ions).

Differences within the various models mentioned, arise from the differing excitation rates and ionisation balances calculated by these authors. The interested reader is referred to Raymond (1988) who shows a comparison of a number of these calculated emissivities.

These plasma codes have been used in a variety of ways to model stellar coronæ, and these will now be discussed.

A.1.1 One-temperature and Two-temperature Thermal Plasma Models

By analogy with the Sun, where a multi-temperature coronal environment has been demonstrated, both single-temperature and two-temperature thermal plasma models can best be thought of as describing *representative* temperatures for stellar coronae (Majer et al., 1986; Schmitt et al. 1990).

The single-temperature models were predominantely used to fit spectra obtained from the earliest X-ray missions, which were hampered by relatively low signal-to-noise of the data. However, this model has also been used to fit higher signal-to-noise stellar flare data, albeit with some modification e.g. the addition of an Iron line (Tsuru et al. 1989), a power-law component (Drake et al. 1994; this thesis), or a low metal abundance (Ottmann and Schmitt 1996; Kürster and Schmitt 1996). The two-temperature thermal plasma model is probably the most common type of model used to fit stellar coronal spectra (see section 1.3.3). However, recent work has shown that in some cases, these models also require the additional constraint of a low metal abundances (e.g. Antunes et al. 1994; Drake et al. 1994; Singh et al. 1995).

These models are parameterised by a temperature and an emission measure for each of the separate temperature components e.g. for a one-temperature model there are two fitting parameters. A two-temperature model would comprise of a linear combination of two isothermal models and thus would consist of four fitting parameters i.e. two temperatures and their corresponding emission measures. Obviously the inclusion of low metal abundance increases the number of parameters by one for each of the temperature components so affected.

A.1.2 Continuous emission measure models

Comparison of spectral results for objects observed with both *Einstein* and EXOSAT has led to the suggestion that a more physically realistic description of stellar coronae is one involving a plasma with a continuous emission measure distribution (Majer et al., 1986; Schmitt et al. 1990; Pasquini et al. 1989). A simplified version of this model, is one in which the emission measure follows a powerlaw distribution, and has been used in the case of the Sun (e.g. Antiochos and Noci 1986) as well as for RS CVns (e.g. Schmitt et al. 1990; Pasquini et al. 1989)

A model of this form, i.e.,

$$EM(T) = EM_{\max}\left(\frac{T}{T_{\max}}\right)^{\alpha}$$

requires only two fitting parameters: $T_{\max}$ an arbitrary maximum temperature (upon which $EM_{\max}$, the normalisation constant, is used to derive the corresponding maximum emission measure) and α an assumed slope for the emission measure distribution.

A.1.3 Multi-Temperature and Differential emission measure models

The level of temperature stratification within the corona can be constrained using a differential emission measure (DEM) method. Unlike the simplified form of the continuous emission measure described above, this method makes no initial assumption about the form of distribution of emitting plasma. In simple terms the DEM, $Q(T)$, can be thought of as a measure of the amount of emitting material at a particular temperature, T. The emission measure, EM, can therefore be defined as,

$$EM = \int_{T-\Delta T}^{T+\Delta T} Q(T)\, dT \equiv \int n_e^2\, dV$$

and gives the emitting power of a plasma of density n_e contained in volume V, between the temperatures $T - \Delta T$ and $T + \Delta T$.

For broad-band instruments, such as the PSPC, this distribution can be approximated by using a multi-temperatue thermal plasma model to sample the emission of plasma at various temperatures. As with two-temperature models, a multi-temperature model would comprise a linear combination of isothermal plasma models, one for each temperature component.

A.1.4 Loop Modelling

Application of these models to RS CVn systems include those of Schrijver et al. (1989), Ottmann et al. (1993) and Ottmann (1993). More recently a number of papers by Ciaravella et al. (1995) and Maggio and Peres (1995) have also discussed this approach more fully. These studies have shown that higher spectral resolution data from instruments onboard future missions such as AXAF and XMM, may require the more complex loop models to describe the spectra satisfactorily. Previous investigation of these coronal structures

culminated in a number of analytical models and scaling laws being developed. These early models used the simplifying assumption that the quiescent loop structures forming the corona are essentially in hydrostatic equilibrium. Among these early "quasi-static" models were those of Rosner, Tucker and Vaiana (1978) — hereafter referred to as the RTV model — and those of Craig, McClymont and Underwood (1978). In the RTV model, Rosner et al. (1978) defined an energy balance relation by equating the energy input to the loop (in terms of a local heating function and an expression involving fluid input to the loop) with the energy losses (via conduction, radiation and mass transport) and integrating this over the whole volume of the loop. This can be expressed in the form,

$$\int_v \mathcal{E}_{\rm I} = -\int_v \mathcal{E}_{\rm R} + \mathcal{L}_{\rm f} + \mathcal{L}_{\rm s}$$

where $\mathcal{E}_{\rm I}$ is the energy input to the whole loop, $\mathcal{E}_{\rm R}$ is the radiative energy losses over the whole loop, and the final two terms, $\mathcal{L}_{\rm f}$ and $\mathcal{L}_{\rm s}$, are the energy losses at the boundaries of the loop, i.e the footpoints and sides of the loop respectively. The plasma contained within the magnetic field lines defining the loop is thermally insulated from the outside (Spitzer 1962), therefore energy losses via the sides is negligible. Energy losses via the footpoints (through thermal conduction and mass transport) can be assumed negligible, because the initial assumption of this model is that these quiescent structures are quasi-static. Any non-negligible mass flux within the loop would cause energy and structural changes, in contrast to the quasi-static assumption. Thus the above energy equation can be simplified by equating the energy input with the sum of the radiative energy losses and any thermal redistribution of energy within the loop by conduction. Under these assumptions, the maximum temperature within the loop occurs at its peak, and a distribution of energy occurs along the loop length. Rosner et al. derived a scaling law relating the maximum loop

temperature T_{max}, with its corresponding base pressure , p (assumed constant throughout the loop), and semilength, L, of the form,

$$T_{max} = 1.4 \times 10^3 (pL)^{\frac{1}{3}} K$$

These agreed with earlier results from Solar X-ray observations. An expression for the heating function (which for simplicity is assumed constant over the whole loop length) was also derived, again in terms of the loop parameters:

$$E_H = 9.8 \times 10^4 (p^{\frac{7}{6}} L^{-\frac{5}{6}})$$

This work has been extended by a number of researchers who investigated the consequences of relaxing some of the initial assumptions. Vesecky et al. (1979) used a numerical rather than an analytic approach which allowed them to probe the effects of a variable cross-sectional area in the loop geometry.

A numerical approach was also used by Serio et al. (1981), enabling them to produce a more general form of the RTV model by considering loops in which both pressure and heating are allowed to vary along loop length. The variable heating considered was of the form,

$$E_H = E_0 e^{-s/s_H}$$

where E_H is the heating rate at position s along the loop, E_0 is the heating rate at the base of the loop, and s_H is the heating scale height.

The corresponding generalised scaling laws of Serio et al. are:

$$T = 1.4 \times 10^3 (p_0 L)^{\frac{1}{3}} \; e^{-\frac{1}{25} L(2/s_H + 1/s_p)}$$

$$E_0 = 10^5 (p_0^{\frac{7}{6}} L^{-\frac{5}{6}}) \; e^{\frac{1}{2} L(1/s_H + 1/s_p)}$$

and allow investigation of loops with lengths, L, greater than the pressure scale height, s_p.

A.2 THE NON-UNIQUENESS OF X-RAY SPECTRAL MODEL FITTING

The spectral analyses for this thesis have predominantely used multi-temperature thermal plasma models to approximate the distribution of the emitting material within the coronæ. This is preferable to using the continuous emission measure model, described in section A.1.2, because no assumption is made concerning the form of this distribution. However, one must still recognise that the relatively low-spectral resolution of the PSPC (see Appendix B) results in an assumed model that is still only an approximation to the real case.

Four-Temp. RS Model (Solar Abundances).								
kT_1/[keV]	K_1	kT_2/[keV]	K_2	kT_3/[keV]	K_3	kT_4/[keV]	K_4	$N_H/[10^{19}\ cm^{-2}]$
0.086	6.25	0.258	1.43	0.86	4.14	2.58	26.54	8.11
Two-Temp RS Model (Sub-Solar Abundances).								
kT_1/[keV]	Abundance	K_1		kT_2/[keV]	Abundance	K_2		$N_H/[10^{19}\ cm^{-2}]$
0.19	0.3	4.18		1.74	0.3	33.47		2.36
Two-Temp RS Model (Solar Abundances).								
kT_1/[keV]	K_1	kT_2/[keV]	K_2	$N_H/[10^{19}\ cm^{-2}]$				
0.19	4.18	1.74	33.47	2.36				

Table A.1: *Details of the Spectral Parameters and models used in creating the Simulated Source spectra. See text for details.*

To test the the validity of the fitting models used in this thesis, I employed the XSPEC package to perform a large number of spectral fitting simulations. I produced simulated datasets using a number of source coronal spectral models. The source spectra considered were Two-Temperature Raymond and Smith (RS) thermal plasma models (with Solar and sub-Solar abundances), and a Four-Temperature RS model with Solar abundance (see Table A.2). A number of faked datasets were created of varying integration times, for each of these source spectral models. The integration times ranged between 0.5

and 4.0 kiloseconds (in increments of 0.5 kiloseconds) and between 5.0 and 25.0 kiloseconds (in increments of 5 kiloseconds). These times were selected to reflect typical integration times of:

1. ROSAT PSPC survey spectra (< 1ks),
2. PSPC spectra typically found in the literature (1.0 ks—10.0 ks) and
3. the high signal-to-noise PSPC spectra analysed in Chapter 2.

Each source spectrum was then fitted with a variety of spectral models (listed below) in order to see how the spectral fits improved (as judged by the χ^2_ν statistic) as a function of integration time, and hence signal-to-noise. These simulations could also then be used to demonstrate whether a reasonable inference of the spectral source could be obtained for these fits. The spectral models used for fitting the faked datasets, were chosen either because they are common in the literature and/or have been used in this thesis. These are an isothermal RS model with sub-solar abundance, two-temperature RS models (solar and sub-solar abundances) and a four-temperature RS model. Each source-spectrum/fitted-model combination was fitted one thousand times. This was in order to provide good statistics and also to guard against obtaining fitted parameter values resulting from the XSPEC program finding a local minimum in χ^2_ν-space.

The results of these simulations are displayed in Figs. A.1–A.6 and provide an indication of the non-uniqueness of the spectral model fits, described in section 6.1.3 of the conclusions chapter.

A summary of the main results arising from these simulations now follow:

Two-Temperature RS Source Spectra (Solar Abundances): Source spectra produced from the canonical two-temperature thermal plasma model (with solar abundance), can be statistically well-fitted by any of the spectral models considered for integration times lower than approximately 10 ks (i.e. of the order of PSPC spectra typically found in the literature).

Two-Temperature RS Source Spectra (Sub-Solar Abundances): Source spectra produced from the canonical two-temperature thermal plasma model with sub-solar abundances, with integration times of several kiloseconds or greater, produced statistically poor fits for the canonical model (with solar abundances). However, single and two-temperature thermal plasma models (with sub-Solar abundances), as well as multi-temperature thermal plasma models *with Solar* abundances, provide good statistical fits, at these integrations times.

Multi-Temperature RS Source Spectra (Solar Abundances): Once again, for low integration spectra, any of the fitting models can provide reasonable statistical fits. However the cut-off point at which poor fits are obtained are (in order of increasing integration time): $\lesssim 3$ kiloseconds for the canonical model; $\lesssim 5$ kiloseconds for the two-temperature model with sub-solar abundances; and approximately ten kiloseconds for the isothermal model (sub-Solar abundance).

Therefore multi-temperature source model spectra with integrations times of length comparable to those found in the literature (i.e. $\lesssim 10$ ks), can be fitted reasonably well by two-temperature thermal plasma model with sub-Solar abundances (but *not* vice-versa). Note that it is impossible to determine

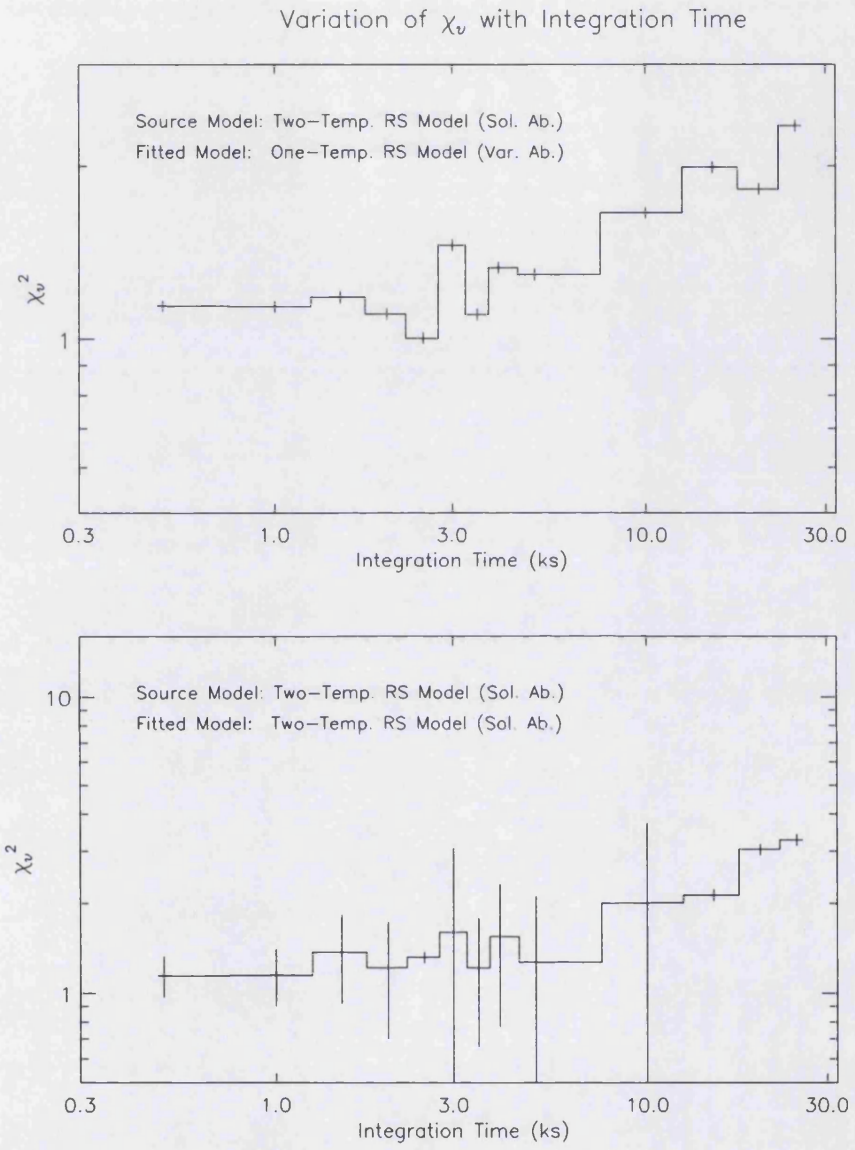

Figure A.1: *The mean χ^2_ν is plotted versus integration time to show how goodness of fit varies with increased signal-to-noise for a simulated source spectrum of a two-temperature RS model (with Solar abundance) fitted with (a) a one-temperature RS model with sub-Solar abundance, and (b) a two-temperature RS model (with Solar abundance). See text for details.*

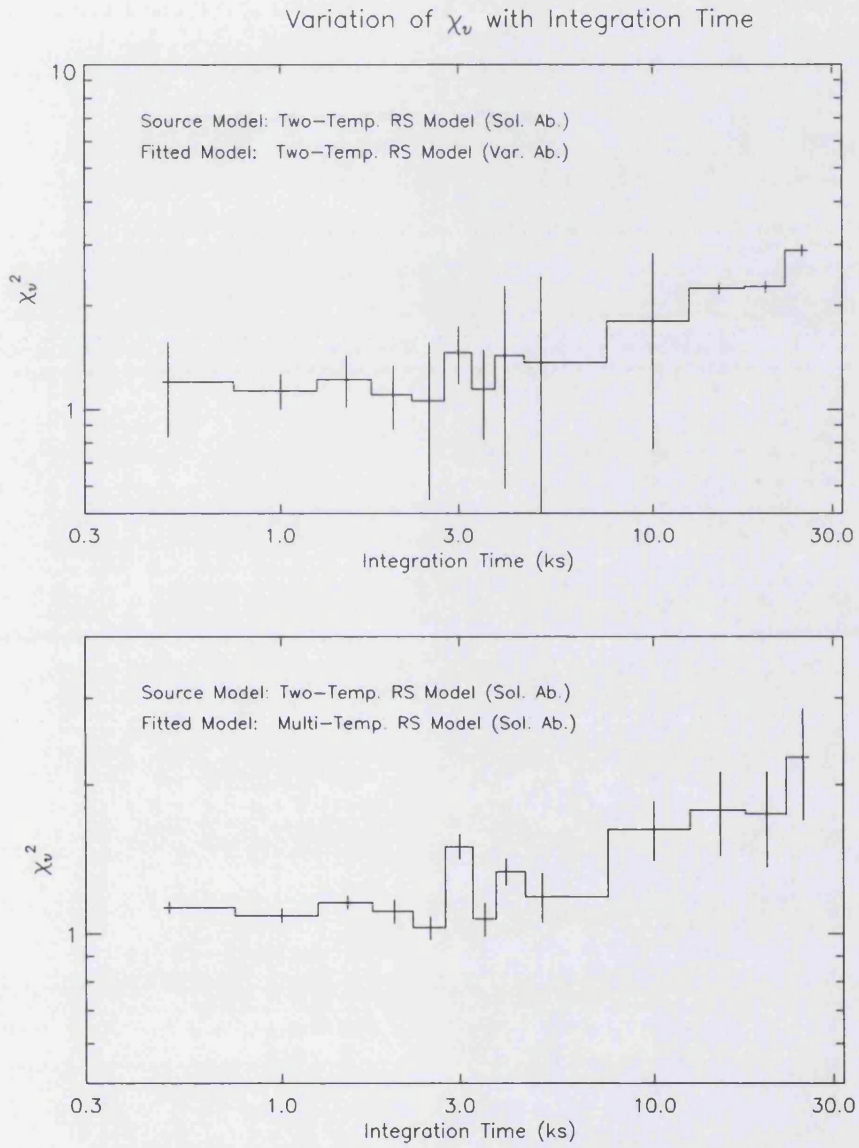

Figure A.2: *The mean χ^2_ν is plotted versus integration time to show how goodness of fit varies with increased signal-to-noise for a simulated source spectrum of a two-temperature RS model (with Solar abundance) fitted with (a) a two-temperature RS model (also with sub-Solar abundance) and (b) a multi-temperature RS model (with Solar abundances). See text for details.*

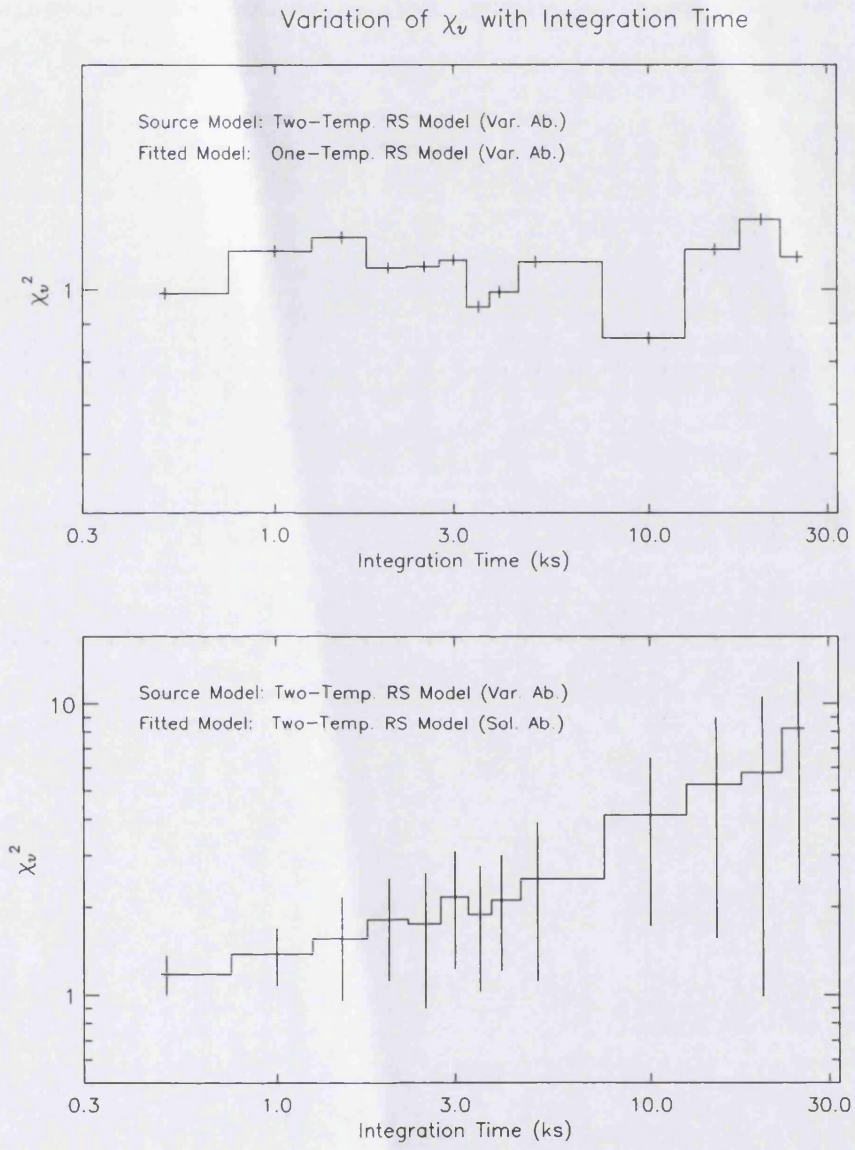

Figure A.3: *The mean χ_ν^2 is plotted versus integration time to show how goodness of fit varies with increased signal-to-noise for a simulated source spectrum of a two-temperature RS model (with sub-Solar abundance) fitted with (a) a one-temperature RS model with sub-Solar abundance, and (b) a two-temperature RS model (with Solar abundance). See text for details.*

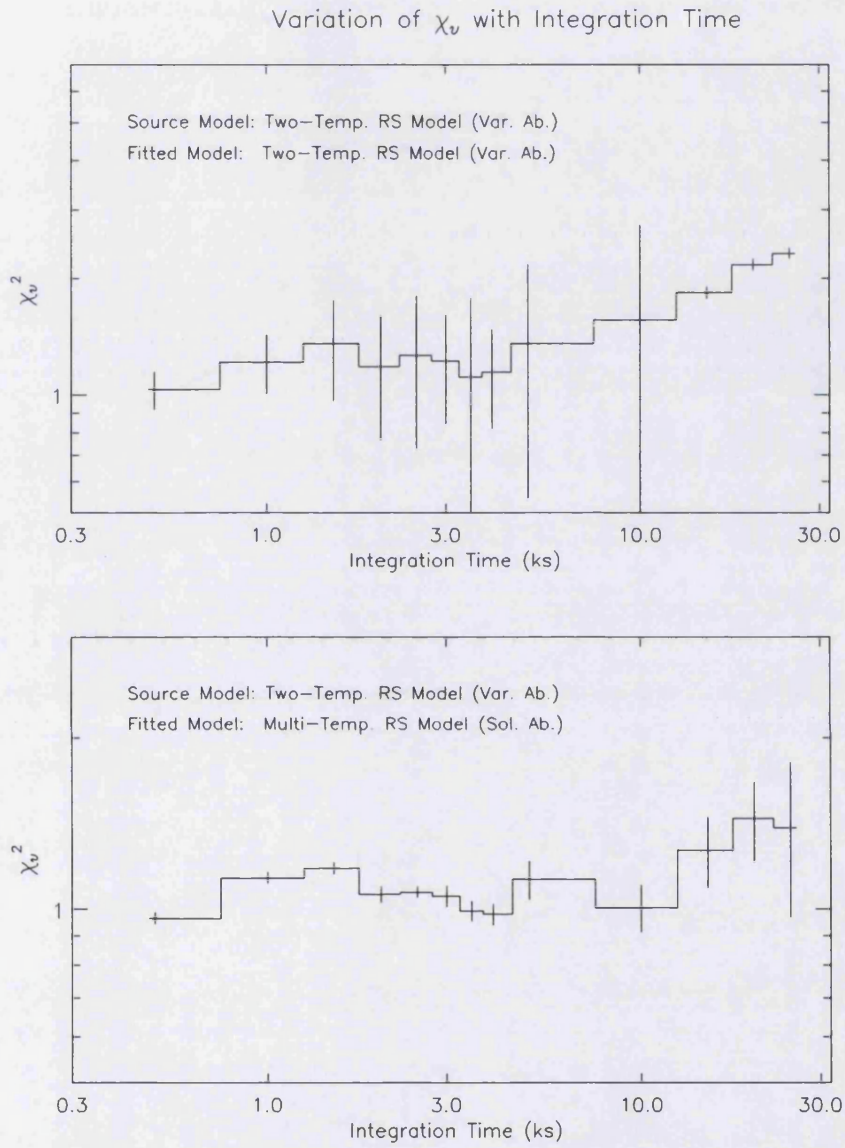

Figure A.4: *The mean χ^2_ν is plotted versus integration time to show how goodness of fit varies with increased signal-to-noise for a simulated source spectrum of a two-temperature RS model (with sub-Solar abundance) fitted with (a) a two-temperature RS model (also with sub-Solar abundance) and (b) a multi-temperature RS model (with Solar abundances). See text for details.*

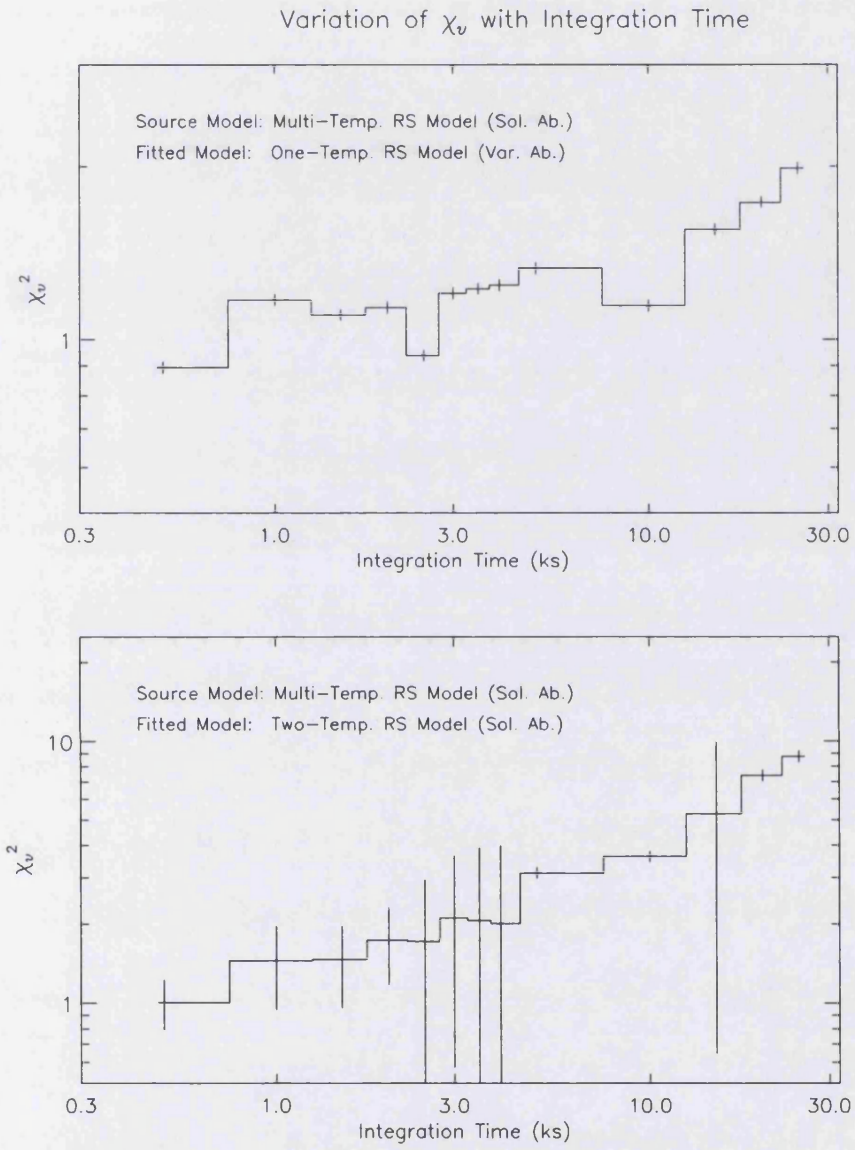

Figure A.5: *The mean χ^2_ν is plotted versus integration time to show how goodness of fit varies with increased signal-to-noise for a simulated source spectrum of a four-temperature RS model (with Solar abundance) fitted with (a) a one-temperature RS model with sub-Solar abundance, and (b) a two-temperature RS model (with Solar abundance). See text for details.*

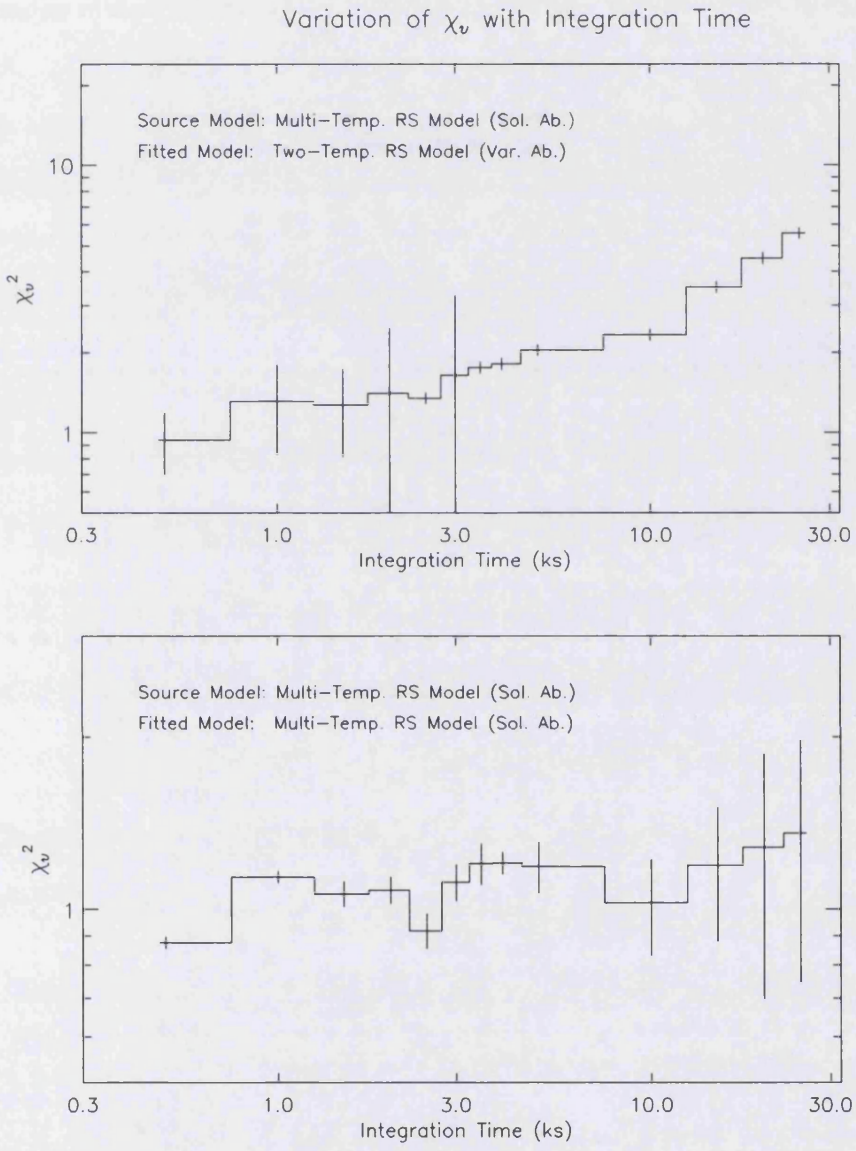

Figure A.6: *The mean χ^2_ν is plotted versus integration time to show how goodness of fit varies with increased signal-to-noise for a simulated source spectrum of a four-temperature RS model (with Solar abundance) fitted with (a) a two-temperature RS model (also with sub-Solar abundance) and (b) a multi-temperature RS model (with Solar abundances). See text for details.*

uniquely both abundances and temperature stratification based on PSPC spectra alone, particularly for spectra with low integration times. (See also Singh et al., 1996; Bauer and Bregman, 1996). Thus in the case of high signal-to-noise PSPC spectra, a multi-temperature plasma model can be used to give a satisfactory statistical fit in place of the canonical model with sub-solar abundances, in order to to reduce the number of fitting parameters. However this is not solely a case of obtaining statistically viable results. In the case of flare spectra, a multi-temperature model may be warrented due to possible abundance variations during the outburst itself as noted in Chapter 6

Four-Temp. RS Model (Solar Abundances).				
Model	**kT_1/[keV]**	**kT_2/[keV]**	**kT_3/[keV]**	**kT_4/[keV]**
1	0.1	0.35	0.9	2.0
2	0.086	0.258	0.86	2.58
3	0.1	0.22	1.2	2.5
4	0.12	0.6	1.2	2.4
5	0.12	0.3	0.7	2.4

Table A.2: *Temperatures used in fitting the HR 5110 Spectra with the four-temperature RS models. See text for details.*

As mentioned in Chapter 2 (where it is first introduced) the multi-temperature RS model is a linear combination of four Raymond and Smith optically thin plasma models, with the temperatures *fixed* at 10^6, 3×10^6, 10^7, and 3×10^7K, the emission measures, and column density, (i.e. five free parameters), allowed to vary. These four temperatures were chosen to cover the PSPC energy range, and are equally spaced in log space, with the initial temperature chosen arbitrarily.

Note however that the temperatures chosen are further constrained by an intrinsic limit to the achievable temperature resolution. This results from the

range of temperatures which any particular spectral line emitted in the thermal plasma, will contribute to the overall spectrum – roughly a factor of two in temperature (Mewe et al. 1995). Note that this is a physical constraint and *is independent of the energy resolution of the instrument.* Thus spectral parameters derived from an observed X-ray spectrum, may not be unique due to this smoothing out of the temperature information. A detailed discussion of this temperture resolution limit and a strategy to provide optimal temperature bins is detailed by Mewe et al. (1995) and more completely by Craig and Brown (1986) who consider general inversion problems found in astronomy. These authors recommend that to minimise the spreading of temperature information between adjacent temperture bins, the logarithmic temperature interval must not be smaller than $\Delta\log(T)\approx 0.15$. This condition *is* met by the temperatures selected for the multi-temperature model used in this thesis, which were chosen to cover the energy range of the PSPC. The choice of initial temperature was arbitrary and in no way affects the conclusions found in this thesis. To demonstrate this, the spectra from Chapter 3 were refitted with multi-temperature models, using different initial temperatures, but with temperture intervals satisfying the condition stated above. The temperatures used are given in Table A.2 and the results can be seen in Figs. A.7–A.10 which show the same characteristic 'U'-shaped emission measure distribution,regardless of the various temperatures chosen. Thus the use of a multi-temperature thermal plasma model, as used in this thesis, to provide a crude approximation to the underlying emission measure distribution, can be considered a valid one.

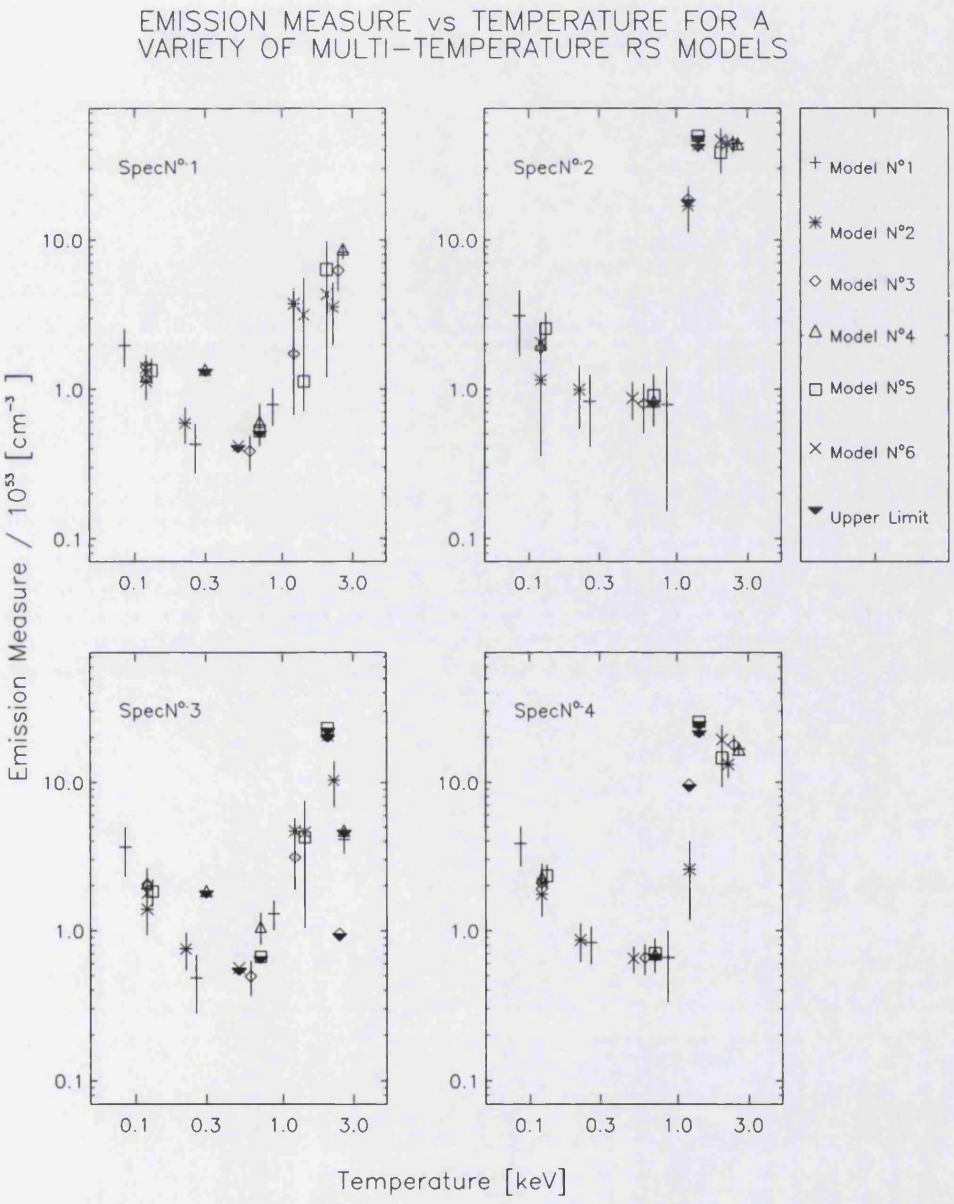

Figure A.7: *An Emission Measure versus Temperature plot for Spectra N°s. 1–4 from the HR 5110 deep survey follow-up observation. A variety of four fixed-temperature RS models have been used, as indicted by the various symbols. See text for details*

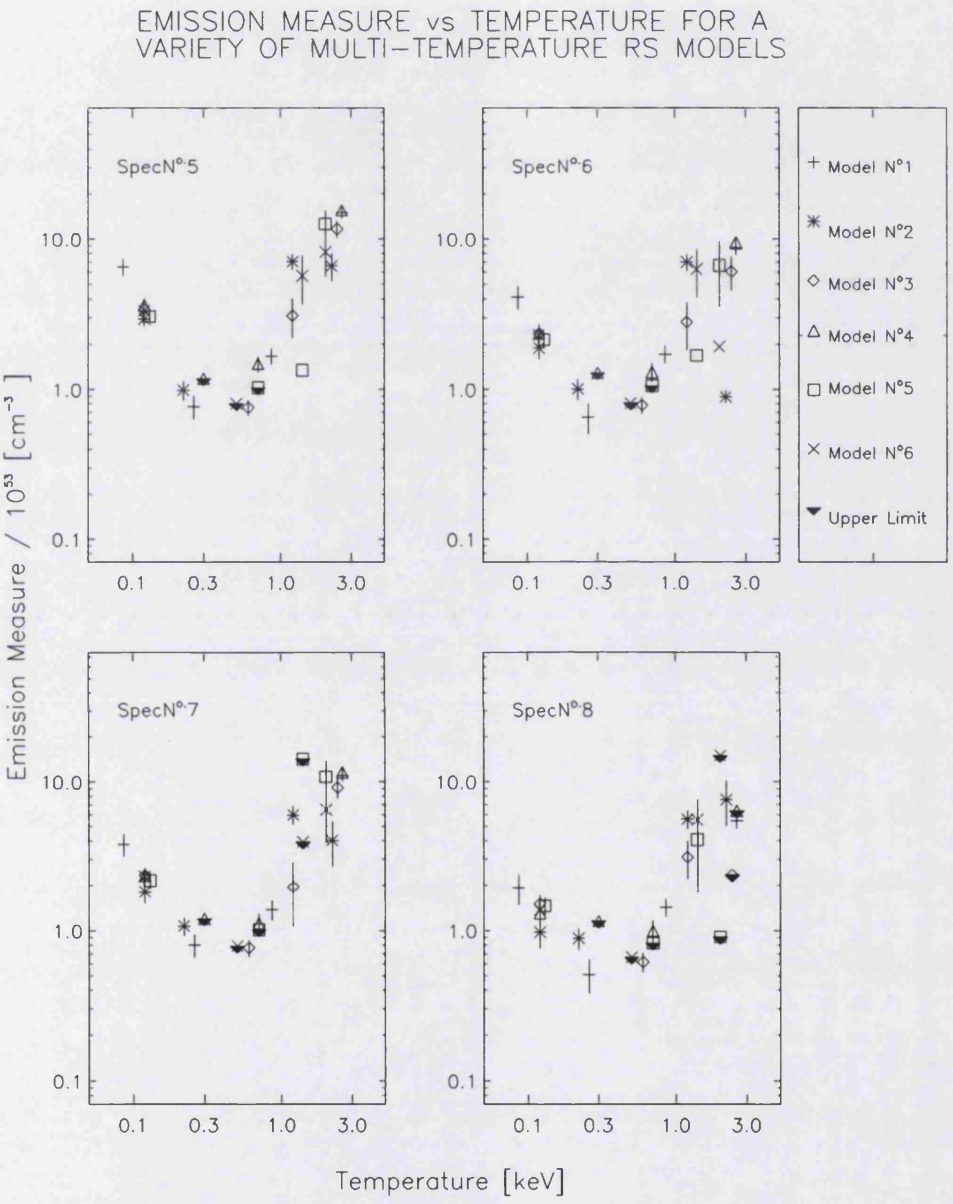

Figure A.8: *An Emission Measure versus Temperature plot for Spectra N°. 5–8 from the HR 5110 deep survey follow-up observation. A variety of four fixed-temperature RS models have been used, as indicted by the various symbols. See text for details*

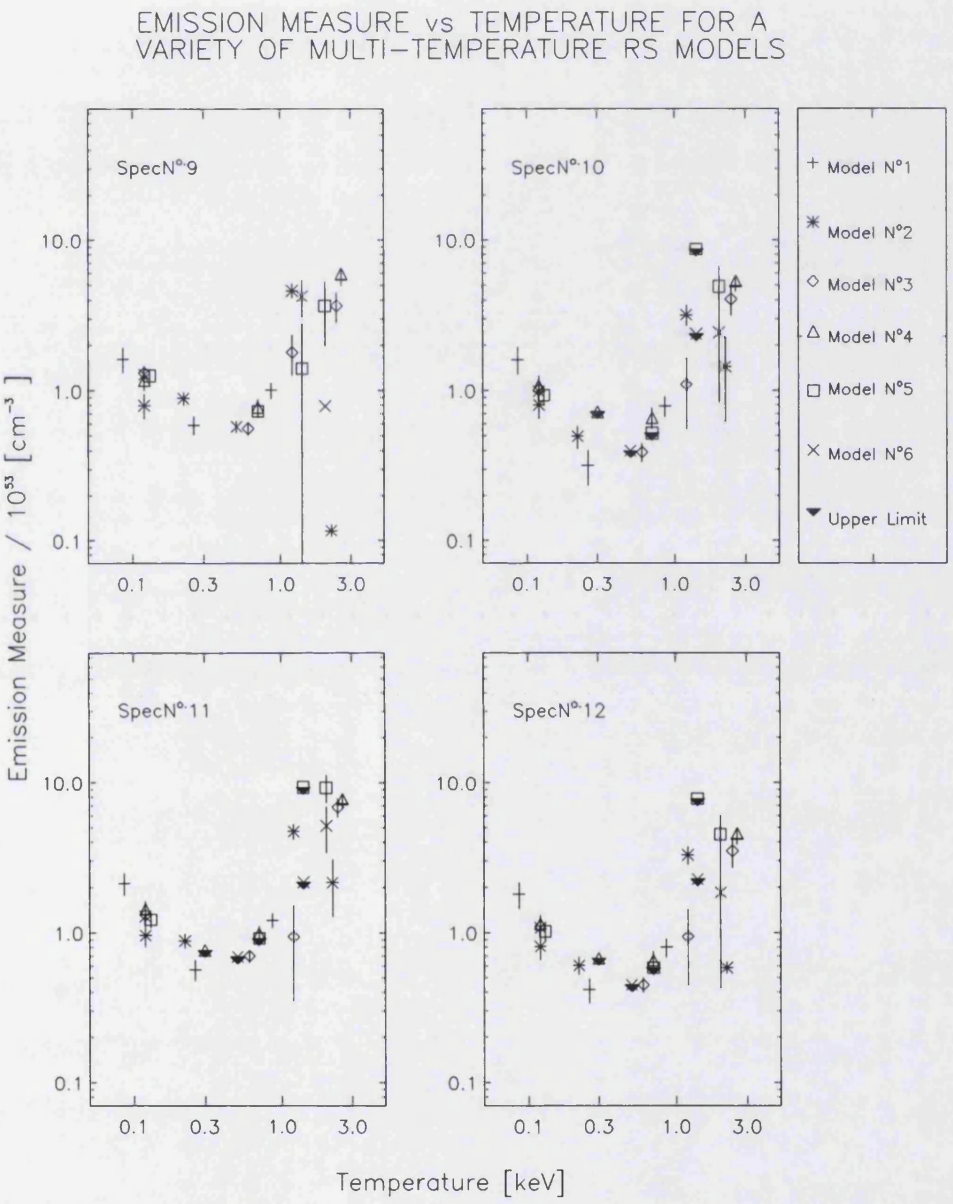

Figure A.9: *An Emission Measure versus Temperature plot for Spectra N°. 9–12 from the HR 5110 deep survey follow-up observation. A variety of four fixed-temperature RS models have been used, as indicted by the various symbols. See text for details*

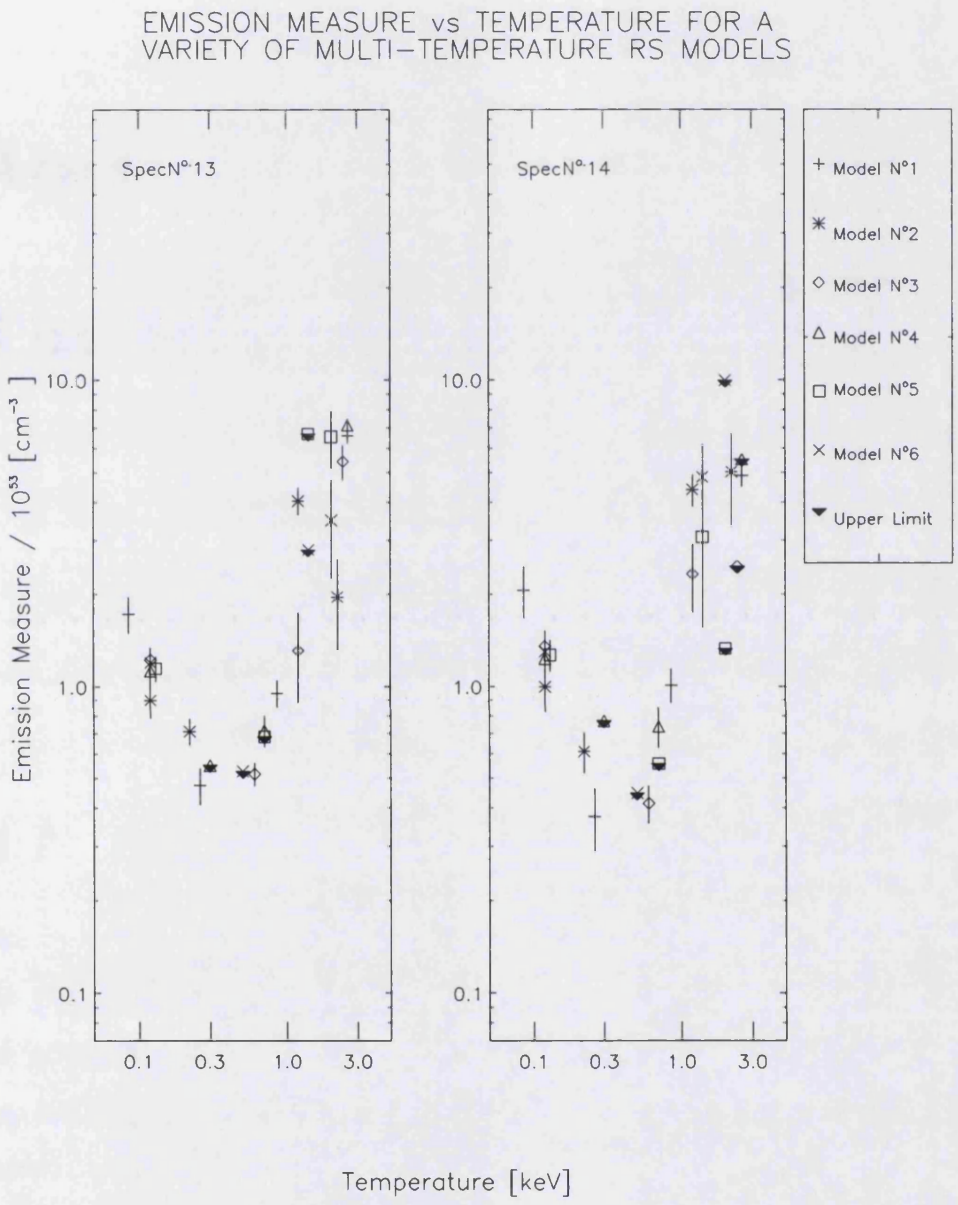

Figure A.10: *An Emission Measure versus Temperature plot for Spectra N°. 13–14 from the HR 5110 deep survey follow-up observation. A variety of four fixed-temperature RS models have been used, as indicted by the various symbols. See text for details*

Appendix B

The ROSAT Mission

... A common mistake that people make when trying to design something completely foolproof is to underestimate the ingenuity of complete fools.

Douglas Adams - "Mostly Harmless", 1992

B.1 AN OVERVIEW OF THE MISSION

The succesful launch on June 1 1990, of the RÖentgen-SATellit (ROSAT) was the culmination of a joint German/UK/US collaborative mission first conceived by M.P.E.(Max-Planck-Institut für Extraterrestriche Physik in Garching, Germany) in 1975. The main aim of this mission was to provide an all-sky survey with imaging X-ray and EUV telescopes of moderate angular ($\lesssim$1 arcmin) resolution and high X-ray sensitivity. As briefly mentioned in chapter 2, the survey phase of the ROSAT mission, was conducted by continuous scanning of the sky along a series of strips of width 2° and 5° for the PSPC and the WFC instruments, respectively. Each strip, which lay roughly perpendicular to the Ecliptic plane and intersected the Ecliptic poles, was scanned once per

orbit, with the intersection of strip and ecliptic plane advancing by 1^o per day. This initial six month survey phase of the mission was subsequently followed by a pointed observation phase.

The scientific payload for the mission consisted of the German X-ray Telescope, XRT, (Trümper 1991) and the co-aligned Wide-Field Camera, WFC, (designed by the British consortium)[11] which extended the spectral bandpass covered by ROSAT to the lower energies of the EUV[12] (see Fig. B.1)

The X-ray telescope was comprised of detectors and an X-ray Mirror Assembly, consisting of four Wolter type I mirrors (see Fig. B.2). This mirror configuration allows high energy photons such as X-ray or EUV, to reflect at grazing incidence angles, typically between $83'$ and $135'$. If the incident angles are greater than this, the photons will be absorbed by the mirror itself. Each mirror has a maximum aperture of 0.835 m. and a focal-length of 2.40 m, which have been nested together in order to increase the effective collecting area of the telescope (1141 cm^2). The mirrors are constructed from zerodur, a glass ceramic with a virtually negligible thermal expansion coefficient, and are then coated with a thin layer of gold to enhance the X-ray reflectivity.

The instrumentation available to the XRT, are the Position Sensitive Proportional Counters (PSPCs) built by MPE, and described below, and the High Resolution Imager (HRI), built by the Americans. These are housed on a carousel which allow the instruments to be placed onto the the focal plane. The Wide Field Camera (WFC) uses its own mirror system co-aligned with the XRT.

---

[11]This consortium is comprised of Leicester University, Mullard Space Science Laboratory (UCL), Birmingham University, Rutherford Appleton Laboratory and Imperial College London.

[12]The energy range covered by the WFC is approximately 0.05–0.21 keV.

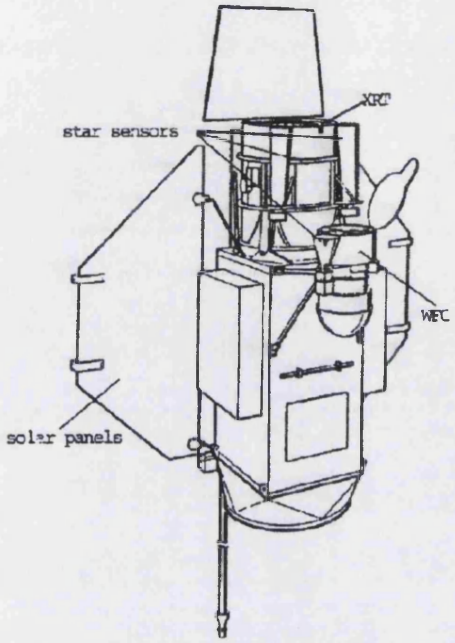

Figure B.1: *The ROSAT Satellite. Taken from ROSAT AO-2 Description*

B.2 THE ROSAT PSPC

There were four gas-filled multiwire position sensitive proportional counters (PSPCs) available to ROSAT, each with a filter wheel carrying a boron filter. These consisted of a pair of cathodes and anodes, contained within a housing filled with a 65% argon, 20% xenon and 15% methane gas mix. Both the cathodes and anodes are essentially wire grids, attached to a ceramic frame within a sealed chamber. The cathode uses platinum iridium wire wheras the anodes use gold-plated tungsten wires. A combination of anode and the two cathodes were used to detect the photo-electrons produced in the gas from an incoming

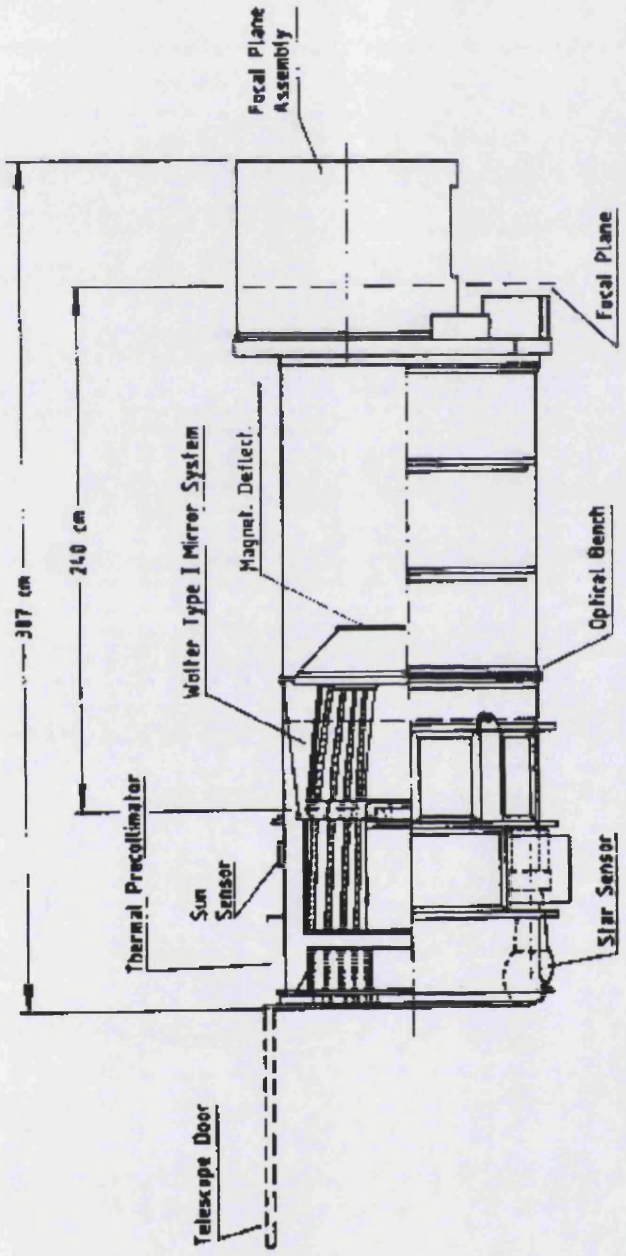

Figure B.2: *Cross-sectional view of the ROSAT XRT containing the nested Wolter type I mirror system and the focal plane turret containing the two PSPCs with filter wheels and one HRI (Extracted from ROSAT Users Handbook)*

X-ray photon and determine the direction and position of the photon. Electronic circuitry connected to the output of the proportional counter, known as the Pulse Height Analyser (PHA) measured and classified the size of the resulting voltage signal (and consequently the charge pulse generated on the anode by a particle or an X-ray photon) into a set of 'channels'. Thus a 'Pulse Height Distribution' of the particle/photon flux incident on the counter could be generated. The energy spectrum of the incident radiation could then be determined from the results of previous ground-based calibrations. The second anode was used as the anti-coincidence counter in order to perform background rejection.

The two flight-spares were used for ground calibration measurements (PSPC-A and PSPC-D) with PSPC-C to have been the primary detector and PSPC-B reserved as back-up[13] Each of these detectors were mounted on a carousel which could position the detectors at the focal point. They provided modest energy resolution ($\delta E/E = 0.43(E/0.93)^{-0.5}$), high spatial resolution ($\sim$ 25 arcsec at 1 keV) and time resolution capable of $\gtrsim$130 microseconds. On September 11, 1994, the PSPC was shut down to conserve the remaining detector gas.

B.3 THE ROSAT WFC

The Wide Field Camera (WFC) is an EUV telescope designed and built by the United Kingdom consortium. It uses three nested Wolter Type I mirrors of focal-length 0.525 m, co-aligned with the XRT, and uses a Microchanel plate

[13]On January 25^{th} an onboard computer glitch caused the ROSAT spacecraft to tumble out of control for approximately 15 hours, resulting in the satellite scanning the Sun, destroying the PSPC-C window. Once control had been regained, subsequent observations were made with PSPC-B.

(MCP) detector.

Filter Name/Type	**FOV Diameter (degrees)**	**Mean Energy (eV)**	**Bandpass (eV) (at 10% of peak)**
S1a (C/Lexan/B)	5	124	90-210
S1b (C/Lexan/B)	5	124	90-210
S2a (Be/Lexan)	5	90	62-111
S2b (Be/Lexan)	5	90	62-111
P1 (Al/Lexan)	2.5	69	56-83
P2 (Sn/Al)	2.5	20	17-24
OPQ (Opaque)	2.5	-	-
UV (UV interference)	2.5	-	-

Table B.1: *Details of the Filters used on the WFC.*

These MCPs are parallel arrays of tiny semiconducting fibre-optic tubes or 'channels'. A large number of these tubes can be bundled together and then sliced through to produce a plate, with sizes of a few to 15 cm diameter. In the case of the WFC the MCP is curved (to match the optimum focal surface and thus take advantage of the telescope resolution) and contains an array of $\approx 10^7$ channels, positioned at a small angle ($\approx 10°$) to the plate surface. This ensures that the incident photons strike the walls, resulting in emission of secondary electrons. The MCP is coated with a CsI photocathode which increases the quantum efficiency of the detector, and emits electrons when struck by EUV photons. It provides a five degree field-of-view with a spatial resolution of 2.3 arcmin (Sims *et al.* 1990).

As microchannel plates have no intrinsic spectral resolution, a filter wheel, containing eight filters, was provided to define the wavelength passbands covered, and surpress any geocoronal background radiation, which would have resulted in the saturation of the detector count-rate. Filter details are given in Table B.3.

The filters comprised of six science filters, consisting of two redundant pairs of 'survey' filters (S1a/S1b and S2a/S2b), two 'pointed' phase filters (P1 and P2), a UV filter and an opaque filter. The purpose of the survey and pointed filters are self-explanatory. The UV filter was used for in-flight monitoring of detector gain drifts and thermally-induced misalignment of the telescope axis. The "Opaque" filter is opaque to photons, but has a sensitivity to particle background. Unfortunately, unexpected leakage of stray-light has hampered its use for determining the particle component of the WFC background. For a complete description of ROSAT and its instrumentation, the reader is referred to the ROSAT Users Handbook (Briel et al. 1996).

Appendix C

Beyond ROSAT...

"The rung of a ladder was never meant to rest upon,
but only to hold a man's foot long enough to enable him
to put the other somewhat higher ...."

Thomas Henry Huxley
from Life and Letters of Thomas Huxley, 1975

C.1 Introduction

The study of stellar coronae has benefitted greatly from the ROSAT mission, and this success has been further built upon by a number of moderate spectral resolution EUV and X-ray missions such as EUVE, ASCA and BeppoSAX. The purpose of this appendix is to briefly summarise the main results found for stellar coronæas a foretaste of the kind of science which will be possible from the high spectral resolution missions CHANDRA and XMM-NEWTON which have recently been launched.

The main findings from these missions include the problem of elemental coronal abundances and the nature of the coronal emission measure distribution, and these are now briefly discussed.

One of the most surprising results to have come out of ASCA, was the anomalous coronal abundances in the quiescent coronæ of active stars, in which metals were often underabundant when compared with those of their photosphere by factors of 3-10 (e,g, White et al. 1994; Drake et al. 1996; White 1996). Similar results were obtained from EUVE (e.g. Rucinski et al. 1995) and later from BeppoSAX (Rodonó et al. 1999; Covino et al. 2000). Furthermore, most of the EUV flux in EUVE observations of RS CVn systems seems to reside in the continuum and a low line-to-continuum ratio is evident. This apparent lack of spectral lines has been dubbed "Metal Abundance Deficiency" (MAD) syndrome (Schmitt et al. 1996). These under-abundances were unexpected because in the solar corona elements such as Fe, Mg, Si, with first ionization potentials (FIP) less than 10 ev are overabundant (see Feldman & Widing, 1990) relative to the photosphere in contrast to the MAD syndrome. Although the cause of these abundance anomalies is still uncertain, the FIP effect is thought to be due different ionisation fractions existing between the high-FIP and low-FIP elements (von Steiger & Marsch 1994) whereas the coronal underabundance of metals (the MAD syndrome) is due to the establishment of hydrostatic equilibrium between the various ions, whose scale height would be dependent on the respective mass and charge of each ion species (see Mewe et al. 1997; Ottmann et al. 1998). However, some doubt has been raised as to whether these low abundances are real. One possible explanation suggested by Drake (1998) is that the coronal abundance depletion is actually only apparent. Instead an enhancement of the coronal He abundance is present. Thus the line-continuum ratio is reduced, which is required in measuring the metal

abundances from X-ray observations. The credibility of the low abundance values found has also been questioned by Rodonó et al. (1999) whose spectral analysis of Beppo-SAX observations of AR Lac emphasised the mutual inter-dependence of the fitted absorbing column with metal abundance as well as with the emission measure ratios.

Whether these abundance anomalies are real await further spectra from the high-resolution CHANDRA and XMM-NEWTON missions. The quality of these spectra will also provide a means of constraining the atomic data which have been used in plasma codes in a self-consistent manner (Brickhouse & Drake 2000) as well as checking for spectral lines which are missing in these plasma codes (Brickhouse et al. 2000).

Differences such as these abundance anomalies, are a further example of a shift from the Solar paradigm. Instead the phenomenology of stellar activity has been extended to encompass a wider range of stellar parameters, with the benefits that these extremes of activity can help us better understand these processes on the Sun. The presence of possibly long-lived polar active regions on RS CVns is another such example (Vogt et al. 1999). However, Lanza et al.'s analysis of long-term photometric observations of AR Lac, has shown that the presence of polar spots is not required to reproduce the photometric modulation although the existence of preferential longitudes for starspots was strongly suggested (Lanza et al. 1998).

The issue of coronal structures has also recently been addressed with the use of combined moderate resolution EUV and X-ray observations. Griffiths and Jordan (1998) have demonstrated that the emission measure distribution in RS CVns are continuous in nature but also exhibits a bi-modal structure, whose local temperature maxima are consistent with previous two-temperature thermal models, and the authors have suggested the presence of two families

of loops as the cause - one compact and high density, the other more extended and lower density. Jeffries' analysis of ROSAT observations of XY UMa also was suggestive of an extended corona, due to the lack of observed eclipses in his observations (Jeffries 1998)

Low density extended flare loops are also suggested from geometric analyses of long duration flares observed on UX Ari from a combined ASCA and EUVE observation (e.g. Gudel et al. 1999). However not all long duration flares necessarily require such large loops. A BeppoSAX observation of a flare on Algol was shown to be much smaller than calculated from the analysis of the lightcurve decay, both by using Reale et al.'s method (1997) and from geometrical constraints imposed by the self-eclipse of the observed flare lightcurve (Favata & Schmitt 1999; Schmitt & Favata 1999).

BeppoSAX allowed the hard X-ray emission above 10 keV to be observed for the first time during strong flares. These observations showed further abundance anomalies because abundance increases were observed during the flare outbursts from the initial quiescent depleted levels (e.g. Pallavicini & Tagliaferri 98; Favata & Schmitt 98; Rododno et al. 1999; Tagliaferri et al. 1999). Gudel et al.'s combined EUVE and ASCA observations of UX Ari. also showed significant elemental abundance increase during the flare rise, with the abundances of the low first ionization potential (FIP) elements typically increasing to higher levels than the high-FIP elements (Gudel et al. 1999). The authors suggest that a fractionation process occurring during the chromospheric evaporation phase selectively enrich the low-FIP elements. Alternatively, the chromospheric evaporation may itself bring metal-rich chromospheric plasma into the metal-poor corona. Increased absorption during flares suggestive of possible circumstellar HI has also been observed (Rodonó et al. 1999; Favata & Schmitt 1999).

At the time of writing, initial results from Chandra and XMM-Newton observations of RS CVn systems are minimal and await publication in the literature. However preliminary results are beginning to filter through to the X-ray community and include combined Chandra and EUVE observations of II Peg (Huenemoerder et al. 2000). These observations show a strong continuum together with a number of emission lines, such as Fe XXV, Si XIII-XIV, Mg XI-XII, Ne X, O VII-VIII, and N VII, spanning a decade in temperature.

A co-ordinated multi-wavelength program incorporating Chandra, EUVE, HST and VLA observations of HR1099 has also been reported (Osten et al. 1999). These observations, which covered half a binary cycle, displayed flaring activity ranging from radio to X-ray wavelengths and highlighted Chandra's ability to measure the coronal plasma motions in stellar flare events. For example light curves utilising Ne X and O VIII lines ((12.1Åand 19.0 Årespectively) displayed a number of impulsive rises and decays, and the overall velocity pattern of the bright Ne X feature was consistent with the 50 $\mathrm{km\,s^{-1}}$ orbital motion of the active primary star. Blue-shifts of 150–200 $\mathrm{km\,s^{-1}}$ in the Ne X lines were also apparent.